Technische Universität Ilmenau

Department of Computer Science and Automation

Control Engineering Group

University of Agder

Faculty of Engineering and Science

Department of Engineering Sciences

Identification of Fractional-Order Models for Viscoelastic Behavior

Master Thesis submitted in partial fulfillment
of the requirements for the degree of

Master of Science (M.Sc.)

Daniela Kapp

Supervising Tutor:	M.Sc. Christoph Weise (TU Ilmenau)
Responsible Professors:	Prof. Johann Reger (TU Ilmenau)
	Prof. Michael Ruderman (University of Agder)
Submission Date:	February 20, 2020

Acknowledgments

Abstract

In this thesis, the fractional-order modeling of viscoelastic behavior based on measurement data obtained in the frequency domain is analyzed. Polymer samples as well as the transfer behavior of a hydraulic dashpot are investigated, whereby two different experimental setups are used for the former. Existing fractional-order transfer function estimation algorithms based on integer-order identification techniques are applied. These algorithms require a priori knowledge of the system structure including the commensurate order of differentiation. Hence an iterative procedure is used to evaluate the influence of the unknown structure. To avoid this, a global optimization is introduced, where the commensurate order is also part of the parameter set to be optimized. The measured polymer samples show a viscoelastic stress response. It can be shown that known model structures of low order for viscoelastic models can represent the measured transfer behavior very well. It is also proven that integer-order models do not reach the accuracy achieved with fractional-order approaches. For low-dimensional models, for which similar coefficients are estimated, the commensurate order is also in a limited range. However, as soon as there are only small deviations or the given model orders increase, it fluctuates enormously between 0 and 1. Additional considerations have to be included in the identification process to generate reliable physical models. The investigated dashpot is rather approximated by integer-order models.

Kurzfassung

In dieser Arbeit wird die nicht-ganzzahlige Modellierung viskoelastischen Verhaltens auf Basis von Messdaten im Frequenzbereich untersucht. Unter Nutzung zweier Versuchsstände werden Messdaten verschiedener Kunststoffproben sowie eines hydraulischen Zylinders aufgenommen und deren Übertragungsverhalten bestimmt. Für die Identifikation der nicht-ganzzahligen Übertragungsfunktionen im Frequenzbereich werden bereits existierende Algorithmen implementiert, die aus ganzzahligen Identifikationsansätzen entstanden sind. Für die Anwendung dieser Methoden sind a priori Informationen über die Modellstruktur notwendig. Aus diesem Grund muss auf ein iteratives Verfahren zurückgegriffen werden. Um dies zu vermeiden, wird eine globale Optimierung genutzt, welche neben den Koeffizienten der Übertragungsfunktion auch die kommensurable Ordnung optimiert. Einige der untersuchten Kunststoffproben weisen ein viskoelastisches Verhalten auf. Es kann gezeigt werden, dass bekannte viskoelastische Modellstrukturen niedriger Ordnung das gemessene Übertragungsverhalten sehr gut abbilden. Außerdem ist erkennbar, dass mit ganzzahligen Modellen nicht die Genauigkeit einiger nicht-ganzzahliger Ansätze erreicht wird. Im Fall niedrigdimensionaler Modelle, deren geschätzte Koeffizienten in einem ähnlichen Bereich sind, liegen auch die gefundenen kommensurablen Ordnungen nah beieinander. Sobald jedoch kleine Abweichungen auftreten oder die Modellordnung höher angesetzt wird, variieren diese Ordnungen sehr stark im vorgegebenen Bereich von 0 bis 1. Daher sollten bei der Auswahl der Modelle weitere Betrachtungen mit einbezogen werden, um sinnvolle physikalische Modelle zu erhalten. Für den untersuchten Zylinder werden eher Modelle ganzzahliger Ordnung identifiziert.

Contents

Symbols List

Symbol	Unit	Description
$\arg(\cdot)$		Argument (polar angle) of a complex number
$\lceil \cdot \rceil$		Ceil function
$\mathbb{C}$		Set of complex numbers
$\mathrm{Cov}(x)$		Covariance matrix of x
$_C\mathcal{D}^\alpha$		Caputo fractional derivative
$\mathcal{D}^\alpha$		Grünwald-Letnikov fractional derivative
$_R\mathcal{D}^\alpha$		Riemann-Liouville fractional derivative
E	$\frac{\mathrm{kg}}{\mathrm{m\,s^2}}$, GPa	Young's modulus
$\mathrm{E}(\cdot)$		Expected value
$\mathcal{F}\{\cdot\}$		Fourier transform
$G(s)$		Transfer function
$\mathcal{I}^\alpha$		Riemann-Liouville fractional integral
$\mathrm{Im}\,(\cdot)$		Imaginary part
$\otimes$		Kronecker product
$\mathcal{L}\{\cdot\}$		Laplace transform
$E_{\alpha,\beta}(\cdot)$		Two-parameter Mittag-Leffler function
S^+		Moore-Penrose inverse of S
$\mathbb{N}$		Set of natural numbers

Symbol	Unit	Description
$\Gamma(\cdot)$		Gamma function
$\mathrm{Re}\,(\cdot)$		Real part
$\mathbb{R}$		Set of real numbers
$\mathbb{R}^+$		Set of positive real numbers
T_{d}	°C	Decomposition temperature
T_{g}	°C	Glass-transition temperature
T_{m}	°C	Melting temperature
ξ		Noise vector
$\epsilon(t)$		Strain
ω	$\frac{\mathrm{rad}}{\mathrm{s}}$, Hz	Frequency
σ		Standard deviation
σ^2		Variance
$\sigma(t)$	$\frac{\mathrm{kg}}{\mathrm{m}\,\mathrm{s}^2}$, Pa	Stress
η	Pa s	Coefficient of viscosity

Acronyms

FC	Force-controlled
FFT	Fast Fourier transform
FOTF	Fractional-order transfer function
LTI	Linear time-invariant
PBT	Polybutylene terephthalate
PC	Position-controlled
PP	Polypropylene
RMSE	Root-mean-square error
SQP	Sequential quadratic programming

1 Introduction

Since their discovery about 100 years ago, polymers have replaced many classic materials and taken over a huge area of application. They are used in the construction industry (e.g. as a replacement for wooden window frames), in the sanitary sector (as a replacement for ceramics), in the automotive industry as well as in the packaging industry and are essential for many other purposes [36]. In order to be able to open up further areas of application or to optimize the current use, complex and expensive tests have to be carried out. To replace these with numerical simulations, it is necessary to develop exact models of these plastics.

The aim of this thesis is the identification of fractional-order models based on real measured data in the frequency domain. Not only the transfer behavior of polymers is investigated, but also that of a hydraulic dashpot, which also has viscoelastic properties. Therefore, an existing hydraulic setup is used and modified to measure the strain-stress relation of different samples. For validation purposes single samples are remeasured with a servo-hydraulic testing machine for dynamic load measurement.

1.1 State of the Art

Many different models have already been developed to represent the viscoelastic behavior of polymers [16]. However, these classic integer-order models quickly become very large and need an excessive number of model parameters to adequately model the memory effects of physical processes. Although known for a long time, the fractional calculus has only managed to make the transition from theory to practice in recent decades. By introducing fractional-order operators instead of integer-order operators in the constitutive relations, the number of parameters required to accurately describe the dynamic properties can be significantly reduced [2, 23]. Although the model structure seems to be more natural for such processes, the identification is extensive. Compared to integer-order models, not only the number of states, but also the order of differentiation is an unknown system parameter. Additional, the maximum fractional order of the system gives no information about the other frac-

tional orders present. This is unlike the integer-order case where the maximum order dictates the only orders present [1, 12]. In [2] it is shown that the classical viscoelastic model with a large number of internal variables converges to the fractional-order model with a single internal variable. The extension of one-dimensional fractional-order viscoelastic models into their three-dimensional equivalents for finitely deforming continua, as well as the numerical algorithms for their solution are presented in [8]. For the application of Magnetic Resonance Elastography reconstruction algorithms, a fractional-order Voigt model of soft tissue-like materials is developed in [23].

There are various approaches available to identify fractional-order models in the time domain, e.g. subspace methods [19, 33] and modulation-function based methods [4, 20]. However, the computation in the time domain is costly in view of the long memory and the non-local properties of fractional differential operators [35]. The determination of a linear model is also much easier in the frequency domain, since in the time domain it is necessary to either design filters or estimate derivatives. There are also advantages in the treatment of noise. If the conditions for white noise in the time domain are violated (e.g. signal-correlated noise), the covariance matrix of the Fourier-transformed noise vector approximately takes the form of a scaled unit matrix and the signal can be assumed as "white-noise-like" in the frequency domain [11]. For these reasons, it was decided to conduct the investigations in the frequency domain.

In [6] the effect of the error definition is evaluated using nonlinear optimization techniques, whereas in [35] an identification method is presented which combines the merits of differential evolution algorithm and subspace identification algorithm in the frequency domain. In [34] different integer-order identification techniques are taken up, e.g. the complex-curve fitting introduced by Levy in [18], the weighting presented in [29] or an online identification method in [17], and are transferred to the fractional-order domain. The usefulness of these algorithms has already been investigated using a simple simulated example.

1.2 Contributions of this Thesis

The main focus of this thesis is to investigate the influence of the model structure and the commensurate order on the quality of identification. Furthermore, the algorithms presented in [34] are validated using real measurement data. The results are also compared with an optimization of the coefficients and the commensurate

order of the system. Materials are investigated that have not yet been described with fractional-order transfer functions. The attempt to model a hydraulic dashpot is also new. In addition, the thesis from the literature is to be proven that fractional-order models need a significantly lower number of parameters than integer-order models for the same identification accuracy.

1.3 Structure

This thesis is structured as follows: In Chapter 2 general definitions of fractional derivatives and integrals are briefly introduced and the fractional-order models in the frequency domain are explained. Based on this, the fundamental integer- and fractional-order models of linear one-dimensional viscoelastic phenomena are re-called. Assuming zero initial conditions these models are reduced to fractional-order transfer functions (FOTF). Furthermore, some remarks about hydraulic dashpots and white noise are made. Chapter 3 summarizes all necessary algorithms and procedures that are used for the fractional-order system identification in the frequency domain. This includes the postprocessing of the measurement data, the explanation of the basic ideas of the identification algorithms presented in [34] as well as the introduction of an optimization approach. The robustness of the identification approaches towards unknown structural parameters (commensurate order, general system order) are validated using simulation data in Section 3.4. In this context, the need for a global optimization is also addressed. Finally, the experimental setups, the measurement procedure, the results and their discussion, as well as the identified models and their validation are given in Chapter 4.

2 Fundamentals

The identification of the model parameters for fractional-order systems requires a basic understanding of the different definitions of these systems and the impacts in the frequency and time domain. Therefore, this chapter is used to give the most important functions needed for the definition of the fractional calculus, a list of the best-known fractional derivatives and integrals and the derivation of fractional-order dynamic systems in the time and frequency domain. Additionally, linear viscoelasticity is introduced and some important integer- and fractional-order models for the description of viscous materials are presented. The next section is dedicated to a short introduction of hydraulic dashpots, and finally noise is briefly discussed.

2.1 Special Functions

This section includes the definitions of the gamma function, the Mittag-Leffler function, and the Wright function.

The gamma function $\Gamma(\cdot)$, also known as second order Euler integral, is a generalization of the factorial $n!$ and allows n to take also non-integer and complex values [27]. It is defined by the integral

$$\Gamma(z) = \int_0^\infty e^{-t} t^{z-1} \mathrm{d}t$$

with $z \in \mathbb{C}$, $\mathrm{Re}\,(z) > 0$ [27]. The convergence at infinity is provided by e^{-t}, and for the convergence at $t = 0$, $Re(z) > 1$ must apply [27]. The gamma function has many useful properties. One of the most important for the fractional calculus is the following characteristic which also shows the generalization of the factorial $n! = \Gamma(n+1)$ [27]:

$$\Gamma(z+1) = z\Gamma(z).$$

The one-parameter Mittag-Leffler function $E_\alpha(\cdot)$ generalizes the exponential function $e^z = \sum_{k=0}^{\infty} \frac{z^k}{k!}$ [27]

$$E_\alpha(z) = \sum_{k=0}^{\infty} \frac{z^k}{\Gamma(\alpha k + 1)}, \quad \text{Re}(\alpha) > 0.$$

A very important role in fractional calculus plays the two-parameter Mittag-Leffler function $E_{\alpha,\beta}(\cdot)$, which is defined by the series expansion [27]

$$E_{\alpha,\beta}(z) = \sum_{k=0}^{\infty} \frac{z^k}{\Gamma(\alpha k + \beta)}, \quad \text{Re}(\alpha) > 0, \quad \text{Re}(\beta) > 0.$$

Particular cases of the Mittag-Leffler function are e.g. the hyperbolic sine and cosine as well as the trigonometric functions [27]. This function has an important application in the solution of differential equations of rational order [27].

Another notable function for solving linear partial fractional differential equations is the Wright function

$$W(z; \alpha, \beta) = \sum_{k=0}^{\infty} \frac{z^k}{k!\Gamma(\alpha k + \beta)}.$$

2.2 Fractional Derivatives and Integrals

"The fractional calculus is a name for the theory of integrals and derivatives of arbitrary order, which unify and generalize the notions of integer-order differentiation and n-fold integration" [27, p. 42]. A short overview of this theory will now be given.

For the description of fractional integrals, the concept of Riemann-Liouville is the best-known. Based on Cauchy's formula for repeated integrals, the Riemann-Liouville fractional-order integral is defined as [24]

$$\mathcal{I}_c^\alpha f(t) = \frac{1}{\Gamma(\alpha)} \int_c^t \frac{f(\tau)}{(t - \tau)^{1-\alpha}} \mathrm{d}\tau, \quad t > c, \quad \alpha \in \mathbb{R}^+. \tag{2.1}$$

For dynamic systems, it can be assumed that $f(t)$ is a causal function of t, i.e. $t > 0$, and thus the definition that is mostly used is [24]

$$\mathcal{I}^\alpha f(t) = \frac{1}{\Gamma(\alpha)} \int_0^t \frac{f(\tau)}{(t - \tau)^{1-\alpha}} \mathrm{d}\tau, \quad t > 0, \quad \alpha \in \mathbb{R}^+. \tag{2.2}$$

In the following definitions of fractional derivatives the special case $c = 0$ is still used. For simplification, $\mathcal{D}^\alpha$ is therefore given instead of $_0\mathcal{D}^\alpha$.

Let $\mathcal{D}^m$ be the derivative operator of order $m \in \mathbb{N}$. Then the just defined integral operator in (2.2) can be transformed into the Riemann-Liouville fractional-order derivative of arbitrary order $\alpha \in \mathbb{R}^+$, $m = \lceil \alpha \rceil$, that is [24]

$$_R\mathcal{D}^\alpha f(t) = \mathcal{D}^m \mathcal{I}^{m-\alpha} f(t) = \frac{\mathrm{d}^m}{\mathrm{d}t^m} \left[\frac{1}{\Gamma(m-\alpha)} \int_0^t \frac{f(\tau)}{(t-\tau)^{\alpha-m+1}} \mathrm{d}\tau \right].$$

Fractional derivatives is the short name for derivatives of arbitrary real order [27]. Another very common definition of the fractional-order derivative was introduced by Caputo [24]:

$$_C\mathcal{D}^\alpha f(t) = \mathcal{I}^{m-\alpha}\mathcal{D}^m f(t) = \frac{1}{\Gamma(m-\alpha)} \int_0^t \frac{f^{(m)}(\tau)}{(t-\tau)^{\alpha-m+1}} \mathrm{d}\tau,$$

where $m = \lceil \alpha \rceil$ and $f(t < 0) = 0$. This definition requires the absolute integrability of the mth-order derivative of the function f, therefore it is more restrictive than the Riemann-Liouville definition [24]. It allows the formulation of initial conditions for initial-value problems for fractional-order differential equations in a form involving only the limit values of integer-order derivatives at the lower terminal (initial time) [27]. This is important for applied problems that require physically interpretable initial conditions, which are not given by the Riemann-Liouville approach [27].

Due to its importance in applications, the definition of Grünwald-Letnikov [24] shall be mentioned, as well,

$$\mathcal{D}^\alpha f(t) = \lim_{\substack{h \to 0 \\ nh=t \\ n \in \mathbb{N}}} \frac{1}{h^\alpha} \sum_{i=0}^n (-1)^i \binom{\alpha}{i} f(kh - ih).$$

The definitions of the fractional calculus in the time domain are quite difficult to handle. Therefore, a frequency domain analysis is reasonable. Fundamental tools in systems and control engineering are Laplace and Fourier integral transforms [24]. The Laplace transform of the function $f(t)$ is defined by

$$\mathcal{L}\{f(t)\} = F(s) = \int_0^\infty e^{-st} f(t)\mathrm{d}t, \tag{2.3}$$

where $s \in \mathbb{C}$ is a complex number that can be interpreted as a frequency parameter [27]. In most cases, $s \in \mathbb{C}^+$ to ensure the convergence of the integral for functions with exponential growth, which are the common solutions of ordinary linear systems.

The Laplace transforms of the presented fractional-order operators are [24]

$$\mathcal{L}\left\{\mathcal{I}^{\alpha}f(t)\right\} = s^{-\alpha}F(s),$$

$$\mathcal{L}\left\{{}_{R}\mathcal{D}^{\alpha}f(t)\right\} = s^{\alpha}F(s) - \sum_{k=0}^{m-1}s^{k}\left[{}_{R}\mathcal{D}^{\alpha-k-1}f(t)\right]_{t=0},$$

$$\mathcal{L}\left\{{}_{C}\mathcal{D}^{\alpha}f(t)\right\} = s^{\alpha}F(s) - \sum_{k=0}^{m-1}s^{\alpha-k-1}f^{(k)}(0),$$

$$\mathcal{L}\left\{\mathcal{D}^{\alpha}f(t)\right\} = s^{\alpha}F(s),$$

where $m - 1 \leq \alpha < m$. The exponential Fourier transform of a continuous function h is defined by

$$\mathcal{F}\left\{h(t)\right\} = \int_{-\infty}^{\infty}e^{j\omega t}h(t)\mathrm{d}t.$$

For the defined fractional-order operators holds [24]

$$\mathcal{F}\left\{\mathcal{I}^{\alpha}f(t)\right\} = \mathcal{F}\left\{\frac{t_{+}^{\alpha-1}}{\Gamma(\alpha)}\right\}\mathcal{F}\left\{f(t)\right\} = (j\omega)^{-\alpha}F(\omega),$$

$$\mathcal{F}\left\{\mathcal{D}^{\alpha}f(t)\right\} = \mathcal{F}\left\{\mathcal{D}^{m}\mathcal{I}^{m-\alpha}f(t)\right\} = (j\omega)^{\alpha}F(\omega),$$

where $m - 1 \leq \alpha < m$.

2.3 Definition and Stability of Fractional-Order LTI Systems

After introducing the most important definitions of the fractional calculus, the various ways to describe continuous-time dynamic systems of fractional-order are now presented as a central theme of this thesis.

In the LTI single variable case, a fractional-order system can be characterized with the equation

$$A(\mathcal{D}^{\alpha_0\ldots\alpha_n})y(t) = B(\mathcal{D}^{\beta_0\ldots\beta_m})u(t), \tag{2.4}$$

with the input $u(t)$, the output $y(t)$ and the combination laws of the fractional-order derivative operator $A(\mathcal{D}^{\alpha_0\ldots\alpha_n}) = \sum_{k=0}^{n}a_k\mathcal{D}^{\alpha_k}$ and $B(\mathcal{D}^{\beta_0\ldots\beta_m}) = \sum_{k=0}^{m}b_k\mathcal{D}^{\beta_k}$ with a_k, $b_k \in \mathbb{R}$ [24].

Definition 1 (Commensurate order [24]). *A system is of commensurate order q, if all the orders of derivation are integer multiples of the base order $q \in \mathbb{R}^{+}$, that means α_k, $\beta_k = kq$.*

A system of commensurate order can be written as

$$\sum_{k=0}^{n} a_k \mathcal{D}^{kq} y(t) = \sum_{k=0}^{m} b_k \mathcal{D}^{kq} u(t). \tag{2.5}$$

It can be noted that from a numerical point of view all systems are commensurable because coefficients can be chosen infinitesimally small, so that the corresponding order (i.e. a multiple of the commensurate order) no longer has any influence. The system described by (2.5) is of rational order, if $q = 1/p$, $p \in \mathbb{Z}^+$ [24].

The transfer function of fractional-order systems (2.4) can be obtained by applying the Laplace transform (2.3) with zero initial conditions [24]. This yield

$$G(s) = \frac{Y(s)}{U(s)} = \frac{b_m s^{\beta_m} + b_{m-1} s^{\beta_{m-1}} + \ldots + b_0 s^{\beta_0}}{a_n s^{\alpha_n} + a_{n-1} s^{\alpha_{n-1}} + \ldots + a_0 s^{\alpha_0}}.$$

In case of a commensurate order q, this equation changes to

$$G(s^q) = \frac{\displaystyle\sum_{k=0}^{m} b_k s^{kq}}{\displaystyle\sum_{k=0}^{n} a_k s^{kq}}, \tag{2.6}$$

where $G(s^q)$ consists of two pseudo polynomials. This relationship can also be expressed using a pseudo-rational function [24]

$$H(\lambda) = \frac{B(\lambda)}{A(\lambda)} = \frac{\displaystyle\sum_{k=0}^{m} b_k \lambda^k}{\displaystyle\sum_{k=0}^{n} a_k \lambda^k}.$$

The fractional-order transfer function is obtained by inserting $\lambda = s^q$.

The two main external stability criteria for the polynomial representations are set out in the following.

Theorem 2 (Stability of fractional-order LTI systems [24])**.** *A fractional-order system with an irrational-order transfer function $G(s)$ is bounded-input bounded-output stable (BIBO stable) if and only if (iff) the following condition is fulfilled:*

$$\exists M \in \mathbb{R} \colon |G(s)| \leq M, \quad \forall s \in \mathbb{C} \colon \operatorname{Re}(s) \geq 0.$$

Theorem 3 (Stability of fractional-order LTI systems of commensurate order [24])**.**
The fractional-order system with transfer function $H(\lambda) = B(\lambda)/A(\lambda)$, $\lambda = s^q$, and
commensurate order q is stable iff

$$|\arg(\lambda_i)| > q\frac{\pi}{2}, \quad \forall \lambda_i \in \mathbb{C} \colon A(\lambda_i) = 0.$$

2.4 Linear Viscoelasticity

In the following, the fundamental integer- and fractional-order models of linear one-dimensional viscoelastic phenomena are introduced. Assuming zero initial conditions these models are reduced to fractional-order transfer functions.

2.4.1 Integer-Order Models

The polymers studied in this thesis, polypropylene and polybutylene terephthalate, are semicrystalline materials. In a certain temperature range their behavior is viscoelastic [36]. "Viscoelastic" is an artificial word combining elastic and viscous. This topic will be clarified in more detail in this section.

In case of viscoelasticity, the deformation energy is split into two parts: the viscous dynamics dissipates the energy while the elastic part stores the mechanical energy. The material models are bounded by the ideal solid body on the one side and the ideal Newtonian fluid on the other side.

Elasticity is the property of a material to resist a distorting or deforming force and return to its original shape after removing the force [22]. The relationship between the stress $\sigma(t)$ and strain $\epsilon(t)$ for pure elastic components can be described by Hooke's law

$$\sigma(t) = E\epsilon(t) \tag{2.7}$$

with Young's modulus E, which is not constant for a material as it depends on many factors such as temperature, strain velocity and humidity [36]. Metals are elastic up to a certain stress limit at which permanent plastic deformation occurs. In contrast, the Hooke's area, in which the stress is in a constant ratio to the deformation, is often not present in plastics [36].

For ideal viscous components (Newtonian fluids), the stress is proportional to the local shear velocity, i.e.

$$\sigma(t) = \eta\dot{\epsilon}(t), \tag{2.8}$$

where η is the coefficient of viscosity which is a scalar constant of proportionality [23]. The viscosity of a fluid describes the linear resistance to shear flow and strain when a stress is applied [22].

To model real materials with properties somewhere in between, there are various approaches [22]. On the one hand integer-order elements can be combined, on the other hand fractional-order calculus can be applied.

To use integer-order derivatives, the elastic element is represented as a spring, while the ideal viscous element is realized as a dashpot [27]. These representations can be combined in parallel and/or series. The two simplest representations are the Maxwell model [27]

$$\frac{\mathrm{d}\epsilon(t)}{\mathrm{d}t} = \frac{1}{E}\frac{\mathrm{d}\sigma(t)}{\mathrm{d}t} + \frac{\sigma(t)}{\eta}, \qquad (2.9)$$

which connects two elements in series, and Voigt's model [27]

$$\sigma(t) = E\epsilon(t) + \eta\frac{\mathrm{d}\epsilon(t)}{\mathrm{d}t}, \qquad (2.10)$$

which uses the parallel arrangement. The schematic diagrams of the spring and dashpot representations of both models can be seen in Figure 2.1. More complex models are e.g. the Kelvin model that consists of the Voigt viscoelastic element (E_2 and η, in parallel) and the Hooke elastic element (E_1) in series, leading to

$$\frac{\mathrm{d}\sigma(t)}{\mathrm{d}t} + \alpha\sigma(t) = E_1\left(\frac{\mathrm{d}\epsilon(t)}{\mathrm{d}t} + \beta\epsilon(t)\right), \qquad (2.11)$$

and the Zener model, that is given by a combination of the Maxwell viscoelastic element (E_2 and η, in series) and the Hooke elastic element, such that

$$\frac{\mathrm{d}\sigma(t)}{\mathrm{d}t} + \beta\sigma(t) = \alpha\eta\frac{\mathrm{d}\epsilon(t)}{\mathrm{d}t} + \beta E_1\epsilon(t), \qquad (2.12)$$

where $\alpha = (E_1 + E_2)/\eta$ and $\beta = E_2/\eta$ [27]. The Zener model is also known as standard linear solid [16]. The mentioned models have been further improved to achieve higher accuracy. Then they consist of several Kelvin or Maxwell elements combined with Hooke's elastic element. This results in very complex relationships between stress and strain. The most general case are models of the form

$$\sum_{k=0}^{n} a_k\frac{\mathrm{d}^k\sigma(t)}{\mathrm{d}t^k} = \sum_{k=0}^{m} b_k\frac{\mathrm{d}^k\epsilon(t)}{\mathrm{d}t^k}. \qquad (2.13)$$
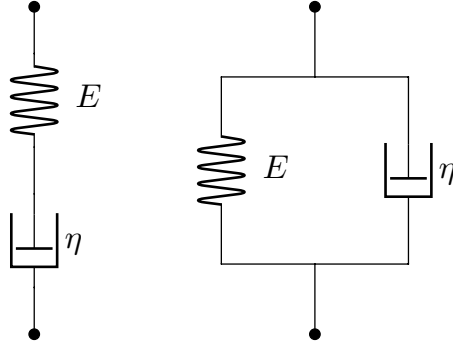
Figure 2.1: Schematic diagrams of the Maxwell model (left) and the Voigt model (right) [27].

The best adequacy can be achieved for $n = m$ [27]. These higher order models require a large set of parameters, which are difficult to measure individually and hard to estimate without overfitting. Therefore the fractional-order approach aims at parameter reduction while maintaining the accuracy of the model [13].

2.4.2 Fractional-Order Models

Based on the previous explanations, it is quite obvious to use fractional-order derivatives to model viscoelastic materials [27]. The material response is bounded by solid and fluid behavior, hence the order of differentiation should be between zero and one.

In [27] the primary form

$$\sigma(t) = E\mathcal{D}^\alpha \epsilon(t), \quad 0 < \alpha < 1, \tag{2.14}$$

is introduced. There are also multi-element models such as those for the integer-order models. Besides of combining Hooke and Newton elements, the Scott Blair element in (2.14) can be used in addition to integer-order elements [27].

The one-parameter model of Hooke and the two-parameter model (2.14) can also be further generalized by adding more terms on both sides, containing arbitrary-order derivatives of stress and strain [27]. There is e.g. the fractional Voigt model where the first time derivative in (2.10) is replaced by fractional-order derivative of order α [5], that is

$$\sigma(t) = E\left(\epsilon(t) + \tau^\alpha \mathcal{D}^\alpha \epsilon(t)\right) \tag{2.15}$$

with $\tau = \eta E^{-1}$. Following the same principle, the four-parameter (or generalized) Maxwell model can be defined in such a way that the elastic element and the vis-

cous element in (2.9) are replaced by viscoelastic elements [13]. The corresponding constitutive equation is

$$\sigma(t) + \tau^\alpha \mathcal{D}^\alpha \sigma(t) = E\tau^\beta \mathcal{D}^\beta \epsilon(t), \tag{2.16}$$

where $0 < \alpha \leq \beta < 1$. For this model the thermodynamic condition for a monotonically decreasing energy function is automatically fulfilled [13]. This is necessary because thermodynamics imposes restrictions on physically feasible processes by its second fundamental law, which means that the constitutive equation in general or the parameter functions or parameters in particular must guarantee a non-negative rate of mechanical energy dissipation [9].

Another representation is the generalized Zener model. This is a modification of the integer-order Zener model in (2.12). Only the time derivatives of stress and strain are replaced by fractional-order derivatives of order α and β, respectively [13]. It should be noted that $\alpha = \beta$, so that the thermodynamic conditions are fulfilled as before [13]. The resulting equation is

$$\sigma(t) + \tau^\beta \mathcal{D}^\beta \sigma(t) = (E_1 + E_2)\tau^\beta D^\beta \epsilon(t) + E_1 \epsilon(t), \tag{2.17}$$

where $\tau = \eta E_2^{-1}$ is the time constant of the Maxwell element [13].

In [13] it is stated that such formulations give an adequate description of real viscoelastic behavior with a limited number of material parameters. A disadvantage of fractional-order identification, however, is that these models are physically difficult to interpret [13] and a simulation in the time domain is complicated.

Applying the Laplace transform to the presented fractional-order models and assuming a stress-free material for $t < 0$ (zero initial conditions) yields the fractional-order transfer functions

$$G_{\text{Voigt}} = \frac{\epsilon(s)}{\sigma(s)} = \frac{1}{E}\frac{1}{\tau^\alpha s^\alpha + 1} = \frac{b_0}{a_1 s^\alpha + 1},$$

$$G_{\text{Maxwell}} = \frac{\epsilon(s)}{\sigma(s)} = \frac{\tau^\alpha s^\alpha + 1}{E\tau^\beta s^\beta} = \frac{b_1 s^\alpha + 1}{a_1 s^\beta},$$

$$G_{\text{Zener}} = \frac{\epsilon(s)}{\sigma(s)} = \frac{\tau^\beta s^\beta + 1}{(E_1 + E_2)\tau^\beta s^\beta + E_1} = \frac{b_1 s^\beta + 1}{a_1 s^\beta + a_0}.$$

2.5 Hydraulic Dashpot

Hydraulic cylinders convert the hydraulic energy provided by a pressure supply and transmitted by a hydraulic fluid into linear mechanical force and movement at the piston rod [7].

In relation to the uniform thrust phase, the starting and braking phases are generally small, so that hydraulic and mechanical parameters can be considered as mean values over the entire stroke [7]. The three phases are shown schematically in Figure 2.2.
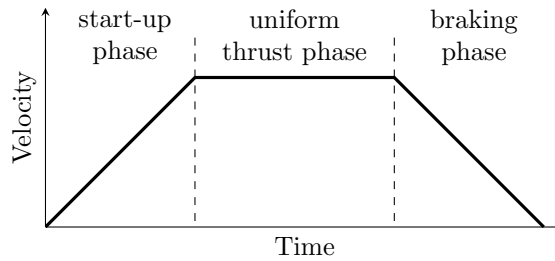
Figure 2.2: Characteristic motion sequence over time for a pushing dashpot with the idealized motion phases starting, moving and braking [7].

First, the hydraulic parameters of loss-free cylinders will be presented. The schematic structure of a dashpot and the forces acting on it are shown in Figure 2.3.
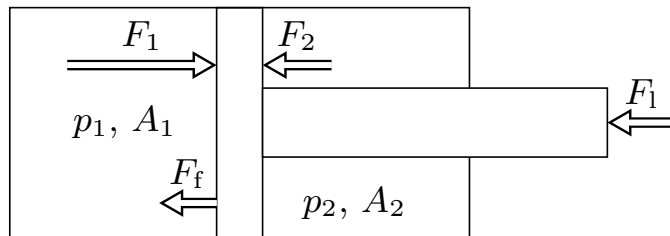
Figure 2.3: Schematic of a single rod, double acting hydraulic cylinder [7].

The (static) pressure difference of the cylinder or the pressure drop (load pressure) between the effective areas of the piston is defined as [7]

$$\Delta p = p_1 - p_2.$$

The effective areas, piston area A_1 and piston ring area A_2, can be calculated with

$$A_1 = \frac{\pi}{4} D^2, \quad A_2 = \frac{\pi}{4} \left(D^2 - d^2 \right),$$

where D and d are the diameters of the cylinder and the piston rod, respectively. In the case of a differential cylinder, the effective areas differ by the rod surface $A_r = \Delta A = A_1 - A_2$ [7]. The stroke volume then has two values for the double-acting design. The area ratio φ between cylinder and piston rod is [7]

$$\varphi = \frac{A_1}{A_2}.$$

The resulting force inside of the cylinder F_{cyl} can be described by

$$F_{\text{cyl}} = F_1 - F_2 = A_1 p_1 - A_2 p_2$$

with the maximum piston force F_1 and the counterforce F_2. This yields the equilibrium of forces

$$F_{\text{res}} = F_{\text{cyl}} - F_{\text{f}} - F_{\text{l}}, \tag{2.18}$$

where F_{res} is the resulting force, F_{l} is the load force and F_{f} is the force of friction.

The mechanical behavior of hydraulic dashpots depends on several factors, such as the damper design and dimensions, the properties of the hydraulic fluid and the operating conditions [30]. In many cases, especially at high frequencies where the damper force has a component that is in phase with the position of the cylinder arm, dampers exhibit a spring-like behavior [30]. Therefore, fluid cylinders can often be described by a combination of an ideal linear purely viscous damper and an ideal spring, either in parallel or series as explained in Section 2.4 [30]. This viscoelastic behavior is most likely caused by the hydraulic fluid in the dashpot, which is often a polymeric liquid [30]. Such fluids show a shear thinning behavior, i.e. their viscosity decreases with increasing shear strain [30]. Therefore, the models of the hydraulic fluid cannot be accurately described using (2.8) of the Newtonian fluid. These liquids often show an elastic behavior that cannot be captured for all flow conditions by generalized Newtonian models, e.g. the Carreau-Yasuda model [37]. For this reason, viscoelastic models have been developed to be able to describe the shear thinning nature of polymeric fluids. One very popular model is the Phan-Thien & Tanner model [32].

Following on from Section 2.4, it is therefore also possible to describe the viscoelastic behavior of a hydraulic dashpot with fractional-order transfer functions.

2.6 Noise

When performing real measurements, there is often undesired influence of noise, caused by measurement disturbances or noisy and inaccurate measuring devices [11]. Since real experiments are also carried out in this work, it is necessary to make some remarks on this subject.

In this thesis, identification problems are investigated, which can be described with a linear system of equations of the form $Ax = b$. For simplicity it is assumed that only the right-hand side vector b is subject to noise. Of course, the matrix A is often influenced by model or quadrature errors, too, but these errors are more systematic and therefore more complicated [11]. It is assumed that there exists an exact right-hand side given by $b_{\text{exact}} = Ax_{\text{exact}}$ if there is an exact solution x_{exact} [11]. The model for the right-hand side is therefore

$$b = b_{\text{exact}} + \xi,$$

where the vector $\xi \in \mathbb{R}^l$ represents the noise in the data. It is assumed that this is Gaussian white noise even if certainly other structural errors can have an influence. The elements of the noise vector are therefore drawn from the same Gaussian distribution with zero mean and standard deviation σ [11]. This is equivalent to

$$\text{Cov}(\xi) \equiv \text{E}(\xi\xi^\top) = \sigma^2 I,$$

where $\text{Cov}(\xi)$ is the covariance matrix, $\text{E}(\cdot)$ denotes the expected value, and σ^2 is the variance [11]. According to the definition of the noise vector, $\text{E}(\xi_i) = 0$ and $\text{E}(\xi) = 0$. The following also applies to the elements ξ_i [11]:

$$\text{E}(\xi_i^2) = \sigma^2,$$

$$\text{E}(|\xi_i|) = \sqrt{\frac{2}{\pi}}\sigma \approx 0.8\sigma.$$

The noise vector $\xi \in \mathbb{R}^l$ satisfies [11]

$$\text{E}(\|\xi\|_2^2) = l\sigma^2,$$

$$\text{E}(\|\xi\|_2) = \frac{\sqrt{2}\,\Gamma\left(\frac{l+1}{2}\right)}{\Gamma\left(\frac{l}{2}\right)}\sigma$$

with the gamma function $\Gamma(\cdot)$.

Based on the assumption that ξ is white noise, it follows that b_{exact} and ξ are uncorrelated and therefore $\mathrm{E}(b) = \mathrm{E}(b_{\text{exact}})$ applies. It follows that the covariance for the right-hand side b is [11]

$$\mathrm{Cov}(b) \equiv \mathrm{E}\Big((b - \mathrm{E}(b))(b - \mathrm{E}(b))^\top\Big) = \mathrm{E}(\xi\xi^\top) = \sigma^2 I.$$

The "naive" solution x can be written as

$$x = A^{-1}b = A^{-1}(b_{\text{exact}} + \xi) = x_{\text{exact}} + A^{-1}\xi$$

and the covariance matrix of x is [11]

$$\mathrm{Cov}(x) = A^{-1}\mathrm{Cov}(b)A^{-\top} = \sigma^2(A^\top A)^{-1}.$$

This covariance matrix shows the sensitivity of $x = A^{-1}b$ to data errors. Large elements imply high sensitivity [11]. This happens when A is very ill conditioned.

However, since this work is primarily concerned with frequency domain considerations, a second definition of white noise will be given. The vector ξ can be called white-noise vector if all frequencies present in this time series signal have the same probability [11]. The discrete Fourier transform of the noise vector $\hat{\xi}$ can be calculated with the relationships

$$\hat{\xi} = \overline{F}\xi,$$
$$\xi = \frac{1}{l}F\hat{\xi},$$

where F is the discrete Fourier matrix which is complex and symmetric and satisfies $\overline{F}F = lI$ [11]. Similar to the first definition, it is necessary that the covariance matrix of the discrete Fourier transform is a scaled identity for ξ to be a white noise vector [11]. From

$$\mathrm{Cov}(\hat{\xi}) = \mathrm{Cov}(\overline{F}\xi) = \overline{F}\mathrm{Cov}(\xi)F = l\sigma^2 I$$

it can be seen that both definitions are equivalent [11]. An advantage of the consideration in the frequency domain is also that signals which are not pure white noise in the time domain, but rather signal-correlated noise, can be regarded as "white-noise-like" when Fourier transformed [11]. An exact explanation and justification of this effect can be found in [11].

3 Fractional-Order System Identification in the Frequency Domain

In this chapter, the algorithms used for the postprocessing of the measured data are presented. This includes the extraction of the magnitude and phase information for plotting the data in a Bode diagram as well as the subsequent identification of the fractional-order transfer function. Additionally, the robustness of the identification approaches towards unknown structural parameters is validated using simulation data.

3.1 Extraction of Magnitude and Phase from Measurement Data

One of the most well-known and easiest methods to identify the transfer behavior of a linear system in the frequency domain is the excitation of the system input with an oscillation $u(t) = u_0 \sin(\omega_i t)$ [14]. For linear systems the output is also sinusoidal $y(t) = y_0 \sin(\omega_i t + \varphi)$. By calculating the amplitude ratio and phase shift of these sinusoidal signals, a discrete point of the desired frequency response can be found. The measurements have to be repeated for each frequency ω_i that is of interest [14]. The gain and phase of $G(\mathrm{j}\omega_i)$ can be calculated with

$$|G(\mathrm{j}\omega_i)| = \frac{y_0}{u_0},$$
$$\angle G(\mathrm{j}\omega_i) = -t_\varphi \omega_i,$$

where $t_\varphi = t_{out} - t_{in}$ is the time of the phase lag.

For real measurement series, which can be highly noisy, these necessary parameters must first be extracted from the recorded data. This can be realized with the Fast Fourier Transform (FFT) of the time series data. The FFT is a computationally

more time saving realization of the discrete Fourier transform [14]. The Fourier transform of a single sine function is a combination of delta impulses at the frequency of the given sine [10],

$$\mathcal{F}\{A\sin(2\pi\nu_0 x)\} = A\left[\frac{1}{2\mathrm{j}}\delta(\nu - \nu_0) - \frac{1}{2\mathrm{j}}\delta(\nu + \nu_0)\right],$$

with $\nu_0 = \omega_i/(2\pi)$. The amplitude of the FFT can then be used to determine the amplitude of the measured sine wave. However, the FFT has not only one amplitude peak due to the noisy data. This is shown in Figure 3.1 as an example for a real measurement series. Only the positive values are displayed here, as the function is symmetrical. Due to the regular spacing, the peaks could also be caused by a dead zone or other nonlinearity. The fundamental oscillation can be recognized by the highest peak in the amplitude curve (here marked with a red dot). The phase information can be calculated with the command `angle()` in MATLAB which uses the atan2() function.
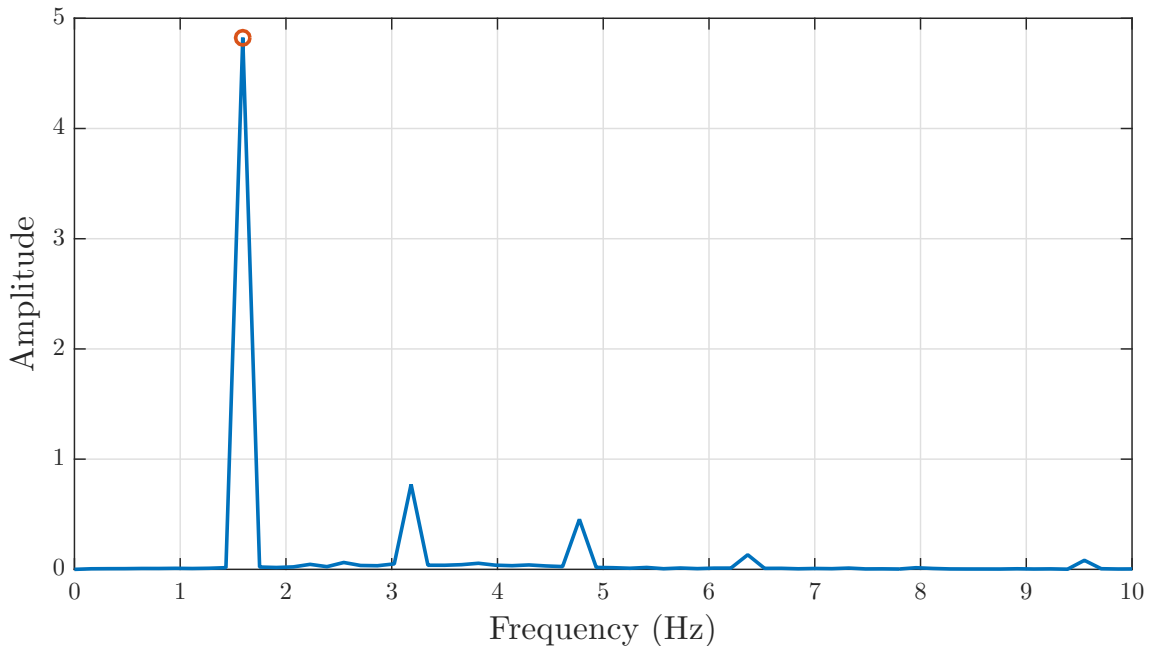
Figure 3.1: Amplitude of the FFT of an exemplary measurement data set.

3.2 Identification of the Transfer Function Coefficients

In this section, algorithms for the estimation of the parameters of fractional-order transfer functions with measurement data are presented. For the application of these algorithms, modeled transfer functions of the form (2.6) with the commensurate order q are considered, where $a_0 = 1$ is fixed (this choice is not restrictive [18]):

$$\widetilde{G}(s) = \frac{b_m s^{mq} + b_{m-1} s^{(m-1)q} + \ldots + b_1 s^q + b_0}{a_n s^{nq} + a_{n-1} s^{(n-1)q} + \ldots + a_1 s^q + 1}. \tag{3.1}$$

The identification problem in the frequency domain for fractional-order LTI systems is given by:

Problem 4 (Parameter Identification with Frequency Data)**.** *Given the commensurate order q, orders m, n of the pseudo polynomials in* (3.1) *and measurements of the output $Y_m(j\omega)$ and input $U_m(j\omega)$ for a set of frequencies $\Omega = \{\omega_1, \omega_2, \ldots, \omega_N\}$ minimize*

$$\min_p \sum_{k=1}^{N} J_k \left(\widetilde{G}(p, \omega_k), Y_m(j\omega_k), U_m(j\omega_k) \right), \tag{3.2}$$

where J_k is the cost function representing the identification error of the model transfer function $\widetilde{G}(s)$ at frequency ω_k and p is the parameter vector containing the coefficients $a_1, \ldots, a_n$ and $b_0, \ldots, b_m$.

This section introduces methods for solving minimization problems that belong to this form where m, n and q must be known in advance.

3.2.1 Algorithm Based on Time Domain Approaches

The first approach is basically motivated by time domain approaches [21]. It is known that the transfer function can be defined as the ratio of the measured outputs and inputs as well as the ratio of the pseudo polynomials

$$G(s) = \frac{Y(s)}{U(s)} = \frac{B(s^q)}{A(s^q)}. \tag{3.3}$$

Equation (3.3) motivates to define the error for a certain frequency ω_k, i.e.

$$E(\omega_k) = \epsilon(\omega_k) U_m(j\omega_k) A((j\omega_k)^q) = A((j\omega_k)^q) Y_m(j\omega_k) - B((j\omega_k)^q) U_m(j\omega_k), \tag{3.4}$$

which is obtained by multiplication with the error between model and plant,

$$\epsilon(\omega_k) = G_\mathrm{m}(\mathrm{j}\omega_k) - \widetilde{G}(\mathrm{j}\omega_k) = \frac{Y_\mathrm{m}(\mathrm{j}\omega_k)}{U_\mathrm{m}(\mathrm{j}\omega_k)} - \frac{B((\mathrm{j}\omega_k)^q)}{A((\mathrm{j}\omega_k)^q)}. \tag{3.5}$$

In relation to Problem 4 the cost function reads

$$J(\omega_k) = |E(\omega_k)|^2.$$

The error definition in (3.4) can be rewritten as

$$A((\mathrm{j}\omega)^q)Y_\mathrm{m}(\mathrm{j}\omega) = B((\mathrm{j}\omega)^q)U_\mathrm{m}(\mathrm{j}\omega) + E(\omega)$$
$$\Leftrightarrow \quad \left((a_n(\mathrm{j}\omega)^{nq} + \ldots + a_1(\mathrm{j}\omega)^q + 1\right)Y_\mathrm{m}(\mathrm{j}\omega)$$
$$= \left(b_m(\mathrm{j}\omega)^{mq} + \ldots + b_1(\mathrm{j}\omega)^q + b_0\right)U_\mathrm{m}(\mathrm{j}\omega) + E(\omega)$$
$$\Leftrightarrow \quad Y_\mathrm{m}(\mathrm{j}\omega) = \left(b_m(\mathrm{j}\omega)^{mq} + \ldots + b_1(\mathrm{j}\omega)^q + b_0\right)U_\mathrm{m}(\mathrm{j}\omega)$$
$$- \left(a_n(\mathrm{j}\omega)^{nq} + \ldots + a_1(\mathrm{j}\omega)^q\right)Y_\mathrm{m}(\mathrm{j}\omega) + E(\omega).$$

Let the vector $p = [a_1, \ldots, a_n, b_0, \ldots, b_m]^\top$ define all linear parameters. This results in the linear system

$$Y_\mathrm{m}(\mathrm{j}\omega) = S(\mathrm{j}\omega)p + E(\omega)$$

with the matrix of measurements

$$S(\mathrm{j}\omega) = \begin{bmatrix} -(\mathrm{j}\omega)^q Y_\mathrm{m}(\mathrm{j}\omega) \\ \vdots \\ -(\mathrm{j}\omega)^{nq} Y_\mathrm{m}(\mathrm{j}\omega) \\ U_\mathrm{m}(\mathrm{j}\omega) \\ (\mathrm{j}\omega)^q U_\mathrm{m}(\mathrm{j}\omega) \\ \vdots \\ (\mathrm{j}\omega)^{mq} U_\mathrm{m}(\mathrm{j}\omega) \end{bmatrix}^\top.$$

The common least squares approach is used to find an optimal solution for the minimization problem (3.2) with the cost function

$$J(\omega_k) = |Y_\mathrm{m}(\mathrm{j}\omega_k) - S(\mathrm{j}\omega_k)p|^2. \tag{3.6}$$

The minimization problem has a unique solution under the assumption that S has full rank. This is the case when sufficient measurements are available at different

frequencies. The optimal parameter vector can then be calculated using

$$p = S^+(\mathrm{j}\omega)Y_\mathrm{m}(\mathrm{j}\omega) \tag{3.7}$$

with the Moore-Penrose inverse $S^+(\mathrm{j}\omega)$ of matrix $S(\mathrm{j}\omega)$.

Since the fractional calculus is limited to real values in this work, the calculation of $p \in \mathbb{R}^{m+n+1}$ is adjusted. To avoid complex numbers, the real and imaginary parts of $S(\mathrm{j}\omega)$ and $Y_\mathrm{m}(\mathrm{j}\omega)$ are separated. For readability reasons the frequency argument is omitted here. Then

$$
\begin{aligned}
\|Y_\mathrm{m} - Sp\|_2^2 &= \|\mathrm{Re}\,(Y_\mathrm{m} - Sp) + \mathrm{j}\,\mathrm{Im}\,(Y_\mathrm{m} - Sp)\|_2^2 \\
&= \|\mathrm{Re}\,(Y_\mathrm{m}) - \mathrm{Re}\,(S)\,p + \mathrm{j}\,(\mathrm{Im}\,(Y_\mathrm{m}) - \mathrm{Im}\,(S)\,p)\|_2^2 \\
&= (\mathrm{Re}\,(Y_\mathrm{m}) - \mathrm{Re}\,(S)\,p + \mathrm{j}\,(\mathrm{Im}\,(Y_\mathrm{m}) - \mathrm{Im}\,(S)\,p))^H \\
&\quad (\mathrm{Re}\,(Y_\mathrm{m}) - \mathrm{Re}\,(S)\,p + \mathrm{j}\,(\mathrm{Im}\,(Y_\mathrm{m}) - \mathrm{Im}\,(S)\,p)) \\
&= (\mathrm{Re}\,(Y_\mathrm{m}) - \mathrm{Re}\,(S)\,p - \mathrm{j}\,(\mathrm{Im}\,(Y_\mathrm{m}) - \mathrm{Im}\,(S)\,p))^\top \\
&\quad (\mathrm{Re}\,(Y_\mathrm{m}) - \mathrm{Re}\,(S)\,p + \mathrm{j}\,(\mathrm{Im}\,(Y_\mathrm{m}) - \mathrm{Im}\,(S)\,p)) \\
&= (\mathrm{Re}\,(Y_\mathrm{m}) - \mathrm{Re}\,(S)\,p)^\top\,(\mathrm{Re}\,(Y_\mathrm{m}) - \mathrm{Re}\,(S)\,p) \\
&\quad + (\mathrm{Im}\,(Y_\mathrm{m}) - \mathrm{Im}\,(S)\,p)^\top\,(\mathrm{Im}\,(Y_\mathrm{m}) - \mathrm{Im}\,(S)\,p) \\
&= \|\mathrm{Re}\,(Y_\mathrm{m}) - \mathrm{Re}\,(S)\,p\|_2^2 + \|\mathrm{Im}\,(Y_\mathrm{m}) - \mathrm{Im}\,(S)\,p\|_2^2 \\
&= \left\| \begin{bmatrix} \mathrm{Re}\,(Y_\mathrm{m}) \\ \mathrm{Im}\,(Y_\mathrm{m}) \end{bmatrix} - \begin{bmatrix} \mathrm{Re}\,(S) \\ \mathrm{Im}\,(S) \end{bmatrix} p \right\|_2^2 .
\end{aligned}
$$

The new matrices are defined as

$$M := \begin{bmatrix} \mathrm{Re}\,(S(\mathrm{j}\omega)) \\ \mathrm{Im}\,(S(\mathrm{j}\omega)) \end{bmatrix}, \qquad N := \begin{bmatrix} \mathrm{Re}\,(Y_\mathrm{m}(\mathrm{j}\omega)) \\ \mathrm{Im}\,(Y_\mathrm{m}(\mathrm{j}\omega)) \end{bmatrix}$$

and the parameter vector p can be calculated as in (3.7) with

$$p = M^+(\mathrm{j}\omega)N(\mathrm{j}\omega).$$

3.2.2 Levy's Algorithm

More advanced methods of finding the coefficients of a fractional-order transfer function are summarized in [34]. These algorithms are based on considerations of integer order but can easily be transferred to cases with fractional-order models.

The best-known method was developed by Levy and will be explained first [18]. The model plant has the same structure as shown in (3.1) with known structural parameters m, n and q. The frequency response of $\widetilde{G}$ is given by

$$\widetilde{G}(\mathrm{j}\omega) = \frac{\displaystyle\sum_{k=0}^{m} b_k \, (\mathrm{j}\omega)^{kq}}{1 + \displaystyle\sum_{k=1}^{n} a_k \, (\mathrm{j}\omega)^{kq}} = \frac{B((\mathrm{j}\omega)^q)}{A((\mathrm{j}\omega)^q)} = \frac{\alpha(\omega) + \mathrm{j}\beta(\omega)}{\gamma(\omega) + \mathrm{j}\delta(\omega)},$$

where α, β, γ and δ are the real and imaginary parts of $B((\mathrm{j}\omega)^q)$ and $A((\mathrm{j}\omega)^q)$.

The cost function can again be motivated using the error definition $\epsilon(\omega_k)$ from (3.5) [34]:

$$J_{\mathrm{Levy}}(\omega_k) = |E_{\mathrm{Levy}}(\omega_k)|^2,$$

with

$$E_{\mathrm{Levy}}(\omega_k) = \epsilon(\omega_k)A((\mathrm{j}\omega_k)^q) = A((\mathrm{j}\omega_k)^q)G_{\mathrm{m}}(\mathrm{j}\omega_k) - B((\mathrm{j}\omega_k)^q). \qquad (3.8)$$

Note that this error is identical to that of the previous approach if $U_{\mathrm{m}}(\mathrm{j}\omega_k) = 1$. By dropping the dependency on the frequency argument, (3.8) can be transformed into

$$\begin{aligned}
E_{\mathrm{Levy}} &= (\gamma + \mathrm{j}\delta)\left(\mathrm{Re}\,(G_{\mathrm{m}}) + \mathrm{j}\,\mathrm{Im}\,(G_{\mathrm{m}})\right) - \alpha - \mathrm{j}\beta \\
&= (\gamma\,\mathrm{Re}\,(G_{\mathrm{m}}) - \delta\,\mathrm{Im}\,(G_{\mathrm{m}}) - \alpha) + \mathrm{j}\,(\delta\,\mathrm{Re}\,(G_{\mathrm{m}}) + \gamma\,\mathrm{Im}\,(G_{\mathrm{m}}) - \beta)\,.
\end{aligned}$$

Then the square of the norm of E_{Levy} is

$$\|E_{\mathrm{Levy}}\|^2 = (\gamma\,\mathrm{Re}\,(G_{\mathrm{m}}) - \delta\,\mathrm{Im}\,(G_{\mathrm{m}}) - \alpha)^2 + (\delta\,\mathrm{Re}\,(G_{\mathrm{m}}) + \gamma\,\mathrm{Im}\,(G_{\mathrm{m}}) - \beta)^2\,.$$

After differentiating $\|E_{\mathrm{Levy}}(a_1, \ldots, a_n, b_0, \ldots, b_n, q)\|^2$ with respect to one of the coefficients a_i and b_i, the results are set equal to zero

$$\begin{aligned}
\frac{\partial \|E_{\mathrm{Levy}}\|^2}{\partial a_i} &= 2\left(\mathrm{Re}\,(G_{\mathrm{m}})\,\gamma - \mathrm{Im}\,(G_{\mathrm{m}})\,\delta - \alpha\right)\mathrm{Re}\,(G_{\mathrm{m}})\,R_{k,i} \\
&\quad + 2\left(\mathrm{Re}\,(G_{\mathrm{m}})\,\delta + \mathrm{Im}\,(G_{\mathrm{m}})\,\gamma - \beta\right)\mathrm{Im}\,(G_{\mathrm{m}})\,R_{k,i} \\
&\quad - 2\left(\mathrm{Re}\,(G_{\mathrm{m}})\,\gamma - \mathrm{Im}\,(G_{\mathrm{m}})\,\delta - \alpha\right)\mathrm{Im}\,(G_{\mathrm{m}})\,I_{k,i} \\
&\quad + 2\left(\mathrm{Re}\,(G_{\mathrm{m}})\,\delta + \mathrm{Im}\,(G_{\mathrm{m}})\,\gamma - \beta\right)\mathrm{Re}\,(G_{\mathrm{m}})\,I_{k,i} \overset{!}{=} 0, \qquad (3.9) \\
\frac{\partial \|E_{\mathrm{Levy}}\|^2}{\partial b_i} &= 2\left(\mathrm{Re}\,(G_{\mathrm{m}})\,\gamma - \mathrm{Im}\,(G_{\mathrm{m}})\,\delta - \alpha\right)R_{k,i} \\
&\quad + 2\left(\mathrm{Re}\,(G_{\mathrm{m}})\,\delta + \mathrm{Im}\,(G_{\mathrm{m}})\,\gamma - \beta\right)R_{k,i} \overset{!}{=} 0, \qquad (3.10)
\end{aligned}$$

using the shorthand notations $R_{k,i} = \text{Re}\,(j\omega_k)^{iq}$ and $I_{k,i} = \text{Im}\,(j\omega_k)^{iq}$. The difference to Levy's identification method for integer-order models can be seen in the term $(j\omega_k)^{iq}$ [34]. If $q = 1$, the real and imaginary parts of $(j\omega_k)^i$, $k \in \mathbb{N}$, are $\pm\omega_k^i$ or $\pm j\omega_k^i$ and as in [18] Levy's original formula is obtained.

A linear system can be created out of the $n + m + 1$ equations given by (3.9) and (3.10) [34]. The desired coefficients $a = [a_1, \ldots, a_n]^\top$ and $b = [b_0, \ldots, b_m]^\top$ can be found by solving this linear system. The number of measured frequencies will be referred to N in the following. The system can be written as

$$Mp = \begin{bmatrix} M_{11} & M_{12} \\ M_{21} & M_{22} \end{bmatrix} \begin{bmatrix} b \\ a \end{bmatrix} = \begin{bmatrix} N_1 \\ N_2 \end{bmatrix} \tag{3.11}$$

with

$$M_{11_{l,c}} = \sum_{k=1}^{N} -R_{k,l}R_{k,c} - I_{k,l}R_{k,c}, \quad l = 0 \ldots m, \quad c = 0 \ldots m,$$

$$M_{12_{l,c}} = \sum_{k=1}^{N} +R_{k,l}R_{k,c}\,\text{Re}\,(G_\text{m}\,(j\omega_k)) + I_{k,l}R_{k,c}\,\text{Im}\,(G_\text{m}\,(j\omega_k))$$
$$- R_{k,l}I_{k,c}\,\text{Im}\,(G_\text{m}\,(j\omega_k)) + I_{k,l}I_{k,c}\,\text{Re}\,(G_\text{m}\,(j\omega_k)),$$
$$l = 0 \ldots m, \quad c = 1 \ldots n,$$

$$M_{21_{l,c}} = \sum_{k=1}^{N} -R_{k,l}R_{k,c}\,\text{Re}\,(G_\text{m}\,(j\omega_k)) + I_{k,l}R_{k,c}\,\text{Im}\,(G_\text{m}\,(j\omega_k))$$
$$- R_{k,l}I_{k,c}\,\text{Im}\,(G_\text{m}\,(j\omega_k)) - I_{k,l}I_{k,c}\,\text{Re}\,(G_\text{m}\,(j\omega_k)),$$
$$l = 1 \ldots n, \quad c = 0 \ldots m,$$

$$M_{22_{l,c}} = \sum_{k=1}^{N} \left[(\text{Re}\,(G_\text{m}\,(j\omega_k)))^2 + (\text{Im}\,(G_\text{m}\,(j\omega_k)))^2\right] [R_{k,l}R_{k,c} + I_{k,l}I_{k,c}],$$
$$l = 1 \ldots n, \quad c = 1 \ldots n,$$

$$N_{1_{l,1}} = \sum_{k=1}^{N} -R_{k,l}\,\text{Re}\,(G_\text{m}\,(j\omega_k)) - I_{k,l}\,\text{Im}\,(G_\text{m}\,(j\omega_k)), \quad l = 0 \ldots m,$$

$$N_{2_{l,1}} = \sum_{k=1}^{N} -R_{k,l}\left((\text{Re}\,(G_\text{m}\,(j\omega_k)))^2 + (\text{Im}\,(G_\text{m}\,(j\omega_k)))^2\right), \quad l = 1 \ldots n.$$

The optimal parameter vector in (3.11) can now be calculated similar to the previous method in (3.7) using the inverse of M.

The application of this algorithm is limited by the type of frequency response function that can be fitted. Functions that have poles at the origin cannot be used [18]. However, it is possible to adjust the specified transfer function if it does not meet the requirements. For this purpose it has to be multiplied by $(j\omega)^n$, where n must be large enough to reduce the absolute magnitude of the function at zero frequency to a finite value [18].

3.2.3 Vinagre's Weights

The problem of the proposed algorithms is that low-frequency data have less influence on the fit than high-frequency data [34]. This is caused by the weighted error $E_{\text{Levy}}(\omega_k) = \epsilon(\omega_k)A((j\omega_k)^q)$, because the higher ω_k is, the higher $A((j\omega_k)^q)$ becomes and the more influence the specific frequency has on the cost function. This also applies for the first method with the additional term $U_{\text{m}}(j\omega_k)$. Therefore, the resulting transfer functions are more accurate for higher frequencies. To counteract this, various approaches have been developed to introduce a weighting w_k for the cost function

$$J_w(\omega_k) = |E_{\text{Levy}}(\omega_k)|^2 w_k. \tag{3.12}$$

A first approach is due to Vinagre [34]. He defined the additional weights as follows:

$$w_k = \frac{\varphi_k}{\omega_k^2}, \tag{3.13}$$

with

$$\varphi_k = \begin{cases} \dfrac{\omega_2 - \omega_1}{2}, & \text{if } k = 1 \\[2mm] \dfrac{\omega_{k+1} - \omega_{k-1}}{2}, & \text{if } 1 < k < N \\[2mm] \dfrac{\omega_N - \omega_{N-1}}{2}, & \text{if } k = N, \end{cases}$$

where $\omega_k \in \Omega = \{\omega_1, \ldots, \omega_N\}$. These weights are multiplied by each corresponding summand in the definitions of M_{11}, M_{12}, M_{21}, M_{22}, N_1 and N_2. In short, this is an attempt to reduce the influence of the higher frequencies to an appropriate level by dividing in general by the frequencies. That means, using Viangre's weights the cost function

$$J_w(\omega_k) = |\epsilon(\omega_k)A((j\omega_k)^q)|^2 \frac{\varphi_k}{\omega_k^2} \tag{3.14}$$

is minimized.

This improvement can also be used to enhance the first proposed method. Therefore, the individual weights are combined in vector $w = [w_1, \ldots, w_N]^\top$ to weight $S(\mathrm{j}\omega)$ and $Y_\mathrm{m}(\mathrm{j}\omega)$ element wise:

$$Y_\mathrm{m}(\mathrm{j}\omega) \otimes w = (S(\mathrm{j}\omega) \otimes w)\, p + E(\omega),$$

where $\otimes$ denotes the Kronecker product. This means the cost function of method 1 changes to

$$J(\omega_k) = |Y_\mathrm{m}(\mathrm{j}\omega_k) - S(\mathrm{j}\omega_k)p|^2 \frac{\varphi_k}{\omega_k^2}.$$

3.2.4 Iterative Method of Sanathanan and Koerner

Another solution for the problem of the different influence of the frequencies was introduced by Sanathanan and Koerner [29]. The previous weights are now replaced by an iterative procedure. This means that the cost function is

$$J_w(\omega_k) = |\epsilon(\omega_k)A((\mathrm{j}\omega_k)^q)|^2 \frac{1}{|A_{L-1}\left((\omega_k)^q\right)|^2},$$

where L is the iteration number and A_{L-1} is the denominator found in the previous iteration [34]. This choice of weights is intended to completely eliminate the influence of $A((\mathrm{j}\omega_k)^q)$ on the error $\epsilon(\omega_k)$, which can be seen when the weight function is inserted in the error definition [29], hence

$$E_w(\omega) = \frac{E_{\mathrm{Levy},L}}{A_{L-1}((\mathrm{j}\omega)^q)} = \frac{A_L((\mathrm{j}\omega)^q)\epsilon(\omega)}{A_{L-1}((\mathrm{j}\omega)^q)} = \frac{A_L((\mathrm{j}\omega)^q)G_\mathrm{m}(\mathrm{j}\omega)}{A_{L-1}((\mathrm{j}\omega)^q)} - \frac{B_L((\mathrm{j}\omega)^q)}{A_{L-1}((\mathrm{j}\omega)^q)}.$$

In the first iteration, A_0 is set equal to 1. The influence of the weighting becomes smaller, because the subsequent iterations converge rapidly and $E_w(\omega)$ tends to be equal to $\epsilon(\omega)$ [29].

The resulting coefficients a_i, $i \in \{1, \ldots, n\}$, in each iteration are used to calculate the weighting for the next iteration. In this work, the number of iterations is set to 10 because too many iterations may cause numerical errors which can spoil the result. In general, this number depends upon the desired accuracy in the values of the coefficients and the nature of the transfer function [29].

3.2.5 Iterative Method of Lawrence and Rogers

The last improvement of Levy's algorithm, listed in [34], is an iterative method that avoids solving a set of linear equations compared to the previous methods. This

algorithm was introduced by Lawrence and Rogers [17]. Using this method, there is no need to solve the system again when new data from new frequencies appear [34]. Each frequency is included simultaneously.

In view of (3.1) the frequency response can be written as

$$\widetilde{G}(\mathrm{j}\omega) = \frac{b^\top v(\mathrm{j}\omega)}{1 + a^\top u(\mathrm{j}\omega)},$$

where $v = \begin{bmatrix} 1 & (\mathrm{j}\omega)^q & \dots & (\mathrm{j}\omega)^{mq} \end{bmatrix}^\top$ and $u = \begin{bmatrix} (\mathrm{j}\omega)^q & \dots & (\mathrm{j}\omega)^{nq} \end{bmatrix}^\top$. Again, n, m and q are known. The same cost function as for Levy's algorithm J_{Levy} is optimized here, where the error can be written as

$$E_{\mathrm{Levy}} = AG_{\mathrm{m}} - B = G_{\mathrm{m}} + a^\top G_{\mathrm{m}} u - b^\top v, \tag{3.15}$$

for simplification without the dependency on ω. By defining the parameter vector $p = \begin{bmatrix} b & a \end{bmatrix}^\top$ and the vector $r = \begin{bmatrix} v & -G_{\mathrm{m}} u \end{bmatrix}^\top$, (3.15) reads

$$E_{\mathrm{Levy}} = G_{\mathrm{m}} - p^\top r.$$

This changes the quality functional to

$$\begin{aligned}
\|E_{\mathrm{Levy}}\|^2 &= \left(G_{\mathrm{m}} - p^\top r \right) \overline{\left(G_{\mathrm{m}} - p^\top r \right)}^\top \\
&= G_{\mathrm{m}} \overline{G_{\mathrm{m}}} - G_{\mathrm{m}} \overline{r}^\top p - \overline{G_{\mathrm{m}}} p^\top r + p^\top r \overline{r}^\top p.
\end{aligned}$$

A weighting w for the minimization is also applied. This can be obtained either from the Vinagre approach or from the iterative method of Sanathanan and Koerner.

Similar to the general Levy method, $\|E_{\mathrm{Levy}}\|^2 w^2$ is differentiated with respect to the parameter vector p

$$\frac{\partial \|E_{\mathrm{Levy}}\|^2 w^2}{\partial p} = \left(-G_{\mathrm{m}} \overline{r} - \overline{G_{\mathrm{m}}} r + r \overline{r}^\top p + \overline{r} r^\top p \right) w^2$$

and is set equal to zero, thus

$$w^2 \left(r \overline{r}^\top + \overline{r} r^\top \right) p = w^2 \left(G_{\mathrm{m}} \overline{r} + \overline{G_{\mathrm{m}}} r \right).$$

The extension to all measured frequencies is then

$$\sum_{k=1}^{N} w_k^2 \left(r_k \overline{r_k}^\top + \overline{r_k} r_k^\top \right) p = \sum_{k=1}^{N} w_k^2 \left(G_{\mathrm{m}}(\mathrm{j}\omega_k) \overline{r_k} + \overline{G_{\mathrm{m}}(\mathrm{j}\omega_k)} r_k \right). \tag{3.16}$$

With this equation a new matrix can be introduced:

$$H_N^{-1} = \sum_{k=1}^{N} w_k^2 \left(r_k \overline{r_k}^\top + \overline{r_k} r_k^\top \right).$$

(3.17)

From this also follows

$$H_N^{-1} p_N = \sum_{k=1}^{N} w_k^2 \left(G_m(j\omega_k) \overline{r_k} + \overline{G_m(j\omega_k)} r_k \right),$$

(3.18)

where p_N is the parameter vector obtained using N frequencies.

Equation (3.16) can be poorly conditioned despite scaling, especially if a wide frequency range is required to characterize the system [17]. Furthermore, adding data points leads to a complete reformulation, and it is very difficult to use the matching process online [17].

The essential algorithm for the parameters after N frequency data points, stated in [17], consists of

$$Z_N = H_{N-1} \left(I - \frac{\mathrm{Re}\,(r_N)\,\mathrm{Re}\left(r_N^\top\right) H_{N-1}}{\frac{1}{2w_N^2} + \mathrm{Re}\left(r_N^\top\right) H_{N-1}\,\mathrm{Re}\,(r_N)} \right),$$

(3.19)

$$H_N = Z_N \left(I - \frac{\mathrm{Im}\,(r_N)\,\mathrm{Im}\left(r_N^\top\right) Z_N}{\frac{1}{2w_N^2} + \mathrm{Im}\left(r_N^\top\right) Z_N\,\mathrm{Im}\,(r_N)} \right),$$

(3.20)

$$p_N = p_{N-1} + H_N w_N^2 \left(r_N \left(\overline{G_m(j\omega_N)} - \overline{r_N^\top} p_{N-1} \right) + \overline{r_N} \left(G_m(j\omega_N) - r_N^\top p_{N-1} \right) \right),$$

(3.21)

where Z_N and $H_N \in \mathbb{R}^{(n+m+1)\times(n+m+1)}$. For a detailed derivation [17] or [34] can be consulted.

Some initial values for H and p have to be selected beforehand. One possibility to calculate them is the application of (3.17) and (3.18) with a few frequencies [34]. The remaining data can then be used for the algorithm.

Another possible initial estimate of the parameter H_0 is $\left(\frac{1}{\epsilon}\right) I$ where ϵ is a number as small as computationally feasible [17]. The parameter vector can be chosen to be zero at the beginning.

With these initial values, (3.19) to (3.21) can now be calculated in order to get the optimal parameter vector p. If sufficient data points are available, an acceptable

model can be obtained with a single pass through the data [17]. However, an improved estimate can be achieved by using the obtained parameter vector as a new initial guess [17]. The weights can also be adjusted accordingly.

3.3 Optimization

Another possibility for the parameter identification is to use an optimization instead of the just introduced algorithms. This has the advantage that not only a limited number of different q can be examined, for each of which the transfer function has to be determined. This means that the accuracy of the best fitting q can be increased. Furthermore, the stability of the transfer function is not guaranteed by the previous algorithms and must therefore be additionally checked afterwards. When using an optimization, it is not necessary to use weights to keep a constant influence of the noise, since a transformation into a linear parameter form is not required.

A disadvantage of the optimization, however, is that only a local minimum and no global minimum could be found. This is illustrated by an example in Section 3.4. A far more important drawback is that the optimization is computationally expensive compared to the matrix multiplications when using the algorithms from Section 3.2.

Problem 5 (Optimization Problem). *The optimization problem is defined as*

$$\min_{x} \quad f(x)$$
$$subject\ to \quad lb \leq x \leq ub,$$
$$c(x) \leq 0,$$

where $f(x) = \left\| G_{\mathrm{m}}(\omega) - \widetilde{G}(\omega, x) \right\|^2$, $x = [a_1, \ldots, a_n, b_0, \ldots, b_m, q]^\top \in \mathbb{R}^{n+m+2}$, $lb = [l_1, \ldots, l_n, 0]^\top$ *and* $ub = [u_0, \ldots, u_m, 1]^\top$, $l_i, u_j \in \mathbb{R}$. *The nonlinear inequalities* $c(x)$ *are used to ensure stability of the modeled transfer function* $\widetilde{G}$ *by the application of Theorem 3:*

$$c(x) = q\frac{\pi}{2} - |\arg(\lambda_i)| + \epsilon, \quad \epsilon > 0.$$

In the following, the lower and upper bounds are chosen as $lb = [-100, \ldots, -100, 0]^\top$ and $ub = [100, \ldots, 100, 1]^\top$ to reduce the search space of the optimization and because the coefficients obtained with the algorithms from Section 3.2 for the polymer samples are in this range.

3.4 Simulation Studies

In this section, the robustness of the identification approaches against unknown structural parameters such as the commensurate order or the general system order is validated using simulation data.

3.4.1 Comparison of the Proposed Algorithms for the Identification of the Parameter Vector

The algorithms presented in Section 3.2 are now verified. The following parameters are specified for this purpose: For 25 frequencies ω_k ranging from $\omega_1 = 0.6\,\frac{\text{rad}}{\text{s}}$ to $\omega_{25} = 300\,\frac{\text{rad}}{\text{s}}$ the inputs $U_k = 1$ according to the frequency with index k and the transfer function pseudo polynomials $A_{\text{ref}}(s^q)$ and $B_{\text{ref}}(s^q)$ are generated. A Gaussian distributed, zero mean noise is added to the output $Y(\text{j}\omega_k)$, so

$$Y(\text{j}\omega_k) = \frac{B_{\text{ref}}((\text{j}\omega_k)^q)}{A_{\text{ref}}((\text{j}\omega_k)^q)}U_k + \Xi(\text{j}\omega_k), \tag{3.22}$$

where $\Xi(\text{j}\omega_k)$ is the Fourier transform of the noise vector ξ that consists of independent entries drawn from the standard normal distribution $\mathcal{N}(0, \sigma)$.

The root-mean-square error (RMSE) is calculated to determine the accuracy of the modeled transfer functions,

$$\text{RMSE} = \frac{1}{N}\sqrt{\sum_{k=1}^{N}\left|G_{\text{ref}}(\text{j}\omega_k) - \widetilde{G}(\text{j}\omega_k)\right|^2}, \tag{3.23}$$

where $G_{\text{ref}}(\text{j}\omega_k)$ are the complex reference transfer function data.

For low signal to noise ratios, all algorithms provide the correct transfer function, i.e. the RMSE is in the range of 10^{-17}, which corresponds to a numerical error. The error values for the parameter identification using the different methods under the influence of noise as in (3.22) are now compared using a simple example. The specified transfer function is:

$$G_{\text{spec}} = \frac{1}{1 + s^{0.5}}. \tag{3.24}$$

A noise model $G_{\text{noise}}(\text{j}\omega)$ is generated using this transfer function and (3.22) with $\sigma = 0.001$. Then, each of the algorithms that are summarized and further described in Table 3.1 are used to calculate the coefficients of the FOTF using $G_{\text{noise}}(\text{j}\omega)$ as

artificial measurement data. Additional, q, n and m have to be specified. This calculation is repeated 10000 times with different noise vectors.

Table 3.1: Summarized methods.

	Method
1	Output error method with Vinagre's weights
2	Levy's method with Vinagre's weights
3	Levy's method with iterative method of Sanathanan and Koerner
4	Levy's method with iterative method of Lawrence and Rogers and Vinagre's weights
5	Levy's method with iterative method of Lawrence and Rogers and iterative method of Sanathanan and Koerner

Here the results for the correct orders are given as an example. Further tables can be found in Appendix A.1. The averaged coefficients of the pseudo polynomials, $a = [1, a_1, \ldots, a_n]$ and $b = [b_0, \ldots, b_m]$, as well as their variances are shown in Table 3.2.

Table 3.2: Simulation studies: algorithms (averaged parameter vector over 10000 runs and variance of the results with $\sigma = 0.001$, $q = 0.5$, $n = 1$ and $m = 0$).

Method	Averaged coefficients	Variance of the coefficients $\times 10^{-4}$
1	$a = \begin{bmatrix} 1 & 0.9990 \end{bmatrix}$, $b = \begin{bmatrix} 0.9996 \end{bmatrix}$	$\sigma_a^2 = \begin{bmatrix} 0 & 3.7071 \end{bmatrix}$, $\sigma_b^2 = \begin{bmatrix} 1.2010 \end{bmatrix}$
2	$a = \begin{bmatrix} 1 & 0.9982 \end{bmatrix}$, $b = \begin{bmatrix} 0.9990 \end{bmatrix}$	$\sigma_a^2 = \begin{bmatrix} 0 & 1.3618 \end{bmatrix}$, $\sigma_b^2 = \begin{bmatrix} 0.4828 \end{bmatrix}$
3	$a = \begin{bmatrix} 1 & 0.9979 \end{bmatrix}$, $b = \begin{bmatrix} 0.9988 \end{bmatrix}$	$\sigma_a^2 = \begin{bmatrix} 0 & 1.3907 \end{bmatrix}$, $\sigma_b^2 = \begin{bmatrix} 0.4570 \end{bmatrix}$
4	$a = \begin{bmatrix} 1 & 1.0000 \end{bmatrix}$, $b = \begin{bmatrix} 1.0000 \end{bmatrix}$	$\sigma_a^2 = \begin{bmatrix} 0 & 1.2513 \end{bmatrix}$, $\sigma_b^2 = \begin{bmatrix} 0.0893 \end{bmatrix}$
5	$a = \begin{bmatrix} 1 & 0.9974 \end{bmatrix}$, $b = \begin{bmatrix} 0.9987 \end{bmatrix}$	$\sigma_a^2 = \begin{bmatrix} 0 & 0.4281 \end{bmatrix}$, $\sigma_b^2 = \begin{bmatrix} 0.3563 \end{bmatrix}$

Table 3.3 shows the averaged RMSEs and variances for G_{spec} and G_{noise} as reference model. To validate the performance of the algorithms, the RMSE with respect to G_{spec} is of particular interest, as it shows how well the known model has been fitted. The second RMSE has also been added for completeness to see if the noise causes serious deviations.

It is recognizable that the accuracy of the results decreases slightly as the given orders become less precise. For the given example, method 3 returns the smallest

Table 3.3: Simulation studies: algorithms (averaged RMSE over 10000 runs and variance of the RMSE for G_{ref} and G_{noise} with $\sigma = 0.001$, $q = 0.5$, $n = 1$ and $m = 0$).

Method	Mean RMSE with G_{spec} $\times 10^{-4}$	Variance RMSE with G_{spec} $\times 10^{-8}$	Mean RMSE with G_{noise} $\times 10^{-4}$	Variance RMSE with G_{noise} $\times 10^{-8}$
1	3.7326	3.9322	10.2942	2.5483
2	2.3283	1.4941	9.7477	1.9882
3	2.1990	1.3706	9.6404	1.9425
4	5.0580	14.2000	11.2319	5.6183
5	3.8884	7.0998	10.4396	3.0687

RMSE for both cases, but is also the slowest algorithm. The fact that method 3 gives the best results is often seen in other specifications or examples, e.g. in the tables in the appendix. Method 4 has the worst RMSEs, although the parameter vector is very close to the given one.

At a higher noise level, this rather clear ranking of the algorithms is no longer so obvious. This means that for real measurements where the noise can be very different any algorithm might be useful. However, it can be assumed that method 3 will find a reliable solution in most cases.

In addition, the dependency of the RMSE on the noise level σ and the commensurate order q is investigated. The noise level is varied from $\sigma = 0.0001$ on to $\sigma = 0.001$ in steps of 0.0001 and for q values from 0 to 1 are given in steps of 0.01. Method 5 is used exemplary in this case. The results are shown in Figure 3.2.

The influence of the noise level is as expected. The smoothness of the resulting error decreases with increasing noise. However, in the direction of the variable commensurate order q the function has a very irregular curve. In the range between $q = 0.2$ and $q = 0.3$ there is an enormous increase of the RMSE. A similar behavior is observed using the other methods. This could be particularly problematic in the case of an optimization. The error in q is a non-convex function and hence it is not guaranteed that an algorithm like steepest descent is able to find the global minimum. The minimum for small noise is clearly $q = 0.5$, which is the correct q.
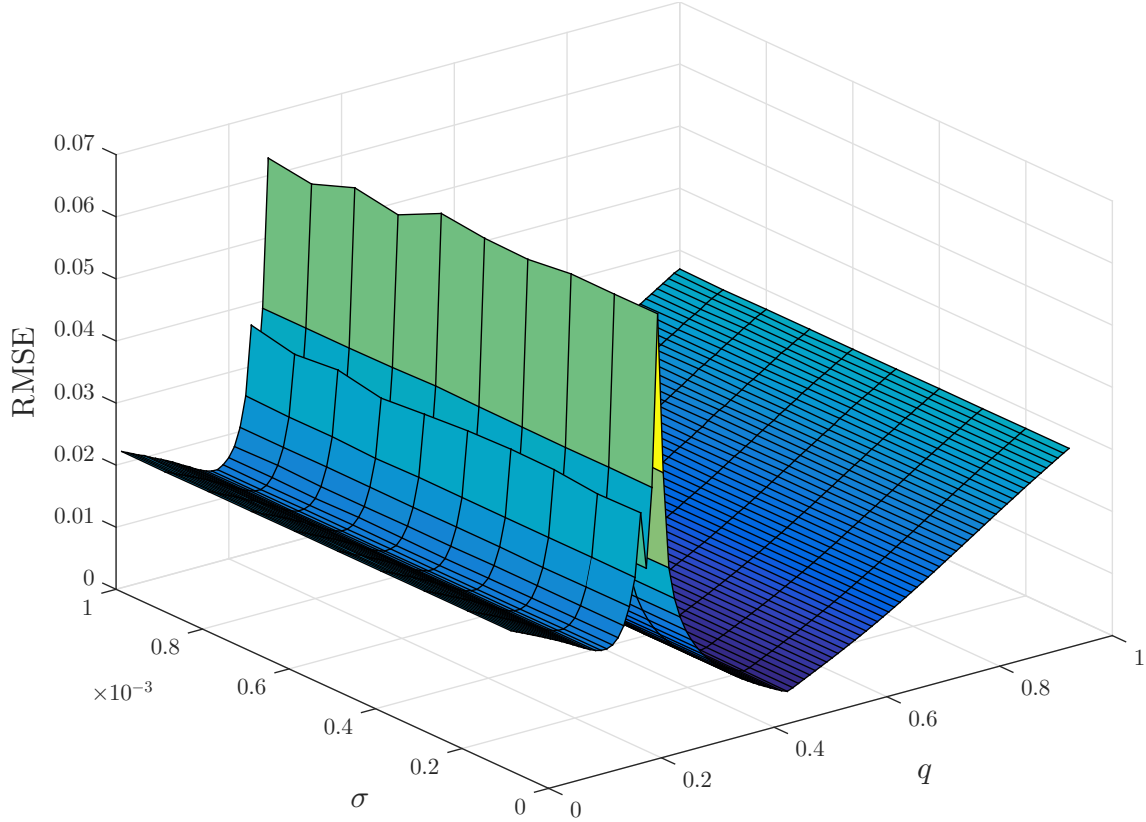
Figure 3.2: RMSE with G_{noise} for different noise levels and commensurate orders q calculated with method 5.

3.4.2 Optimization

Following the just explained problem of the strong variance of the RMSE in dependence of q, the optimization presented in Section 3.3 will now be examined.

The same conditions are used as in the previous section. That means G_{spec} is defined as in (3.24). The same orders n and m are also given. The commensurate order q is optimized this time. Also $\sigma = 0.001$ is selected again for the generation of the noise data. However, the calculation is only performed 1000 times for different noise vectors, because the optimization is much slower. The influence of different initial values on the result of the optimization is examined. Therefore two stable initial estimates of the parameter vector $x_0^\top = \begin{bmatrix} 0.5 & 0.5 & \dots & 0.5 & 0.1 \end{bmatrix}$ and $x_0^\top = \begin{bmatrix} 0.5 & 0.5 & \dots & 0.5 & 1 \end{bmatrix}$ as well as two unstable initial estimates of the parameter vector $x_0^\top = \begin{bmatrix} -0.5 & 0.5 & \dots & 0.5 & 0.1 \end{bmatrix}$ and $x_0^\top = \begin{bmatrix} -0.5 & 0.5 & \dots & 0.5 & 1 \end{bmatrix}$ are examined where $x_0 \in \mathbb{R}^3$, $x_0 \in \mathbb{R}^4$ and $x_0 \in \mathbb{R}^6$ (for the three different combinations of the orders n and m discussed in Section 3.4.1).

Table 3.4 shows the results for $n = 1$ and $m = 0$. Here the optimization gives the same result for all specified initial vectors, so only one column is listed. The other results are given in Table 3.5 and in Tables A.5 and A.6 in the appendix.

Table 3.4: Simulation studies: optimization (1000 runs, $\sigma = 0.001$, $n = 1$ and $m = 0$).

$\overline{a}$	$\begin{bmatrix} 1 & 0.9997 \end{bmatrix}$
$\mathrm{Var}(a)$	$\begin{bmatrix} 0 & 1.7678 \end{bmatrix} \times 10^{-4}$
$\overline{b}$	$\begin{bmatrix} 0.9998 \end{bmatrix}$
$\mathrm{Var}(b)$	$\begin{bmatrix} 0.7195 \end{bmatrix} \times 10^{-4}$
$\overline{q}$	0.5001
$\mathrm{Var}(q)$	7.1897×10^{-6}
Mean RMSE with G_{spec}	2.3346×10^{-4}
Variance RMSE with G_{spec}	1.3059×10^{-8}
Mean RMSE with G_{noise}	9.5296×10^{-4}
Variance RMSE with G_{noise}	1.8946×10^{-8}

For the correct orders, the optimization still delivers the correct coefficients and the correct q with an error that is within the range of the RMSEs of the algorithms. For higher orders, however, it quickly becomes clear that the nonlinear optimization runs into local minima due to the non-convex and nonlinear structure of the optimization problem and the specification of different initial values. This results in the necessity of a global optimization in order to find the parameter set with the best fit. However, global optimization procedures are generally much more computationally time-consuming, which makes it difficult to use this class of estimators for online parameter identification.

The results of the global optimization using `MultiStart` in MATLAB which attempts to find multiple local solutions by starting from various initial points can be found in Table A.7. The given initial values are $x_0^\top = \begin{bmatrix} -0.5 & 0.5 & 1 \end{bmatrix}$, $x_0^\top = \begin{bmatrix} -0.5 & 0.5 & 0.5 & 1 \end{bmatrix}$ and $x_0^\top = \begin{bmatrix} -0.5 & 0.5 & 0.5 & 0.5 & 0.5 & 1 \end{bmatrix}$ which are the vectors that lead to the worst results of the nonlinear optimization discussed earlier.

Here, only 100 different runs (with variable noise vector) could be performed, due to the already mentioned slow computation speed of the global optimization.

The results are significantly better compared to the previous optimization. In the case $n = 2$ and $m = 2$, the identified model parameters are not well approximated compared to the given model (the variances of some values are also very high), but the RMSE is in a similar range. This could not be claimed before. Moreover, the commensurate order is also well identified. In terms of the noisy data G_{noise}, the global optimization fits better than the algorithms from Section 3.2, but for the correct model G_{spec}, the RMSEs obtained by methods 2 and 3 are smaller.

Thus, global optimization can also be used to estimate the model parameters with real measurement data.

Table 3.5: Simulation studies: optimization (1000 runs, $\sigma = 0.001$, $n = 1$ and $m = 1$).

$x_0^\top$	$\begin{bmatrix} 0.5 & 0.5 & 0.5 & 0.1 \end{bmatrix}$	$\begin{bmatrix} -0.5 & 0.5 & 0.5 & 0.1 \end{bmatrix}$	$\begin{bmatrix} 0.5 & 0.5 & 0.5 & 1 \end{bmatrix}$	$\begin{bmatrix} -0.5 & 0.5 & 0.5 & 1 \end{bmatrix}$
$\overline{a}$	$\begin{bmatrix} 1 & 1.0000 \end{bmatrix}$	$\begin{bmatrix} 1 & 55.1232 \end{bmatrix}$	$\begin{bmatrix} 1 & 7.8037 \end{bmatrix}$	$\begin{bmatrix} 1 & -27.3086 \end{bmatrix}$
$\mathrm{Var}(a)$	$\begin{bmatrix} 0 & 3.2297 \end{bmatrix} \times 10^{-4}$	$\begin{bmatrix} 0 & 1.3321 \end{bmatrix} \times 10^{3}$	$\begin{bmatrix} 0 & 0.1390 \end{bmatrix}$	$\begin{bmatrix} 0 & 24.4183 \end{bmatrix}$
$\overline{b}$	$\begin{bmatrix} 1.0001 & -0.0001 \end{bmatrix}$	$\begin{bmatrix} 5.0765 & 11.3428 \end{bmatrix}$	$\begin{bmatrix} -0.5638 & 2.7296 \end{bmatrix}$	$\begin{bmatrix} 45.4255 & -51.8932 \end{bmatrix}$
$\mathrm{Var}(b)$	$\begin{bmatrix} 1.2730 & 0.0916 \end{bmatrix} \times 10^{-4}$	$\begin{bmatrix} 0.8115 & 0.7630 \end{bmatrix} \times 10^{3}$	$\begin{bmatrix} 0.0076 & 0.0225 \end{bmatrix}$	$\begin{bmatrix} 59.0852 & 71.0984 \end{bmatrix}$
$\overline{q}$	0.5000	0.1412	0.0015	2.4631×10^{-18}
$\mathrm{Var}(q)$	4.5006×10^{-5}	4.1600×10^{-2}	7.2294×10^{-4}	1.9269×10^{-36}
Mean RMSE with G_{spec} $\times 10^{-4}$	2.7394	285.4958	451.2613	452.5969
Variance RMSE with G_{spec}	1.6532×10^{-8}	4.3132×10^{-4}	5.9328×10^{-6}	4.7141×10^{-13}
Mean RMSE with G_{noise} $\times 10^{-4}$	9.4024	287.2987	451.3501	452.6771
Variance RMSE with G_{noise}	1.9008×10^{-8}	4.2213×10^{-4}	5.9051×10^{-6}	7.7617×10^{-9}

4 Experiment

The last chapter is dedicated to practical experiments. First, the two experimental setups are described, and then the measurement procedure is discussed.

This is followed by the evaluation of the measured data and the application of the algorithms and methods for fitting fractional-order transfer functions explained in Chapter 3. The results are discussed and validated.

4.1 Experimental Setup

The investigated hydraulic system is almost completely described in [26]. It consists of two single rod, double-acting cylinders connected with a linear force sensor that is measuring the respective load from the perspective of each cylinder. The actuator of this system is a servo valve, the dashpots can be moved by controlling the valve opening. According to [26] the valve has a ten percent overlap in the spool-orifice area, i.e. there is a dead zone. The complete experimental setup is shown in Figure 4.1.

The first part of the experiments deals with the dashpot on the right side. It is disconnected from the force sensor and the left dashpot. This means that it can move freely within its maximum extension length.
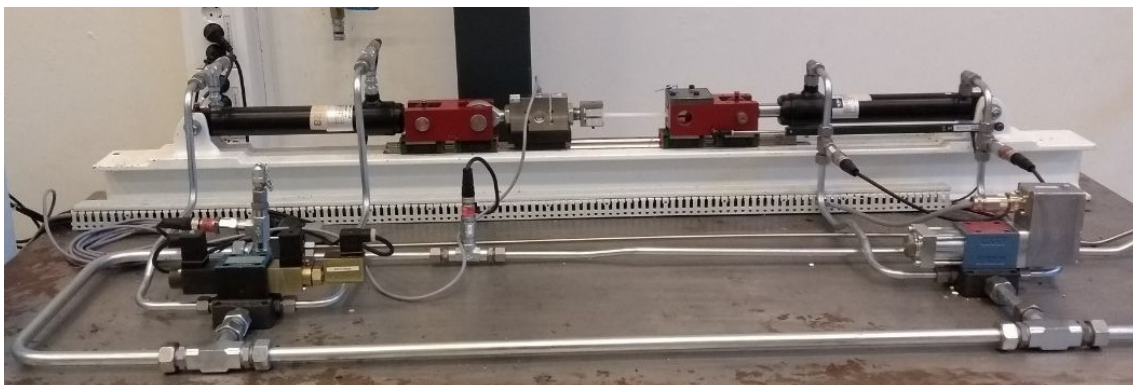

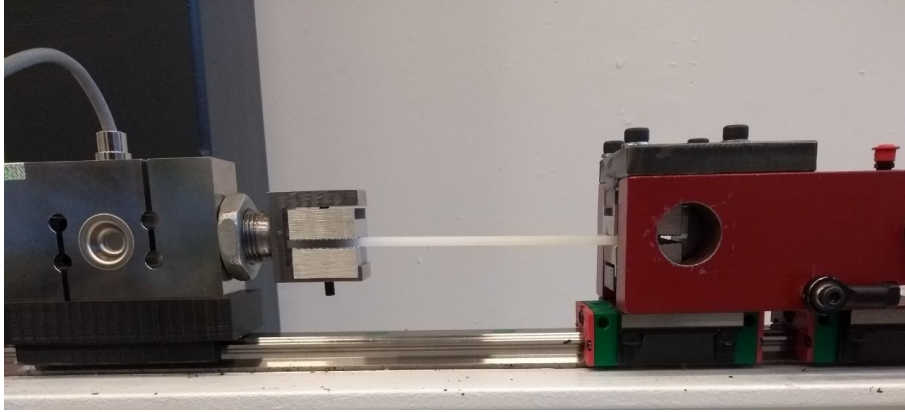Figure 4.1: Experimental hydraulic setup (laboratory view).

Figure 4.2: New parts of experimental hydraulic setup (laboratory view).

The hydraulic system was adjusted for the implementation of tensile tests. The modified section of the setup is shown in more detail in Figure 4.2. There are modifications that are used as a mount for polymer samples. One side of the mounting bracket is connected to the force sensor and the other side to the cylinder on the right. During the experiments, the left cylinder is held in the retracted position and only the right cylinder can move. This can then be driven manually to the desired position in order to fix the sample. The position measurement by the linear potentiometer has been extended by a laser sensor, which measures the distance from the cylinder to the bracket on the force sensor.

Furthermore, the samples have been tested on a servo-hydraulic testing machine for dynamic loads to validate the measurement results. The material testing machine HB100 was produced by ZwickRoell GmbH & Co. KG [38]. The schematic structure of this machine is depicted in Figure 4.3. The test cylinder, which is installed in the upper load frame, can apply forces of up to 25 kN [38]. Using the software Workshop 96, the position can be controlled sinusoidally [28]. The measurement data acquisition required for dynamic testing is also implemented via the software. A maximum of 10000 points can be recorded per measurement variable and measurement process [28].

4.2 Measurement Procedure

The aim of the investigations is to determine the transfer behavior of the dashpot and various polymer samples. According to the principle described in Section 3.1 they are excited with sinusoidal signals of different frequencies. In the following, the measurement procedures of the experiments are explained.
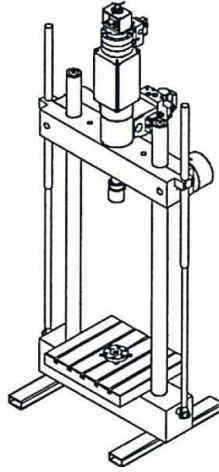
Figure 4.3: Servo-hydraulic testing machine (schematic view) [38].

Polymer Samples

In the force-controlled (FC) case, the right cylinder is moved to the initial position, where the sample is fixed with the mounting brackets. The sample is prestressed to $-200\,\text{N}$ in order to avoid compressive stress which might lead to buckling. The force is then controlled sinusoidally. The control principle is presented in [25]. Finally, the cylinder returns to the initial level of $0\,\text{N}$. Following a measurement, the sample must be dissolved directly, which leads to variable initial conditions of each measurement. However, this process is necessary to protect the samples from excessive loads.

The input-output plot is shown in Figure 4.4 for a single frequency. A hysteresis and creep effect is clearly visible. Therefore, the fractional-order modeling approach seems reasonable. The force-controlled measurement, however, leads to drifting off the sample. It is not returned to its initial position and remains stretched. This results in the drift, which can be observed in the position over time.

The measurements were carried out on three samples, two made of polypropylene (PP) and one made of polybutylene terephthalate (PBT). The specified sine was measured for frequencies from $0.05\,\frac{\text{rad}}{\text{s}}$ to $10\,\frac{\text{rad}}{\text{s}}$ in a logarithmic scale, alternately ascending and descending. Eight measurement series were recorded per sample.

For the validation with the position-controlled (PC) setup, only one measurement was recorded per sample and frequency. Less frequencies were considered in the range of $0.01\,\text{Hz}$ to $30\,\text{Hz}$. The stress-strain diagrams of some measurements are depicted in Figure 4.5. Due to the position-controlled approach the loops are closed, and a frequency dependent input-output lagging can be observed.
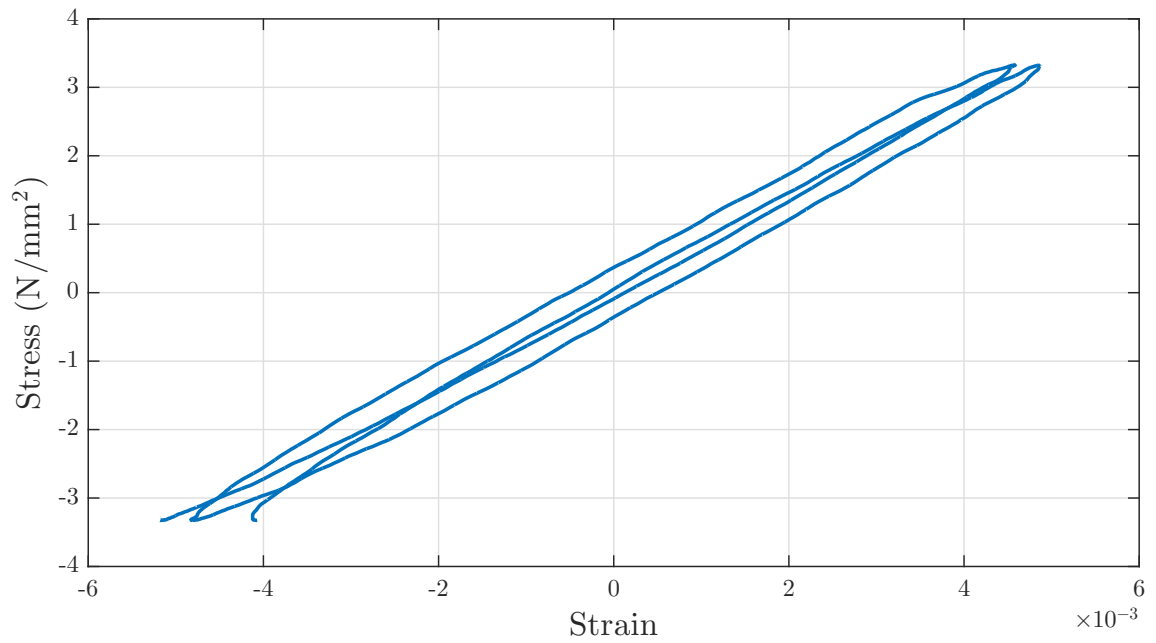
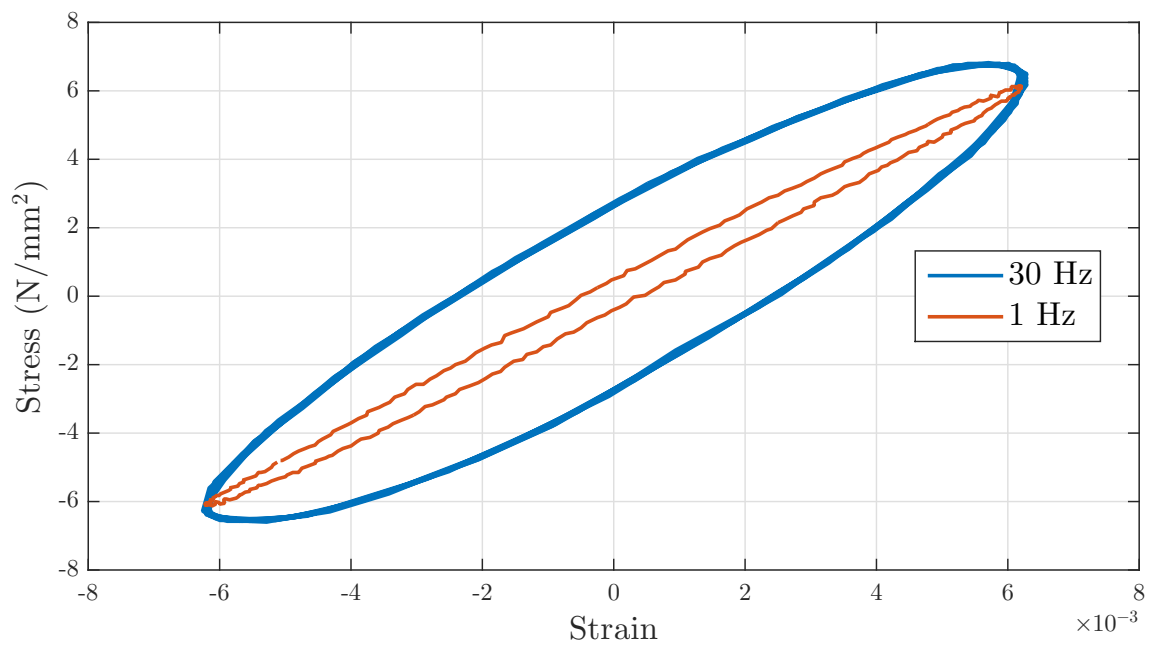Figure 4.4: Stress-strain diagram (force-controlled setup).

Figure 4.5: Stress-strain diagram (position-controlled setup).

Dashpot

In addition to the polymer samples, the transfer behavior of the dashpot is also investigated in the first experimental setup. Here, the right cylinder is disconnected from the left cylinder and is then freely movable within its maximum extension length. Two different modes are examined. First, the dashpot is operated in open-loop without a controller, i.e. the valve is directly excited sinusoidally. It is then moved in closed-loop mode with the position control described in [25].

In the open-loop case, frequencies from $0.03 \frac{\text{rad}}{\text{s}}$ to $10 \frac{\text{rad}}{\text{s}}$ are considered. The position of the cylinder arm is subject to a linear trend, as the arm extends faster than it retracts. The amplitude of the sinusoidal oscillation therefore has to be very low, otherwise the maximum extension length will be reached for small frequencies. It is set to a 10% valve opening. However, this leads to the fact that for high frequencies there is hardly any movement of the cylinder recognizable.

For the closed-loop case, these problems do not matter. Here the cylinder is first moved to half its maximum extension length and then oscillates by $2\,\text{cm}$ with frequencies from $0.05 \frac{\text{rad}}{\text{s}}$ to $10 \frac{\text{rad}}{\text{s}}$.

In both cases, ten measurement series were recorded per frequency.

Additional to these measurements, a Simulink model introduced by Pasolli and Ruderman [25] is used to compare the results.

4.3 Results

This section includes the preprocessing of the measured data as well as the results of the tests with the polymer samples and the dashpot.

4.3.1 Preprocessing

The collected raw data must be prepared before they can be used to determine the transfer behavior. This preprocessing is explained in this section.

For the dashpot experiments, the following information is stored: the position of the right cylinder x_d and the two pressures at both ends inside the cylinder p_3 and p_4. According to Section 2.5, the equilibrium of forces inside the cylinder can be described with (2.18). In this case, the dashpot is disconnected from the left cylinder. Therefore, no external forces have an influence. That means, the load force F_l is set to zero. Friction is also neglected ($F_\text{f} \approx 0$). This simplifies the

equation for the resulting force in the dashpot to

$$F_{\mathrm{d}} = A_4 p_4 - A_3 p_3, \tag{4.1}$$

where $A_4 = 0.0013\,\mathrm{m}^2$ and $A_3 = 0.00076\,\mathrm{m}^2$ are the cross-sectional areas of the respective ends of the cylinder [26]. The mean values are calculated from the ten measurement series. The non-sinusoidal parts of the averaged signals have to be cut off and integer periods have to be selected because otherwise the results would be affected. Finally, linear trends and offsets are eliminated, too.

For the polymer sample tests, the position of the dashpot x_{d} (measured with two different sensors) and the force F measured with the force sensor are stored. First, all measured data are averaged over the eight measurement series. The ramps at the beginning and at the end, which are used for prestressing the samples, must be cut off. Again, integer periods must be selected and the offsets have to be removed. Since, as written in Section 2.4, the viscoelastic behavior of the samples is of interest, the force and position signals were converted into stress and strain, i.e.

$$\sigma(t) = \frac{F(t)}{A_0},$$
$$\epsilon(t) = \frac{\Delta l(t)}{l_0},$$

where $\Delta l(t) = x_{\mathrm{d}}(t) - l_0$. Based on the dimensions of the samples, $A_0 = 40\,\mathrm{mm}^2$ and $l_0 = 80\,\mathrm{mm}$ are fixed. Only the middle uniform part of the sample was selected to measure the size. The outer wider areas have been neglected. In addition, repeated measurements may result in permanent changes in length and diameter. As known from (2.7), Young's modulus E can be calculated as follows:

$$E = \frac{\sigma}{\epsilon} = \frac{l_0 F}{A_0 \Delta l}.$$

The unit of E is then $\dfrac{\mathrm{N}}{\mathrm{mm}^2} = \mathrm{MPa}$. The calculated E from the measurements with the PP samples are in the range of 0.5 to 1.2 GPa. This is slightly below the values from 0.7 to 1.5 GPa given in [15]. This deviation can have various causes, starting with the difficult calculation of the values with the very noisy measurement data. In contrast, the calculated values for the PBT samples lie in a wider range from 2 to 3.5 GPa compared to the values of 2.5 to 2.8 GPa given in [3]. The causes will be similar.

Figure 4.6: Behavior of semicrystalline thermoplastics at rising temperature [36].

4.3.2 Polymer Samples

Polymers show a viscoelastic behavior in a limited temperature range. This can be seen in Figure 4.6, where T_g is the glass-transition temperature, T_m is the melting temperature and T_d is the decomposition temperature. In the vicinity of T_g, which is specific to each polymer, the behavior changes from hard and relatively brittle to viscous or rubbery [36]. This can also be explained by the spring-damper analogy introduced in Section 2.4. For temperatures below the glass-transition temperature the dampers can be regarded as "frozen" [36]. This makes the material largely elastic. The dampers only work above T_g and the higher the temperature, the easier the dampers "run" [36].

The glass-transition temperature T_g of PP is $10\,°C$ and of PBT $60\,°C$ [36]. This means that at a normal room temperature of $20\,°C$ the PP samples should show a viscoelastic behavior during the experiments and the PBT samples should still be in the elastic range. It was at least evident that the PBT samples were significantly harder and did not expand as much as the others under the same force. Whether they have returned to their original length after a tensile test cannot be determined exactly.

Polymers can show four possible behaviors in tensile tests which are depicted simplistic in Figure 4.7 [36]:

1. Brittle: After elastic deformation, fracture occurs.
2. Brittle, hornlike: After exceeding a maximum tension, breakage occurs without significant necking (the process by which a ductile material deforms under tension forming a thin neck).
3. Viscoelastic: After exceeding the yield stress (first maximum) the sample constricts spontaneously by a certain amount. In the further course of time, this necking area is extended without a further reduction in cross-section. This extension can reach a very large length. The total elongation may exceed 500%.
4. Rubber elastic: The deformation takes place largely without Hooke's area. Provided that the material has not been stressed to breakage, the deformation largely returns after relief.
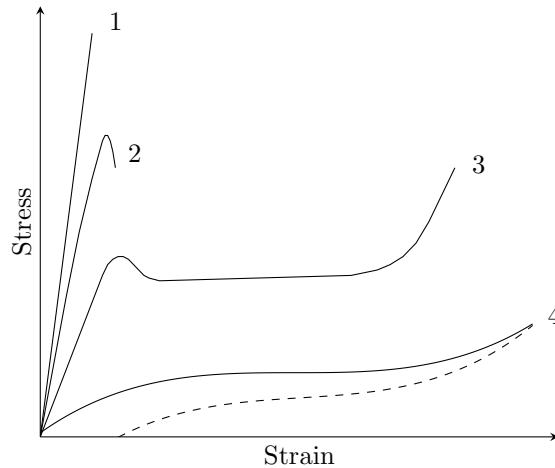
Figure 4.7: Behavior of polymers in tensile tests (1 and 2 brittle, 3 viscoelastic, 4 rubber elastic) [36].

Figure 4.8: Result of tensile test with PP samples under high force (above sample for comparison).

A material can show the behaviors 1 to 3 depending on the load temperature [36]. This is also visible from the PP samples. Two of the white samples were initially stressed with a high force. The result is shown in Figure 4.8. The samples appear to exhibit behavior 3, as they were stretched for a long time before they broke, or the dashpot reached its minimum insertion length.

Following this preliminary examination of the samples, the results of the actual investigations are now presented. Figure 4.9 shows the resulting Bode diagrams for the three different samples obtained by applying the procedure described in Section 3.1. For the measurement results recorded with the force-controlled setup, the largest deviations from the mean value are also displayed with error bars. With the other experimental setup, less data is recorded, but over a larger frequency range. The error cannot be specified here because the measurements were not repeated. They were subject to significantly lower noise compared to the other data. However,
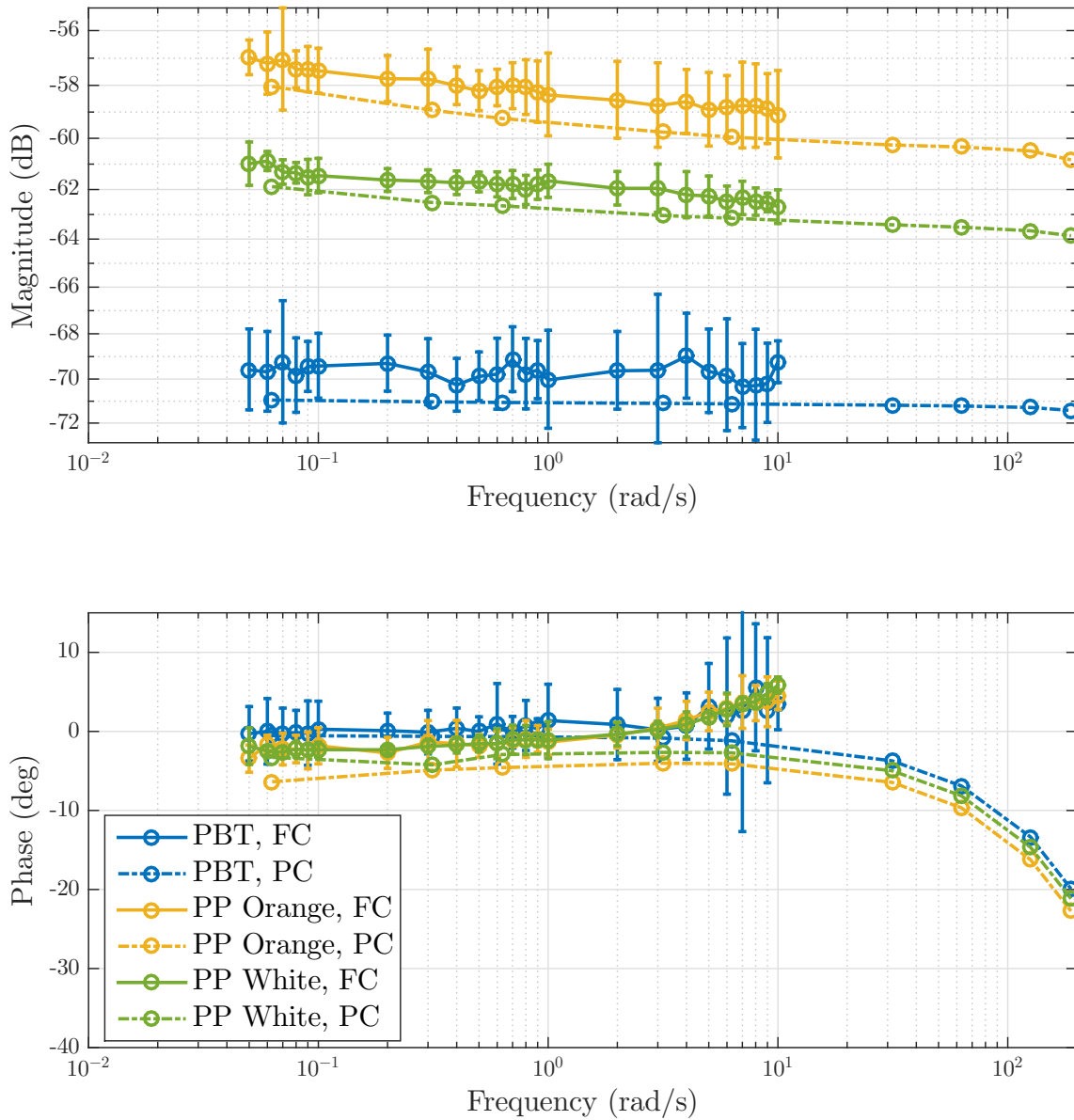
Figure 4.9: Bode diagram with the amplitude and phase responses of the three different samples for the force-controlled (FC) setup with error bars and for the position-controlled (PC) setup.

the accuracy of the position-controlled experiments was $1 \cdot 10^{-5}$ m for the position and 1 N for the force. These data points are near or between the error ranges of the force-controlled measurements. The white sample shows the greatest deviation, as the error bars are much smaller here. This indicates that the position-controlled test setup also gives similar curves, at least for the lower frequencies. The force-controlled test setup was poorly suited for higher frequencies, which is particularly noticeable in the phase response. The signals are very noisy, therefore the evaluation of the FFT can be inaccurate at this point. At least the data obtained with the two different methods have the same scale and a slight decrease in their amplitude. In a first approximation, this can be considered constant, which indicates the behavior of a spring. The phase response could be caused by a delay. In general, the force-controlled data are significantly worse despite the higher number of measurements.

In the following, only the results of one sample will be presented, as the results of the other samples do not differ significantly. The orange PP sample is chosen, since validation data for the time domain have also been recorded for this.

In Section 2.4.2 some well-known fractional-order models for viscoelastic behavior were presented. Some of these model structures will now be used as a basis for fitting the fractional-order transfer function. Starting with a very simple model, the fractional Voigt model shall be examined, because the generalized Maxwell model does not fit optimally to the required structure of the transfer function (3.1). One parameter more must be found for the second model, the generalized Zener model. And to investigate the influence of a higher order, the maximum orders $n_{\max}$ and $m_{\max}$ for the third approach $G_{\max 3}$ are set to 3. Maximum order means in this case that the orders are not fixed, but that there is a loop over the orders $n = 1, \ldots, n_{\max}$ and $m = 0, \ldots, n$ and finally the stable model with the lowest RMSE is selected. This means that the structures of the transfer functions to be fit are as follows:

$$G_{\mathrm{Voigt}} = \frac{b_0}{a_1 s^q + 1},$$
$$G_{\mathrm{Zener}} = \frac{b_1 s^q + b_0}{a_1 s^q + 1},$$
$$G_{\mathrm{max3}} = \frac{b_{m_i} s^{m_i q} + \ldots + b_0}{a_{n_i} s^{n_i q} + \ldots + 1}, \quad n_i = 1, \ldots, 3, \quad m_i = 0, \ldots, n_i.$$

In order to determine the coefficients of these models and the commensurate order q such that they fit the measured data optimally, the methods tested in Section 3.4.1 and the global optimization discussed in Section 3.4.2 with 1000 different initial points are used. When applying methods 1 to 5 the commensurate order q is varied

in 0.01-steps from 0 to 1 to find the parameter vector that gives the smallest RMSE. In addition, using the global optimization with $q = 1$ fixed models of integer order with the same structure are fitted. In case of the position-controlled setup, not all measured data points are fitted. As no validation data are available, two data points are removed to be able to use them for a later validation.

Figures 4.10 and 4.11 show exemplary the results for the position-controlled setup with G_{Voigt} and G_{max3}, respectively.
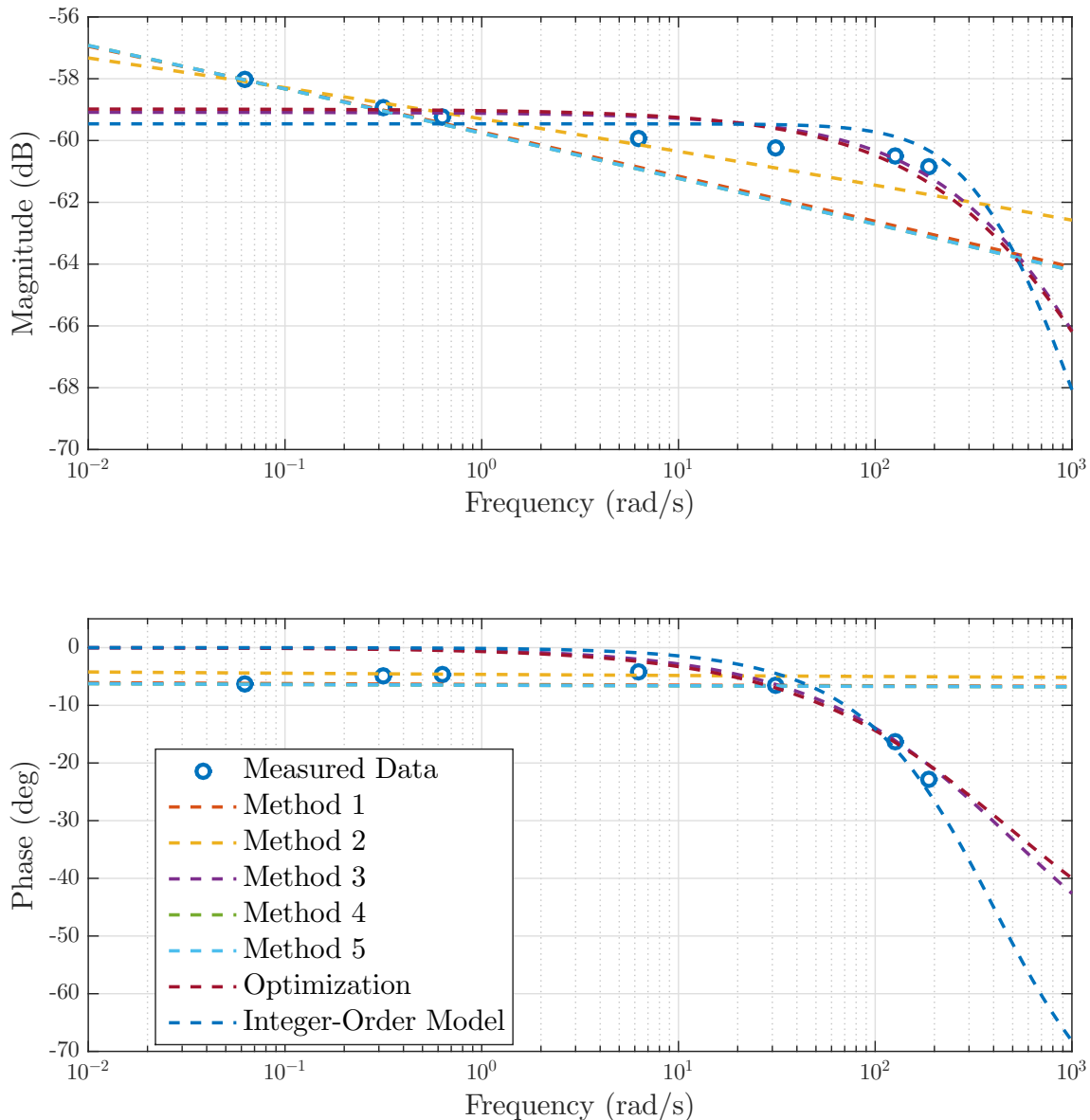
Figure 4.10: Best fit of the transfer behavior of PP for G_{Voigt} (orange sample, position-controlled setup).

Further graphics for the orange sample can be found in the Appendix A.3. No stable transfer function is found for the Zener approach using method 3, therefore this result is not shown.

The graphs show that a significantly better fit is achieved with a higher model order. Furthermore, it can be assumed that some better fitting results are thrown away due to the subsequent check for stability when using the algorithms. Therefore, it is obvious that the approximations of the global optimization are closest to the measured data. This is also illustrated by the calculated RMSEs in Table 4.1. Also, the low parameterized models of integer order do not reach the accuracy of the
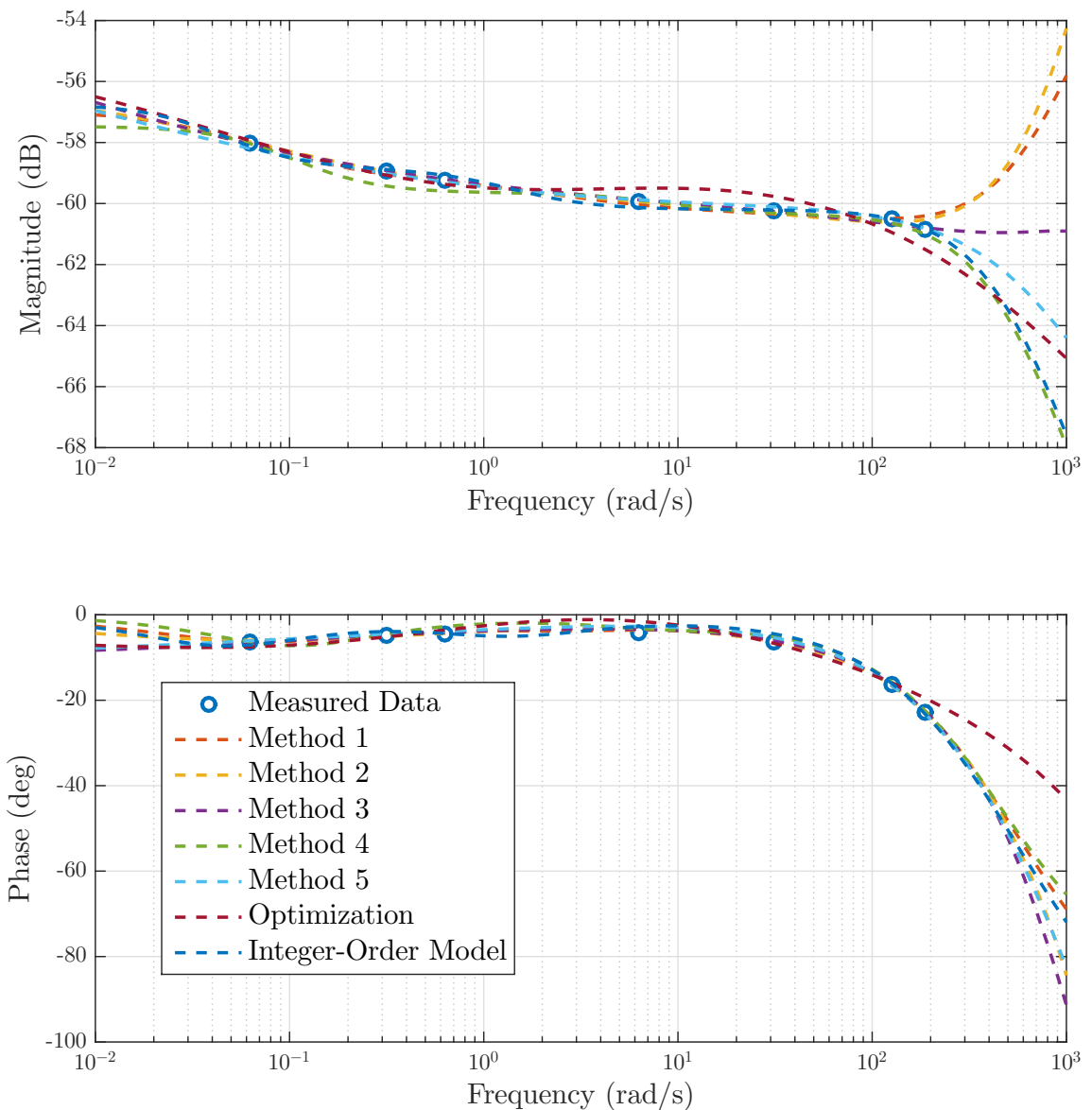
Figure 4.11: Best fit of the transfer behavior of PP for G_{max3} (orange sample, position-controlled setup).

optimized models, which was to be expected, because they have one free parameter less. For G_{max3} the integer-order models do fit better than the optimized models. This may be because they cover a smaller search space with the same number of different initial values, which increases the possibility of determining a favourable initial value. By choosing the solution of the integer-order optimization as starting value for a local optimization of the fractional-order models with the SQP method, an RMSE is obtained which is slightly better than that received with the integer-order optimization. The RMSEs of the PC setup models are usually higher because there are significantly fewer measurement points.

Table 4.1: Identification results orange PP samples: RMSE $\times 10^{-5}$.

| | G_{Voigt} | | G_{Zener} | | G_{max3} | |
Method	FC	PC	FC	PC	FC	PC
1	1.8121	6.3798	1.2878	5.9041	1.2878	0.7925
2	1.7112	5.1369	1.7696	5.8411	0.9446	0.5851
3	1.8082	3.8015		3.4448	1.1729	0.4032
4	1.8836	6.5335	1.4978	5.8096	1.4793	1.3218
5	1.8843	6.5332	1.4672	8.9906	0.9736	0.6858
Opt	1.5276	3.7678	1.1989	3.2842	0.7048	1.9875
Int	2.1221	4.4910	1.2002	4.1969	0.6186	0.8353

Further interesting information are the coefficients $a = [a_0, \ldots, a_n]$ and $b = [b_0, \ldots, b_m]$ and the commensurate order q of the approximated models. These are shown exemplary for G_{Voigt} in Table 4.2. The other tables can be found in Appendix A.2.

For given small orders the obtained commensurate orders are very similar in case of the force-controlled setup. The RMSEs show that for the position-controlled setup the global optimization and method 3 clearly provide the best results, since their orders q are very similar but fundamentally different from the ones provided by the other algorithms. This shows that despite the specification of the same orders, the obtained FOTFs can differ enormously.

A similar behavior can be seen in Table A.8 for the Zener approach. Here the commensurate orders for the FC setup are for the most part relatively close to each other, while for the PC setup, q varies more. This could be since the significantly fewer measuring data offer more freedom in the search for the optimal parameters.

Table 4.2: Identification results orange PP samples for G_{Voigt}: coefficients and commensurate order.

Method		FC	PC
	a	$\begin{bmatrix} 1 & 0.4262 \end{bmatrix}$,	$\begin{bmatrix} 1 & 7.7929 \end{bmatrix}$,
1	b_0	0.0018,	0.0091,
	q	0.1	0.08
	a	$\begin{bmatrix} 1 & 0.5126 \end{bmatrix}$,	$\begin{bmatrix} 1 & 2.7926 \end{bmatrix}$,
2	b_0	0.0019,	0.0041,
	q	0.08	0.07
	a	$\begin{bmatrix} 1 & 5.2621 \end{bmatrix}$,	$\begin{bmatrix} 1 & 0.0100 \end{bmatrix}$,
3	b_0	0.0077,	0.0011,
	q	0.05	0.74
	a	$\begin{bmatrix} 1 & 3.5708 \end{bmatrix}$,	$\begin{bmatrix} 1 & 9.4960 \end{bmatrix}$,
4	b_0	0.0058,	0.0108,
	q	0.05	0.08
	a	$\begin{bmatrix} 1 & 3.5434 \end{bmatrix}$,	$\begin{bmatrix} 1 & 9.4923 \end{bmatrix}$,
5	b_0	0.0057,	0.0108,
	q	0.05	0.08
	a	$\begin{bmatrix} 1 & 2.9028 \end{bmatrix}$,	$\begin{bmatrix} 1 & 0.0133 \end{bmatrix}$,
Opt	b_0	0.0048,	0.0011,
	q	0.0357	0.6980
Int	a	$\begin{bmatrix} 1 & 0.0000 \end{bmatrix}$,	$\begin{bmatrix} 1 & 0.0025 \end{bmatrix}$,
	b_0	0.0012	0.0011

A significantly higher variation of the commensurate order is shown for G_{max3} in Table A.9, where it can be seen that very different parameter combinations lead to a similar error, indicating overfitting. There is also a big difference between the FC setup and PC setup fits, although both describe the same plastic. However, since the plotted transfer behavior also shows differences, this problem can be attributed to it. It is difficult to make generalized statements in this case. On average the PC setup models have a higher model order.

These investigations confirm that fractional-order transfer functions represent the assumed viscoelastic behavior of the orange samples more accurately than integer-

order transfer functions of the same order. During optimization, however, it is never quite certain that the global optimum has really been found. This is also not easy to verify. The methods 1 to 5 would also give better results if the unstable transfer functions are not subsequently removed. Thus, the potential of these algorithms cannot be fully exploited. For low model orders, similarities can be found in the optimized FOTF, but with increasing model order the obtained transfer functions and their commensurate orders q show little in common. Especially the latter vary enormously. In this case, it is therefore difficult to make a choice as to which of the FOTFs represents the behavior best. What can be done, however, is to look at the curves of the transfer functions in the Bode diagrams outside the measured range and examine them for their physical usefulness. For example, in Figure 4.11 the amplitudes of the transfer functions obtained using methods 1 and 2 increase at $100\,\frac{\text{rad}}{\text{s}}$. This behavior cannot be explained physically, so these two FOTF should not be considered further.

4.3.3 Model Validation

The transfer function models found in the previous section will now be validated. It can be expected that the models fit well if the error between the validation data and the fitted models corresponds approximately to the RMSEs that resulted from the identification process.

For the FC setup a chirp signal was recorded and for the PC setup two data points of the transfer behavior were removed before the identification procedure, because it was not possible to generate a chirp signal in this experimental setup. This data is now used for the validation. The magnitude and phase calculation described in Section 3.1 can also be applied to obtain the transfer behavior of the orange PP sample. This time, however, the FFT is not evaluated at a single frequency, but at all frequencies contained in the chirp signal. The resulting bode diagram can be seen in Figure 4.12 in comparison to the behavior already shown.

Again the RMSE is calculated as in (3.23), where $G_{\text{ref}}(\omega) = Y_{\text{chirp}}/U_{\text{chirp}}$, $\omega \in [0.4641\,\frac{\text{rad}}{\text{s}}, 5.9619\,\frac{\text{rad}}{\text{s}}]$, in case of the FC setup and $G_{\text{ref}}(\omega) = Y_{\text{2of9}}/U_{\text{2of9}}$, $\omega \in \{0.5\,\text{Hz}, 10\,\text{Hz}\}$ in case of the PC setup. The results can be found in Table 4.3.

In general, the RMSEs have a similar magnitude as the RMSEs in Table 4.1. Most error values for the FC setup have become smaller, but for the PC setup all but one value have become larger. This is also visible in Table A.10 where the ratios of the RMSEs of the validation and the RMSEs of the fitting data are shown. Additionally, there is a big change in the methods that show the best and
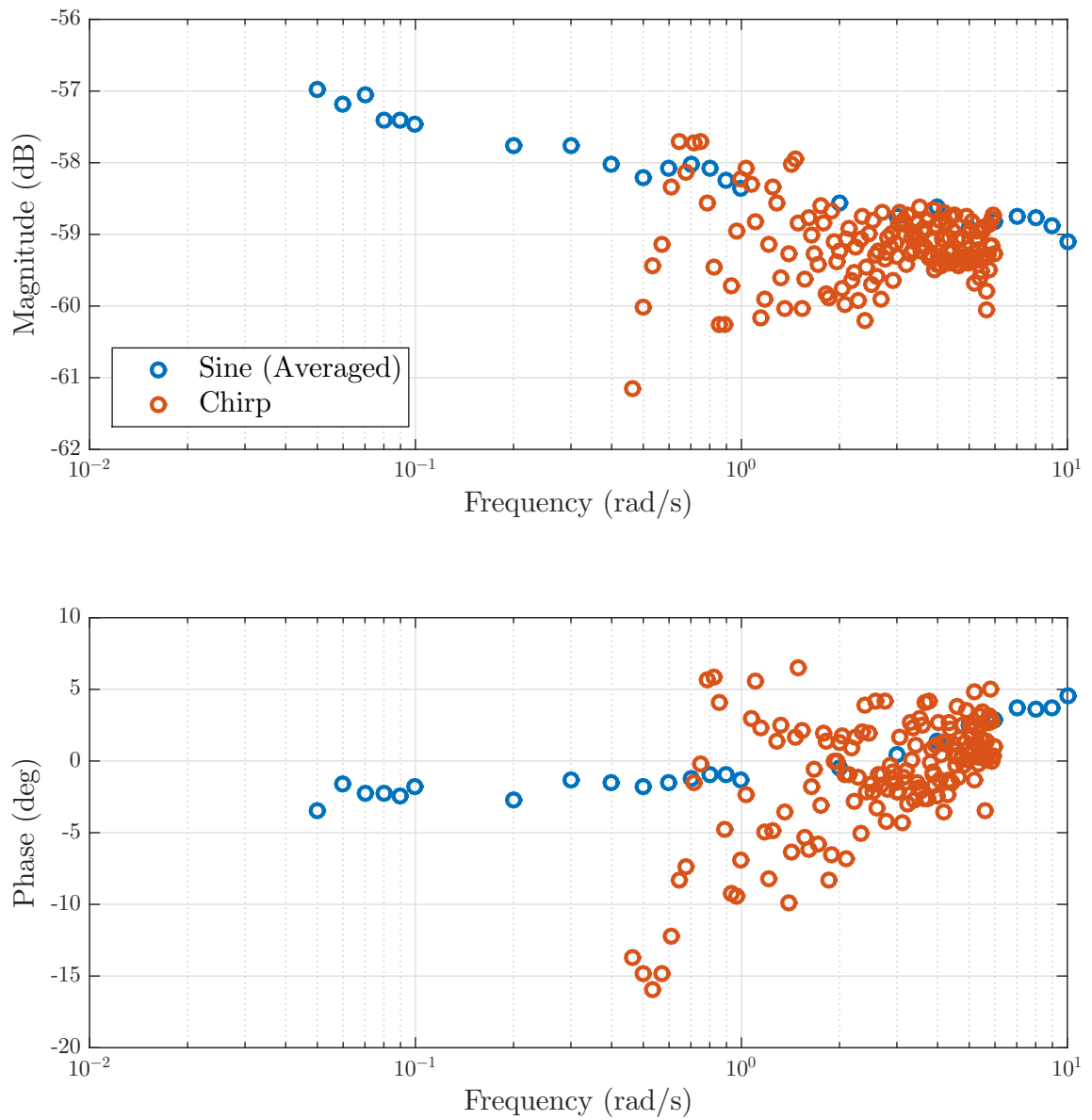
Figure 4.12: Bode diagram with the amplitude and phase responses of the orange PP sample for the FC setup obtained by using averaged sine waves of different frequencies and a chirp signal.

Table 4.3: Validation results orange PP samples: RMSE $\times 10^{-5}$ over validation data set.

Method	G_{Voigt} FC	G_{Voigt} PC	G_{Zener} FC	G_{Zener} PC	G_{max3} FC	G_{max3} PC
1	1.4072	10.9880	1.1541	6.5167	1.1541	0.7693
2	1.3750	6.0318	1.2626	7.9880	1.0136	1.1674
3	1.1335	5.0402		4.2792	1.0877	0.9889
4	1.3196	11.4415	1.2857	7.0491	1.3829	1.8870
5	1.3214	11.4408	0.9580	17.8150	0.9690	1.2590
Opt	1.1828	5.0854	1.0652	4.3737	0.9870	3.1514
Int	1.4031	5.8456	1.0540	6.4366	1.0405	1.7367

worst values. The methods that provided the worst RMSEs for the PC setup have remained the same. Noticeable is that the optimized models no longer have the smallest RMSEs. It can be seen that good identification results can always be achieved with the help of Levy's method in combination with the iterative method of Sanathanan and Koerner, which was already shown in Section 3.4.1.

For the FC setup the best fractional-order model was not obtained with the largest model approach G_{max3}, but with the Zener model approach and method 5. This indicates that the model can be overfitted when using the largest model approach or that the low-dimensional model approaches fit better for the frequency range covered by the chirp signal. It is at least obvious that more free parameters do not lead to better fits.

In contrast, the models of higher order of the PC setup only have smaller error values. This could be because clearly fewer measuring values are available here and thus the selection of two measuring points represents a very strong deviation.

Finally, the best fractional-order models will be validated in the time domain. In order to implement such systems, a common method is to apply higher-order approximations within a certain frequency set $\Omega = \{\omega \in \mathbb{R} \,|\, \omega_l \leq \omega \leq \omega_h\}$. The Oustaloup filter [31] is given by

$$s^\alpha \approx G_{\text{f}}(s) = \omega_h^\alpha \prod_{k=-N}^{N} \frac{s + \omega_k^-}{s + \omega_k^+},$$
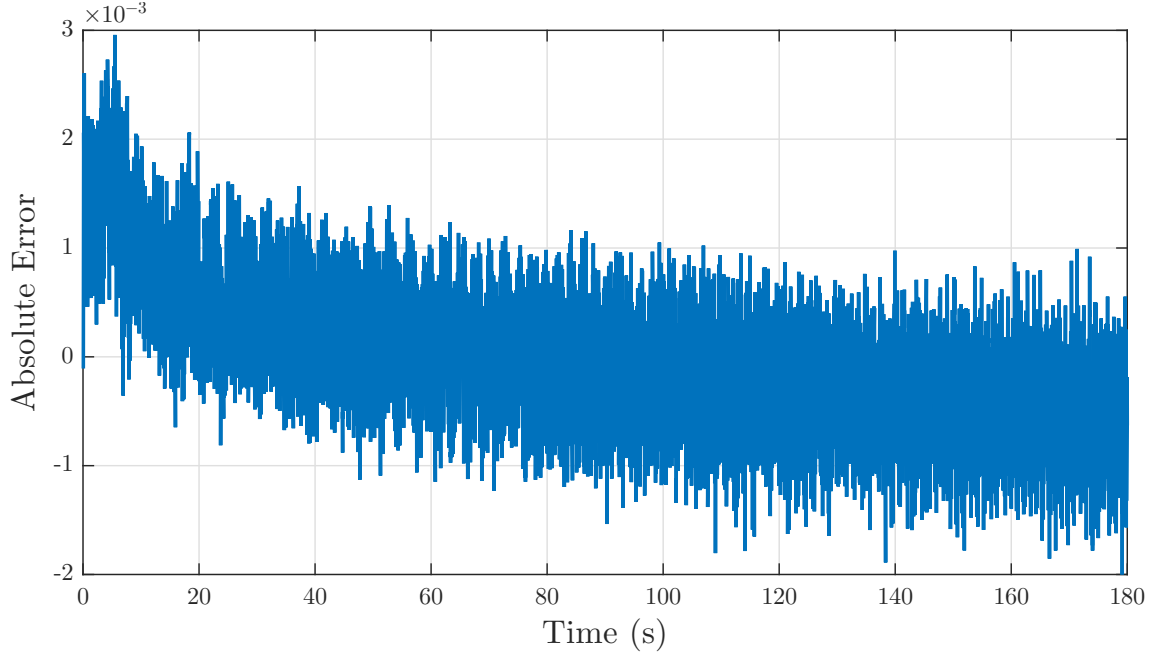
Figure 4.13: Validation in the time domain: absolute error of strain using G_{Zener} identified with method 5 (FC setup).

where $0 < \alpha < 1$ is the order of derivative, N is the order of the filter, and

$$\omega_k^\pm = \omega_l \left(\frac{\omega_h}{\omega_l} \right)^{\frac{k+N+\frac{1}{2}(1\pm\alpha)}{2N+1}}.$$

In MATLAB, the function `oustapp()` can be used to apply the Oustaloup filter to identified fractional-order models [31]. Then the absolute error between the measured validation data and the modeled time domain data can be calculated with

$$e_{\text{abs}}(k) = \epsilon_{\text{m}}(k) - G_{\text{f}}\sigma_{\text{m}}(k),$$

where ϵ_{m} contains the discrete measured strain data and σ_{m} are the discrete measured stress data. This error is shown graphically in Figures 4.13 and 4.14 for the best models for the verification data of the FC and PC setup. The corresponding strain curves over time can be found in Appendix A.3. Here it can be seen once again that the data measured with the FC setup are much noisier. The Fourier transform of this error vector displayed in Figure A.7 shows a single large peak at $0.0349 \frac{\text{rad}}{\text{s}}$. This may be caused by the slow decrease of the error values. Otherwise the signal seems to be white-noise-like. This shows that the model approximates the behavior very well and only the noise of the measured data remains.
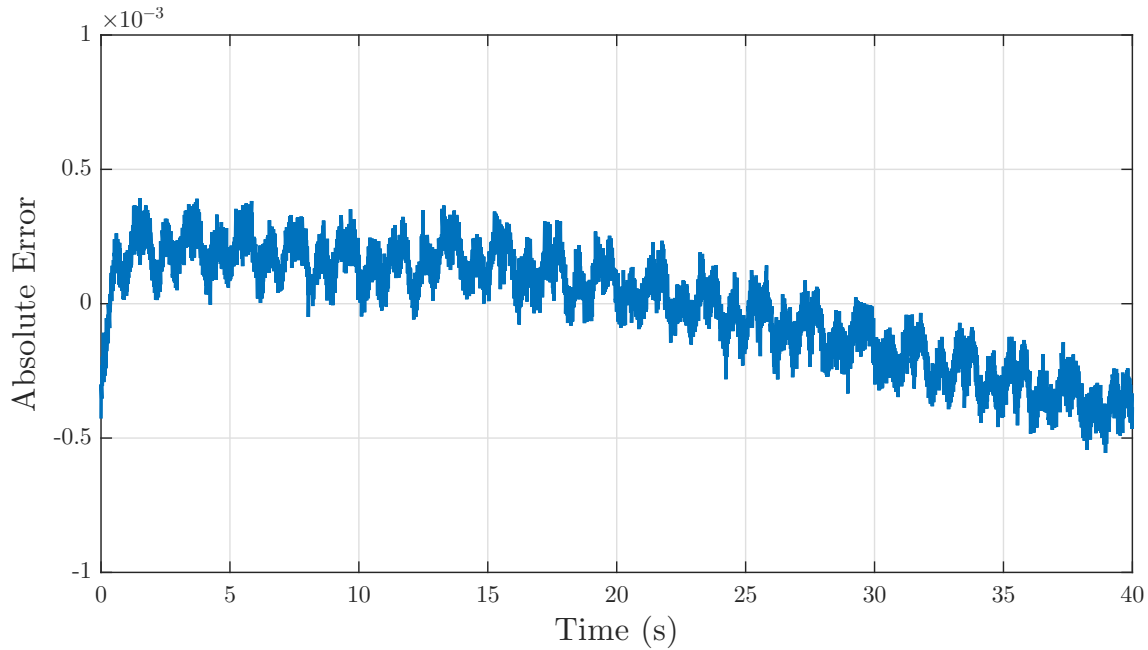
Figure 4.14: Validation in the time domain: absolute error of strain using G_{max3} identified with method 1 (PC setup).

In contrast, the curve of the error for the PC setup does not look like pure noise. There are still systematic errors, which also show up in the Fourier transformation. So, the models for PC setup seem to fit a little worse, but this is probably also due to the significantly less measured data.

4.3.4 Dashpot

Using the procedure explained in Section 3.1, a Bode diagram for the measured and simulated data can be obtained. This is shown in Figure 4.15 for the open-loop and closed-loop case.

The curves of the two simulated transfer behaviors are very similar. In comparison, the curves of the measured data differ significantly. Reasons for this can be inaccurate measurement methods, measurement errors, other environmental influences, or an incorrect Simulink model that does not adequately represent the real behavior of the test setup.

However, there is a certain similarity between the simulated data and the experimental open-loop data, neglecting the higher frequencies. The strong deviations at the higher frequencies can be explained by the fact that the system is not designed for such frequencies, these fast changes of direction are physically hardly realizable. This leads to a stronger phase shift and higher noise. As mentioned in Section 4.2,

the amplitude of the input sine in the open-loop case is set to $A = 0.1$, which corresponds to a 10% valve opening. This means that the input signal is completely within the dead zone of the servo valve. The following section explains why this can lead to complications in the results.

Let $G_\mathrm{d}(s)$ be the transfer function of the right dashpot to be identified. Then the system can be simply assumed as

$$Y_\mathrm{d}(s) = G_\mathrm{d}(s)U_\mathrm{d}(s),$$
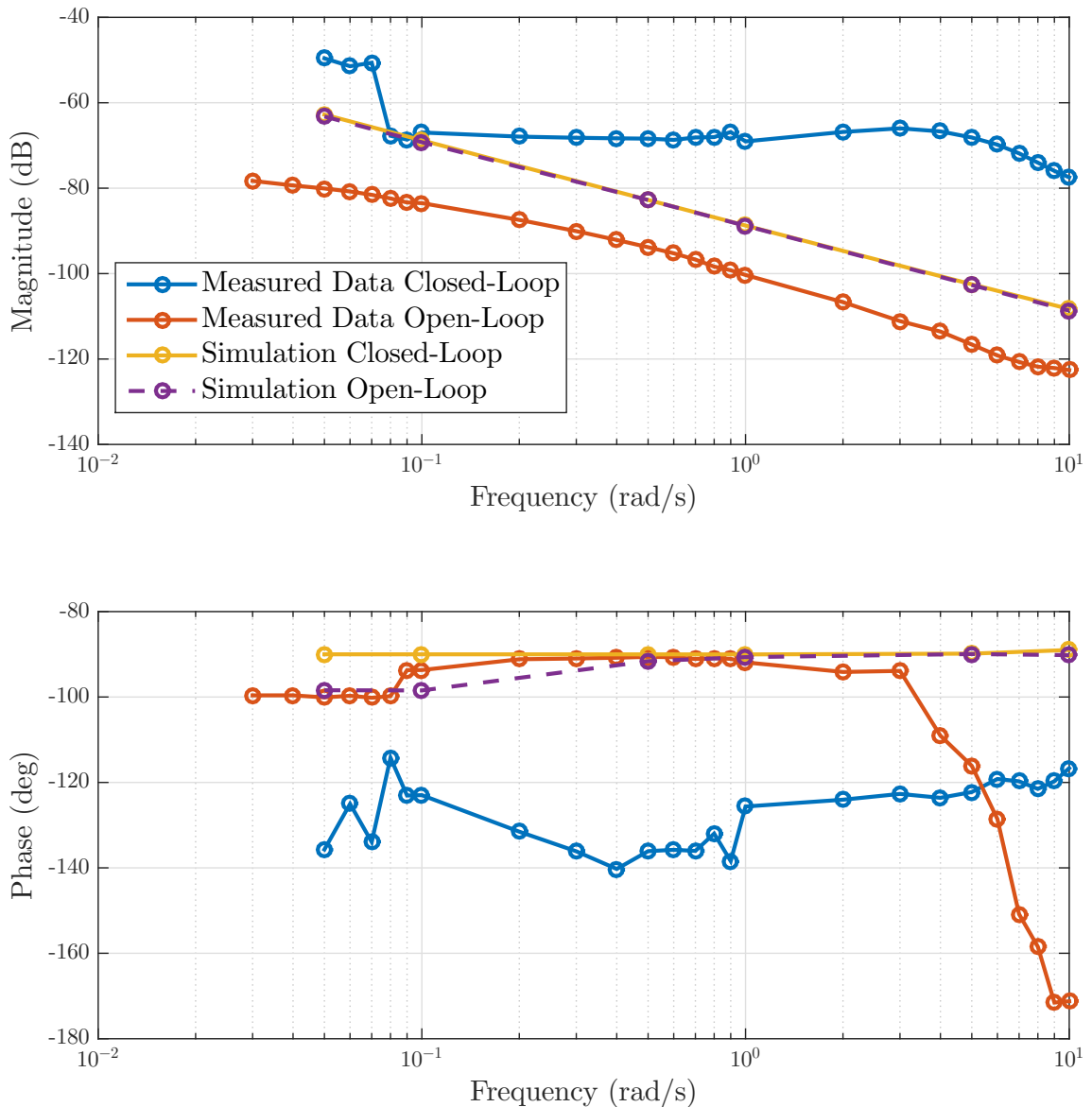
Figure 4.15: Bode diagram of open-loop and closed-loop measurements of the transfer behavior of the dashpot.

where $U_d(s)$ denotes the Laplace transform of the output signal of the nonlinear dead zone, that is

$$U_d(s) = \mathcal{L}\left\{f_{\text{deadzone}}(u_{\text{in}}(t))\right\}(s),$$

with the valve input $u_{\text{in}}(t)$. This is shown in Figure 4.16. The dead zone is approximated very simplified with the following monomial function

$$f_{\text{deadzone}}(x(t)) = 372x^5(t),$$

where the pre-factor is roughly calculated using values from the graph of the dead zone, which was determined experimentally in [26]. If the selected sine function $u_{\text{in}}(t) = 0.1\sin(\omega t)$ is then inserted, this yields

$$\begin{aligned}
f_{\text{deadzone}}(u_{\text{in}}(t)) &= 372(0.1\sin(\omega t))^5 \\
&= 372(0.1)^5 \sin^5(\omega t) \\
&= 0.00372\sin^5(\omega t).
\end{aligned} \tag{4.2}$$

Using Euler's formula $e^{jx} = \cos(x) + j\sin(x)$ and the binomial theorem, the power of the sine amounts to

$$\begin{aligned}
\sin^n(x) &= \left(\frac{e^{jx} - e^{-jx}}{2j}\right)^n \\
&= \frac{1}{(2j)^n}\sum_{k=0}^{n}\binom{n}{k}e^{j(n-k)x}(-1)^k e^{-jkx} \\
&= \begin{cases}
\dfrac{1}{2^n(-1)^{\frac{n}{2}}}\displaystyle\sum_{k=0}^{n}\binom{n}{k}(-1)^k\cos((n-2k)x), & \text{if } n \text{ is even,} \\[2em]
\dfrac{1}{2^n(-1)^{\frac{n-1}{2}}}\displaystyle\sum_{k=0}^{n}\binom{n}{k}(-1)^k\sin((n-2k)x), & \text{if } n \text{ is odd.}
\end{cases}
\end{aligned}$$

Thus, (4.2) becomes

$$\begin{aligned}
f_{\text{deadzone}}(u_{\text{in}}(t)) &= 0.00372\left(\frac{1}{16}\left(10\sin(\omega t) - 5\sin(3\omega t) + \sin(5\omega t)\right)\right) \\
&= 2.325 \times 10^{-4}\left(10\sin(\omega t) - 5\sin(3\omega t) + \sin(5\omega t)\right).
\end{aligned}$$

It can be seen that the input signal $u_d(t)$, with which the transfer function $G_d(s)$ is to be determined, does not consist of a single sine wave anymore. Therefore, as discussed in Section 3.1, multiple peaks can be detected in the FFT. This is shown
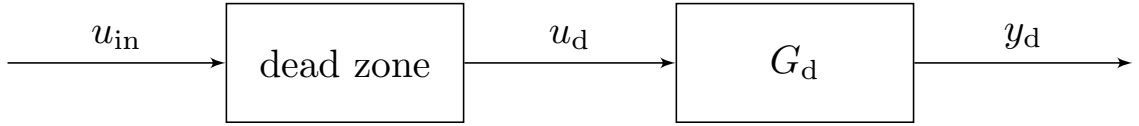
Figure 4.16: Simplified diagram of the dashpot in open-loop.
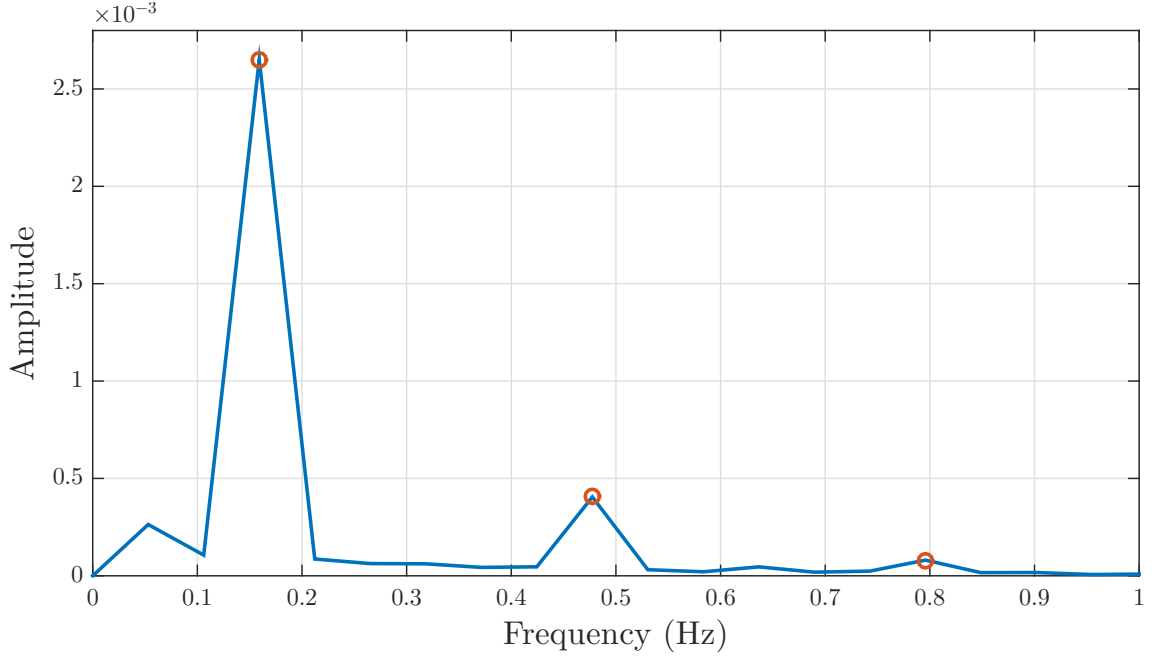
Figure 4.17: Amplitude of the FFT of the averaged measured position signal of the dashpot in open-loop for $\omega = 1\,\frac{\text{rad}}{\text{s}}$.

in Figure 4.17. Here it is easy to see that the approximation of the dead zone using the fifth power of x reflects reality well. The frequencies of the sines are clearly ω, $3\,\omega$ and $5\,\omega$ with a decreasing amplitude. This means that due to the dead zone, the amplitude is determined incorrectly, as some non-negligible parts of the amplitude are assigned to other frequencies.

The dead zone does not have this influence on the closed-loop measurements, since the control concept in [25] also includes a dead zone compensation. Nevertheless, this transfer behavior differs most from the others. The strong deviation at the beginning of the amplitude response in Figure 4.15 may be due to the fact that the measurement series for these three frequencies were recorded at a slightly later time than the others. This means that the system requirements may have changed, e.g. the supply pressure. However, it is difficult to explain why the general shapes of amplitude and phase differ so fundamentally here. A possible reason could be that by calculating the force in the dashpot with (4.1) the resulting signal is extremely noisy and obviously has no sinusoidal shape. This can be seen in Figure A.9 in
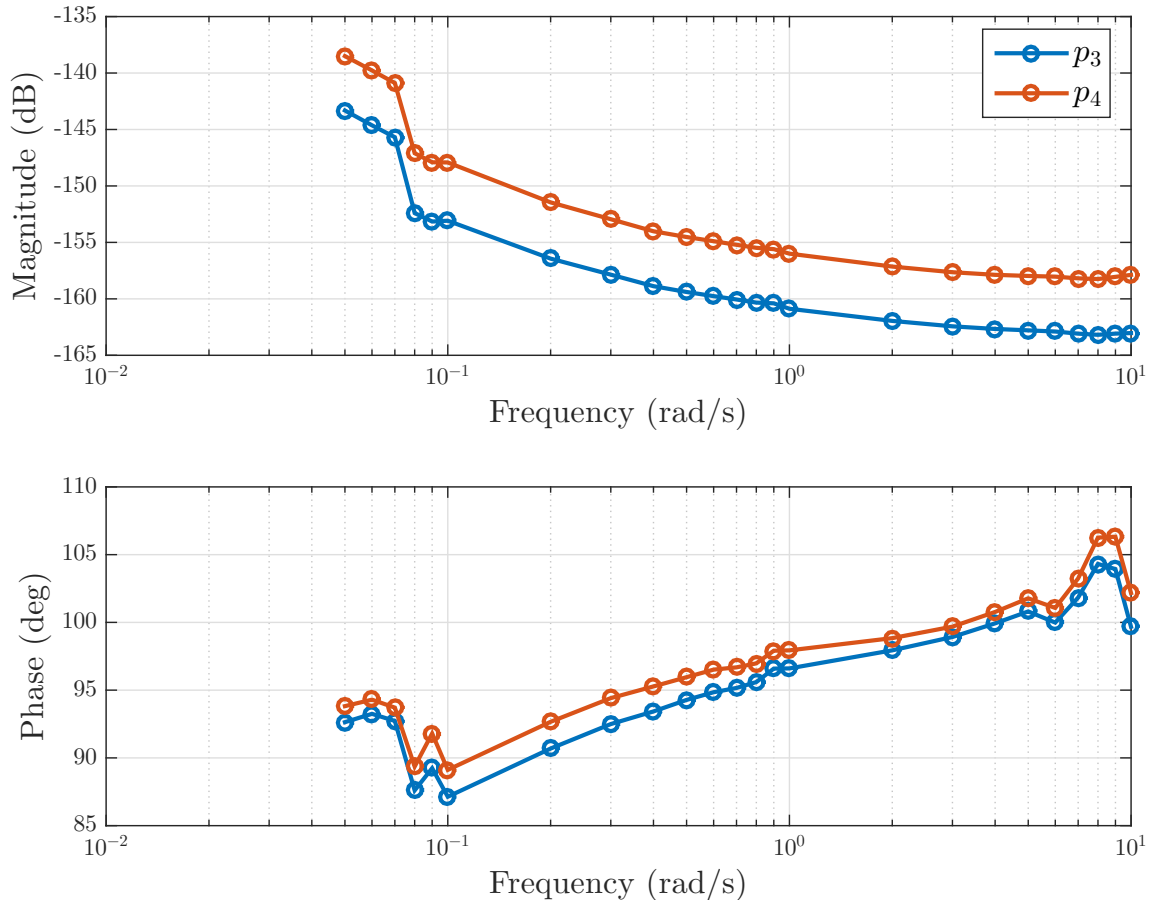
Figure 4.18: Bode diagram of closed-loop measurements with different pressures as input and the position of the dashpot as output.

the appendix. In comparison, there is also a graph showing the two pressures in Figure A.8. These look much more sinusoidal. For this reason, the transfer behavior of the dashpot was determined using the pressures instead of the calculated force. This means, Figure 4.18 shows the Bode diagram, which is generated when the pressures are chosen as input and the position as output. In comparison to the previous curves, fewer significant outliers are now visible.

As described in Section 2.5, hydraulic dashpots can also exhibit viscoelastic behavior. Therefore, it is also possible to adapt FOTF to the measurement data. Since the open-loop data tend to show the expected behavior rather than the closed-loop data, these are fitted.

A closer look at the curves of the open-loop measurements shows that the dashpot has the behavior of an integrator with an amplitude drop of $-20\,\mathrm{dB}$ per decade and a phase at about $-90°$, if the higher frequencies, at which the measurements become less accurate, are left out. Therefore, it does not seem to be reasonable to use the previously chosen approaches, since there is a fixed $a_0 = 1$ in the denominator

polynomial. Assuming that the transfer function rather takes the form $G(s) = b_0/s$, this specification is very unfavorable. For this reason, it is not advisable to choose the transfer function stable. This could also be observed in the results obtained with the previous approaches.

It is therefore decided to identify the inverse transfer function. This means that $U_{\mathrm{m}}(\mathrm{j}\omega)$ and $Y_{\mathrm{m}}(\mathrm{j}\omega)$ are swapped and the same model structures as for the polymer samples in Section 4.3.2 are fitted with

$$G(s^q) = \frac{1}{G'(s^q)},$$

where $G' = U_{\mathrm{m}}/Y_{\mathrm{m}}$. By defining $G' = B'/A'$, b_0' is in the denominator polynomial of the actually desired transfer function

$$G(s^q) = \frac{a_n' s^{nq} + \ldots + a_1' s^q + 1}{b_m' s^{mq} + \ldots + b_1' s^q + b_0'} = \frac{b_m s^{mq} + \ldots + b_1 s^q + 1}{a_n s^{nq} + \ldots + a_1 s^q + a_0}.$$

So, if this has an unwanted influence, the algorithms could make it very small.

A few other changes to the previous identification techniques still need to be made. For G'_{max3} the iterated orders change to $m_i = 1, \ldots, 3$ and $n_i = 0, \ldots, m_i$. The upper and lower bounds for the coefficients in the case of the global optimizations have been extended to -1000000 and 1000000, respectively. This is done for reasons of comparability, since the application of the algorithms leads to very high values. As already mentioned, the nonlinear inequality constraint of the optimization, which is necessary for stability, is also removed.

Figures 4.19 and 4.20 show the results of the identification using the inverted G'_{Zener} and G'_{max3} models. The results of G_{Voigt} can be seen in Figure A.10 in the appendix. Levy's Method and the iterative method of Sanathanan and Koerner require that the order $n \geq 1$. Therefore, no Voigt model can be fitted with methods 2, 3 and 5. For the models of the higher order a clear overfitting can again be seen, since the identified curves adapt very strongly to the measurement data. In particular, the assumed wrong phase drop at higher frequencies has a greater influence.

The RMSEs calculated during the identification process using $G' = U/Y$ as well as the those obtained with $G = Y/U$ are listed in Table 4.4. Since the magnitudes of the RMSEs depend very much on the value range of the transfer function values, a comparison of these values is not possible. This means, that the inversion of the transfer function also causes the inversion of the error. This probably also leads to the fact that the values for G_{max3} are sometimes significantly worse than those of the low-dimensional models and to the big difference between the best and worst
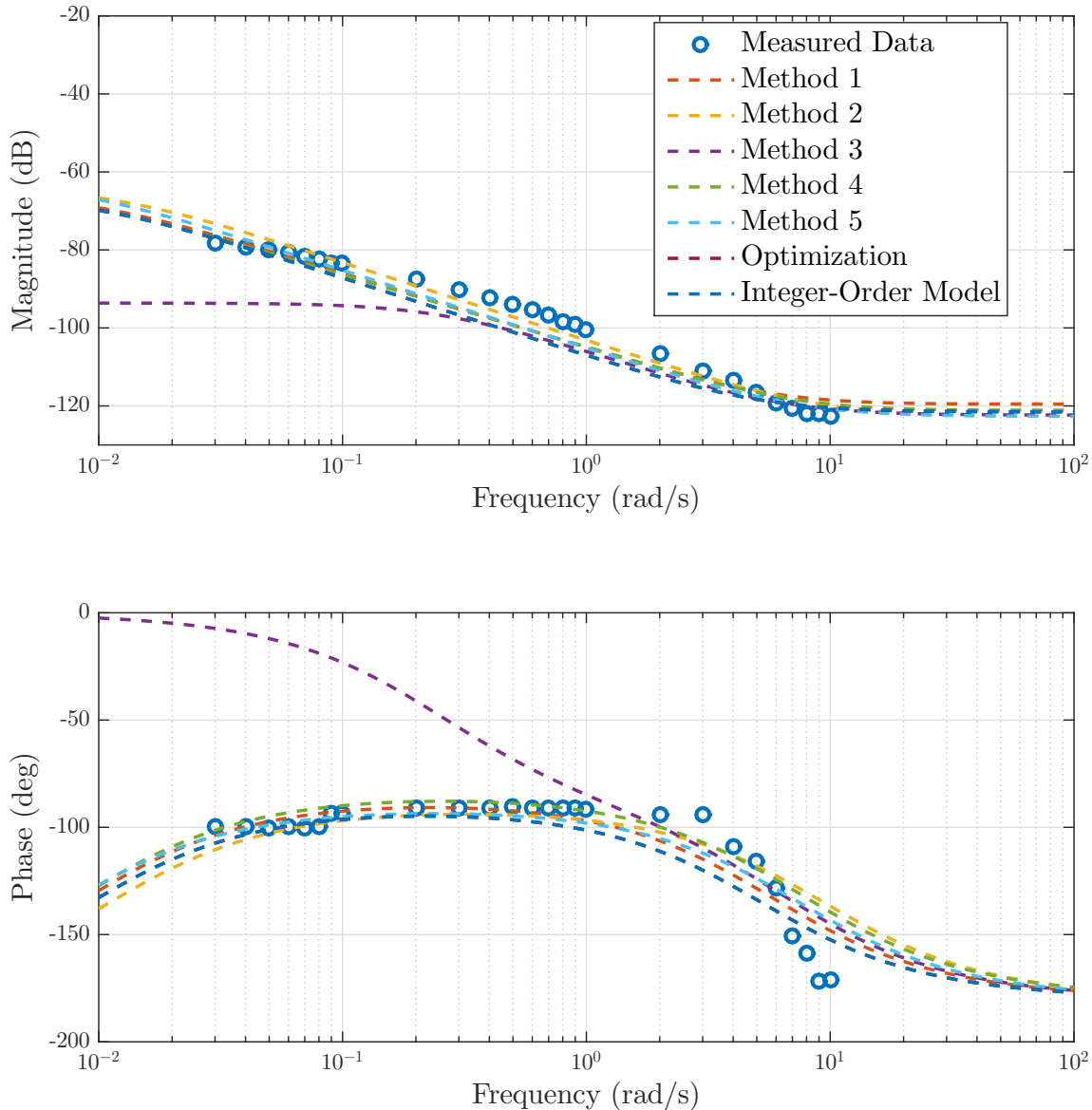
Figure 4.19: Best fit of the transfer behavior of the dashpot with open-loop data for G_{Zener}.

model for the two different transfer behaviors. For the original transfer behavior, the Zener models are obviously best.

The coefficients for these models are listed in Table A.12 in the appendix together with the results of G_{max3}. The results for the Voigt model approach can be found in Appendix A.4, too. The commensurate order identified by most of the algorithms is $q = 1$ in case of the Zener model approach which seems to cover the behavior best. The results do not seem to vary as much as with the polymer samples.

This shows that the approximation of a fractional-order model is not necessary in this case. This could look different if instead of choosing the force as input and

Table 4.4: Identification results dashpot open-loop measurements: RMSE.

Method	G_{Voigt} $\times 10^{-6}$	G_{Zener} $\times 10^{-6}$	G_{max3} $\times 10^{-6}$	G'_{Voigt} $\times 10^{4}$	G'_{Zener} $\times 10^{4}$	G'_{max3} $\times 10^{4}$
1	8.7003	2.1694	0.3560	10.9571	4.6189	3.5560
2		4.8881	2.3458		5.2823	0.8023
3		10.1263	8.6925		4.3612	0.8134
4	9.4096	2.1826	6.0428	10.9543	5.0616	1.8280
5		2.8026	4.8181		4.4400	0.7797
Opt	10.1932	2.5529	9.9957	8.8712	3.9010	0.71268
Int	10.1932	2.5529	16.2399	8.8712	3.9010	0.7210

the position of the cylinder as output, the velocity is chosen as output. However, it is difficult to make generalized statements, since the measurement data are very poor and therefore a considerable uncertainty already exists. Additionally, there is another source of error by inverting the models, because the error is inverted too and the assumption of the algorithms that the noise is white-noise-like might be violated. A further problem can be that nonlinear influences exist which cannot be approximated by linear models.
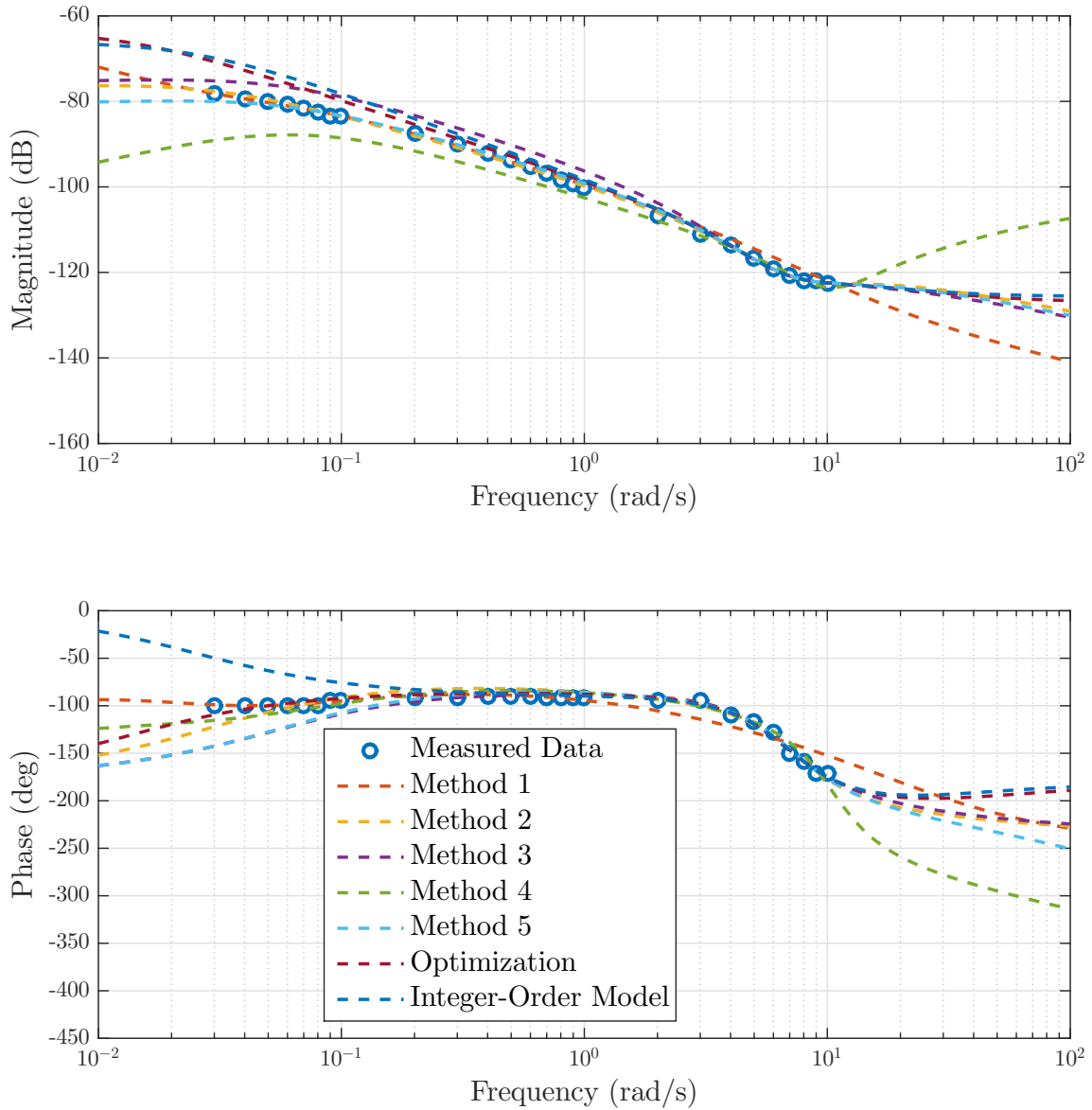
Figure 4.20: Best fit of the transfer behavior of the dashpot with open-loop data for G_{max3}.

5 Conclusion

In this thesis, different approaches to identify fractional-order transfer functions in the frequency domain are presented. The aim was to verify these algorithms with real measurement data of different materials and applications showing viscoelastic behavior.

First, after a short introduction of the fractional calculus, the best-known integer-order models for the representation of viscoelastic behavior are introduced. The transfer to corresponding fractional-order models is also described at this point. Subsequently, hydraulic dashpots are presented, which can exhibit viscoelastic properties and are included in the experimental investigations. There are also some theoretical considerations about noise, because the measured data are partly very noisy, and these ideas show an advantage of the investigation in the frequency domain.

A whole chapter is then devoted to the possibilities of identifying the fractional-order transfer functions. First, some literature-based algorithms are presented and explained, which are further developments of integer-order algorithms. These algorithms require a priori knowledge of the system structure including the commensurate order. In addition, an optimization of the coefficients and the commensurate order of the FOTF is introduced and implemented. In subsequent simulation studies, the functionality of the presented approaches is examined. These show that often Levy's algorithm with the iterative method of Sanathanan and Koerner provides the smallest RMSE. Furthermore, it turns out that the error in q is a non-convex function and therefore finding a global solution when using a simple optimization such as the steepest descent strongly depends on the selected initial value. The use of a global optimization, which tries to find several local solutions by starting from different initial values, leads to significantly improved results.

The transfer behaviors of polymer samples (PP and PBT) and of a hydraulic dashpot (closed-loop and open-loop) have been measured. The results are depicted in Bode diagrams.

Regarding the measurement data of the polymers, it can be stated that it is essential to use the position-controlled approach in order to increase the repeatability

of the measurements. The test sample is forced back to its original shape, so that the influence of the load history is reduced. However, considerably less data could be recorded at this experimental setup, which has a negative effect on the subsequent model identification and validation. Since the PBT samples should have purely elastic properties at the temperature at which the investigations were carried out and the white and orange PP samples do not differ fundamentally in their transfer behavior, only the results of the orange PP samples are presented in this thesis.

Three different model structures are fitted, the Voigt and Zener as well as a higher order fractional-order transfer function. The model identification methods used are the previously introduced algorithms and global optimization as well as a global optimization to identify models of integer order. The resulting models must meet the requirement for stability. It is shown that a significantly better fit is achieved with a higher model order. The investigations also indicate that fractional-order transfer functions represent the viscoelastic behavior more accurately than integer-order transfer functions of the same order. It can also be assumed that the algorithms would show better results if the unstable transfer functions are not subsequently removed. In addition, it is difficult to verify the functionality of the global optimization, as it has already been demonstrated that it does not always deliver the best results. The transfer functions found show that for a low model order the parameters are very similar. However, the higher the order, the more variations there are. For similar coefficients of small order models (e.g. Voigt) very similar commensurate orders q result. However, slight variations can quickly lead to very large fluctuations in the commensurate order.

When validating with data sets that are not used to fit the models, there is a change in the best fit away from global optimization to methods 1 to 5. Furthermore, the higher parametric models for the FC setup are no longer clearly better, but probably lead to an overfitting of the data. This shows that not only with the algorithms but also with low-order models the viscoelastic behavior can be well represented. Nevertheless, additional considerations, such as the high-frequency behavior, should be mentioned in order to select a suitable model. It would also be possible to use stochastic measures of model order selection techniques to investigate the models in more detail. Additional for the validation of the PC setup results, e.g. cross-correlation studies can be used to minimize the possibility of a poor data point selection. Furthermore, it is also possible to determine the physical parameters of the polymer samples in future investigations using the identified transfer functions. The residuals from the identification can also be subject to further examination to find out whether there are any remaining systematic errors.

The evaluation of the dashpot experiments leads to partly very unexpected Bode diagrams. This may indicate that there are nonlinearities in the system which cannot be fitted with linear models. In case of the open-loop studies, the dead zone of the servo valve can lead to complications. This behavior seems to be integrator-like. Therefore, the structure of the investigated algorithms is not suitable to identify the transfer function models. To solve this problem, the measured transfer behavior is inverted, and the inverted fractional-order models are fitted. The Zener models seem to identify this behavior best, and the resulting models are mostly integer-order models. This suggests that the dashpot with the selected inputs and outputs shows no fractional-order transfer behavior. This may well be due to the poor and very noisy measurements.

It was possible to identify the measured transfer functions of the polymer samples using low-dimensional fractional-order models. For very similar model structures with a small number of parameters, the identified models show some similarities, but the differences increase significantly with growing order. The dashpot studied for this thesis is more likely to be approximated by integer-order models. In both cases, however, it has to be admitted that due to the unfavorable measurement conditions many problems of identification can be put at the expense of the poor measurement data. For future investigations it would be interesting to see whether the algorithms also provide similar results with measurement data obtained with a lower probability of systematic errors.

A Appendix

A.1 Simulation Studies: Tables

Table A.1: Simulation studies: algorithms (averaged parameter vector over 10000 runs and variance of the results with $\sigma = 0.001$, $q = 0.5$, $n = 1$ and $m = 1$).

Method	Averaged coefficients	Variance of the coefficients $\times 10^{-4}$
1	$a = \begin{bmatrix} 1 & 0.9948 \end{bmatrix}$,	$\sigma_a^2 = \begin{bmatrix} 0 & 10.1675 \end{bmatrix}$,
	$b = \begin{bmatrix} 0.9984 & -0.0013 \end{bmatrix}$	$\sigma_b^2 = \begin{bmatrix} 1.8887 & 0.2752 \end{bmatrix}$
2	$a = \begin{bmatrix} 1 & 0.9963 \end{bmatrix}$,	$\sigma_a^2 = \begin{bmatrix} 0 & 2.1930 \end{bmatrix}$,
	$b = \begin{bmatrix} 0.9984 & -0.0004 \end{bmatrix}$	$\sigma_b^2 = \begin{bmatrix} 0.6472 & 0.0254 \end{bmatrix}$
3	$a = \begin{bmatrix} 1 & 0.9989 \end{bmatrix}$,	$\sigma_a^2 = \begin{bmatrix} 0 & 1.2065 \end{bmatrix}$,
	$b = \begin{bmatrix} 0.9995 & -0.0001 \end{bmatrix}$	$\sigma_b^2 = \begin{bmatrix} 0.4026 & 0.0146 \end{bmatrix}$
4	$a = \begin{bmatrix} 1 & 0.9997 \end{bmatrix}$,	$\sigma_a^2 = \begin{bmatrix} 0 & 7.9542 \end{bmatrix}$,
	$b = \begin{bmatrix} 0.9999 & -0.0001 \end{bmatrix}$	$\sigma_b^2 = \begin{bmatrix} 0.2020 & 0.6184 \end{bmatrix}$
5	$a = \begin{bmatrix} 1 & 0.9965 \end{bmatrix}$,	$\sigma_a^2 = \begin{bmatrix} 0 & 0.9622 \end{bmatrix}$,
	$b = \begin{bmatrix} 0.9984 & -0.0002 \end{bmatrix}$	$\sigma_b^2 = \begin{bmatrix} 0.2523 & 0.0332 \end{bmatrix}$

Table A.2: Simulation studies: algorithms (averaged RMSE over 10000 runs and variance of the RMSE for G_{ref} and G_{noise} with $\sigma = 0.001$, $q = 0.5$, $n = 1$ and $m = 1$).

Method	Mean RMSE with G_{spec} $\times 10^{-4}$	Variance RMSE with G_{spec} $\times 10^{-8}$	Mean RMSE with G_{noise} $\times 10^{-4}$	Variance RMSE with G_{noise} $\times 10^{-8}$
1	6.1425	9.2972	11.3107	5.4620
2	2.8526	1.5611	9.7315	2.0643
3	2.2822	1.2675	9.5670	1.9496
4	9.1282	24.5144	13.4264	13.6890
5	4.3684	6.5408	10.4361	3.2819

Table A.3: Simulation studies: algorithms (averaged parameter vector over 10000 runs and variance of the results with $\sigma = 0.001$, $q = 0.25$, $n = 2$ and $m = 2$).

Method	Averaged coefficients	Variance of the coefficients
1	$a = \begin{bmatrix} 1 & 0.1069 & 0.6263 \end{bmatrix}$, $b = \begin{bmatrix} 1.1292 & -0.3346 & 0.0723 \end{bmatrix}$	$\sigma_a^2 = \begin{bmatrix} 0 & 0.0387 & 0.0631 \end{bmatrix}$, $\sigma_b^2 = \begin{bmatrix} 0.0182 & 0.0403 & 0.0014 \end{bmatrix}$
2	$a = \begin{bmatrix} 1 & 0.0442 & 0.9059 \end{bmatrix}$, $b = \begin{bmatrix} 1.0334 & -0.0705 & 0.0122 \end{bmatrix}$	$\sigma_a^2 = \begin{bmatrix} 0 & 0.0129 & 0.0073 \end{bmatrix}$, $\sigma_b^2 = \begin{bmatrix} 0.0049 & 0.0043 & 0.0001 \end{bmatrix}$
3	$a = \begin{bmatrix} 1 & 0.0606 & 0.9420 \end{bmatrix}$, $b = \begin{bmatrix} 1.0388 & -0.0433 & 0.0065 \end{bmatrix}$	$\sigma_a^2 = \begin{bmatrix} 0 & 0.0283 & 0.0173 \end{bmatrix}$, $\sigma_b^2 = \begin{bmatrix} 0.0112 & 0.0103 & 0.0002 \end{bmatrix}$
4	$a = \begin{bmatrix} 1 & 0.1330 & 0.6851 \end{bmatrix}$, $b = \begin{bmatrix} 1.1249 & -0.2690 & 0.0564 \end{bmatrix}$	$\sigma_a^2 = \begin{bmatrix} 0 & 0.0967 & 0.2374 \end{bmatrix}$, $\sigma_b^2 = \begin{bmatrix} 0.0521 & 0.1605 & 0.0062 \end{bmatrix}$
5	$a = \begin{bmatrix} 1 & 0.1457 & 0.8448 \end{bmatrix}$, $b = \begin{bmatrix} 1.0886 & -0.1057 & 0.0153 \end{bmatrix}$	$\sigma_a^2 = \begin{bmatrix} 0 & 0.0239 & 0.0137 \end{bmatrix}$, $\sigma_b^2 = \begin{bmatrix} 0.0074 & 0.0069 & 0.0002 \end{bmatrix}$

Table A.4: Simulation studies: algorithms (averaged RMSE over 10000 runs and variance of the RMSE for G_{ref} and G_{noise} with $\sigma = 0.001$, $q = 0.25$, $n = 2$ and $m = 2$).

Method	Mean RMSE with G_{spec} $\times 10^{-3}$	Variance RMSE with G_{spec} $\times 10^{-6}$	Mean RMSE with G_{noise} $\times 10^{-3}$	Variance RMSE with G_{noise} $\times 10^{-6}$
1	3.1417	9.1396	3.3116	8.8555
2	0.4314	0.0204	0.9853	0.0251
3	0.3623	0.0210	0.9569	0.0219
4	4.4785	35.3426	4.6783	34.4486
5	0.6078	0.0550	1.0848	0.0386

Table A.5: Simulation studies: optimization (1000 runs, $\sigma = 0.001$, $n = 2$ and $m = 2$, part 1).

$x_0^\top$	$\begin{bmatrix} 0.5 & 0.5 & 0.5 & 0.5 & 0.5 & 0.1 \end{bmatrix}$	$\begin{bmatrix} -0.5 & 0.5 & 0.5 & 0.5 & 0.5 & 0.1 \end{bmatrix}$
$\bar{a}$	$\begin{bmatrix} 1 & 9.7620 & 8.8087 \end{bmatrix}$	$\begin{bmatrix} 1 & 8.3781 & 7.4182 \end{bmatrix}$
$\mathrm{Var}(a)$	$\begin{bmatrix} 0 & 280.6334 & 277.0976 \end{bmatrix}$	$\begin{bmatrix} 0 & 18.7990 & 17.0455 \end{bmatrix}$
$\bar{b}$	$\begin{bmatrix} 1.0991 & 8.7117 & -0.0215 \end{bmatrix}$	$\begin{bmatrix} 0.9905 & 7.4089 & -0.0022 \end{bmatrix}$
$\mathrm{Var}(b)$	$\begin{bmatrix} 0.4013 & 278.5133 & 0.0168 \end{bmatrix}$	$\begin{bmatrix} 0.0577 & 17.3309 & 0.0026 \end{bmatrix}$
$\bar{q}$	0.4831	0.4995
$\mathrm{Var}(q)$	5.1489×10^{-3}	1.5945×10^{-4}
Mean RMSE with G_{spec} $\times 10^{-4}$	5.3899	<mark>3.0339</mark>
Variance RMSE with G_{spec}	1.3983×10^{-6}	1.5727×10^{-8}
Mean RMSE with G_{noise} $\times 10^{-4}$	11.2805	9.3163
Variance RMSE with G_{noise}	1.1731×10^{-6}	1.8977×10^{-8}

Table A.6: Simulation studies: optimization (1000 runs, $\sigma = 0.001$, $n = 2$ and $m = 2$, part 2).

$x_0^\top$	$\begin{bmatrix} 0.5 & 0.5 & 0.5 & 0.5 & 0.5 & 1 \end{bmatrix}$	$\begin{bmatrix} -0.5 & 0.5 & 0.5 & 0.5 & 0.5 & 1 \end{bmatrix}$
$\bar{a}$	$\begin{bmatrix} 1 & 5.1492 & 12.6855 \end{bmatrix}$	$\begin{bmatrix} 1 & 31.3166 & 30.4820 \end{bmatrix}$
$\mathrm{Var}(a)$	$\begin{bmatrix} 0 & 0.0501 & 5.6528 \end{bmatrix} \times 10^{-4}$	$\begin{bmatrix} 0 & 3.6875 & 0.6190 \end{bmatrix}$
$\bar{b}$	$\begin{bmatrix} -1.6210 & 0.5380 & 5.7133 \end{bmatrix}$	$\begin{bmatrix} 0.9609 & 30.4430 & -0.0081 \end{bmatrix}$
$\mathrm{Var}(b)$	$\begin{bmatrix} 0.1907 & 1.6068 & 1.5147 \end{bmatrix} \times 10^{-4}$	$\begin{bmatrix} 0.2756 & 0.0118 & 0.0153 \end{bmatrix}$
$\bar{q}$	1.0978×10^{-7}	0.4996
$\mathrm{Var}(q)$	9.5824×10^{-15}	1.4635×10^{-4}
Mean RMSE with G_{spec} $\times 10^{-4}$	`452.5970`	3.0477
Variance RMSE with G_{spec}	4.7178×10^{-13}	1.5762×10^{-8}
Mean RMSE with G_{noise} $\times 10^{-4}$	`452.6772`	`9.3115`
Variance RMSE with G_{noise}	7.7618×10^{-9}	1.8988×10^{-8}

Table A.7: Simulation studies: global optimization (100 runs, $\sigma = 0.001$, multi start).

Orders	$n = 1, m = 0$	$n = 1, m = 1$	$n = 2, m = 2$
$\overline{a}$	$\begin{bmatrix} 1 & 1.0009 \end{bmatrix}$	$\begin{bmatrix} 1 & 1.0010 \end{bmatrix}$	$\begin{bmatrix} 1 & 45.3903 & 44.2364 \end{bmatrix}$
$\overline{b}$	$\begin{bmatrix} 1.0006 \end{bmatrix}$	$\begin{bmatrix} 1.0006 & -0.0000 \end{bmatrix}$	$\begin{bmatrix} 1.0231 & 44.2933 & 0.0008 \end{bmatrix}$
$\mathrm{Var}(a)$	$\begin{bmatrix} 0 & 1.3654 \end{bmatrix} \times 10^{-4}$	$\begin{bmatrix} 0 & 2.4027 \end{bmatrix} \times 10^{-4}$	$\begin{bmatrix} 0 & 544.6653 & 531.9798 \end{bmatrix}$
$\mathrm{Var}(b)$	$\begin{bmatrix} 6.0778 \end{bmatrix} \times 10^{-5}$	$\begin{bmatrix} 9.4542 & 0.8066 \end{bmatrix} \times 10^{-5}$	$\begin{bmatrix} 0.5869 & 533.0843 & 0.0377 \end{bmatrix}$
$\overline{q}$	0.4998	0.4998	0.5012
$\mathrm{Var}(q)$	4.5006×10^{-5}	3.6767×10^{-5}	1.6159×10^{-4}
Mean RMSE with G_{spec} $\times 10^{-4}$	2.4991	2.8640	3.1031
Variance RMSE with G_{spec} $\times 10^{-8}$	1.8020	1.9921	1.7875
Mean RMSE with G_{noise} $\times 10^{-4}$	9.2988	9.1765	9.1088
Variance RMSE with G_{noise} $\times 10^{-8}$	1.9265	2.0411	2.0519

A.2 Experiments with Polymer Samples: Tables

Table A.8: Identification results orange PP samples for G_{Zener}: coefficients and commensurate order.

Method		FC	PC
1	a	$\begin{bmatrix} 1 & 2.2951 \end{bmatrix}$,	$\begin{bmatrix} 1 & 60.4044 \end{bmatrix}$,
	b	$\begin{bmatrix} 0.0014 & 0.0027 \end{bmatrix}$,	$\begin{bmatrix} 0.0161 & 0.0499 \end{bmatrix}$,
	q	0.73	0.21
2	a	$\begin{bmatrix} 1 & 0.6556 \end{bmatrix}$,	$\begin{bmatrix} 1 & 1.7355 \end{bmatrix}$,
	b	$\begin{bmatrix} 0.0014 & 0.0007 \end{bmatrix}$,	$\begin{bmatrix} 0.0017 & 0.0012 \end{bmatrix}$,
	q	0.74	0.28
3	a		$\begin{bmatrix} 1 & 0.0002 \end{bmatrix}$,
	b		$\begin{bmatrix} 0.0011 & -0.0000 \end{bmatrix}$,
	q		0.57
4	a	$\begin{bmatrix} 1 & 3.6306 \end{bmatrix}$,	$\begin{bmatrix} 1 & 7.9200 \end{bmatrix}$,
	b	$\begin{bmatrix} 0.0016 & 0.0043 \end{bmatrix}$,	$\begin{bmatrix} 0.0034 & 0.0061 \end{bmatrix}$,
	q	0.55	0.22
5	a	$\begin{bmatrix} 1 & 2.8421 \end{bmatrix}$,	$\begin{bmatrix} 1 & 1.5213 \end{bmatrix}$,
	b	$\begin{bmatrix} 0.0015 & 0.0032 \end{bmatrix}$,	$\begin{bmatrix} 0.0015 & 0.0009 \end{bmatrix}$,
	q	0.7	0.43
Opt	a	$\begin{bmatrix} 1 & 3.3787 \end{bmatrix}$,	$\begin{bmatrix} 1 & 0.0002 \end{bmatrix}$,
	b	$\begin{bmatrix} 0.0014 & 0.0039 \end{bmatrix}$,	$\begin{bmatrix} 0.0012 & -0.0000 \end{bmatrix}$,
	q	0.7030	0.4203
Int	a	$\begin{bmatrix} 1 & 4.4548 \end{bmatrix}$,	$\begin{bmatrix} 1 & 0.0044 \end{bmatrix}$,
	b	$\begin{bmatrix} 0.0014 & 0.0053 \end{bmatrix}$	$\begin{bmatrix} 0.0011 & 0.0000 \end{bmatrix}$

Table A.9: Identification results orange PP samples for G_{max3}: coefficients and commensurate order.

Method		FC	PC
1	a	$\begin{bmatrix} 1 & 2.2951 \end{bmatrix}$,	$\begin{bmatrix} 1 & 11.2894 & 5.2941 & 0.0000 \end{bmatrix}$,
	b	$\begin{bmatrix} 0.0014 & 0.0027 \end{bmatrix}$,	$\begin{bmatrix} 0.0014 & 0.0124 & 0.0051 & -0.0000 \end{bmatrix}$,
	q	0.73	0.84
2	a	$\begin{bmatrix} 1 & 0.7367 & -0.0635 & 0.0043 \end{bmatrix}$,	$\begin{bmatrix} 1 & 14.0493 & -1.2076 & 0.0891 \end{bmatrix}$,
	b	$\begin{bmatrix} 0.0014 & 0.0007 \end{bmatrix}$,	$\begin{bmatrix} 0.0029 & 0.0133 & -0.0012 \end{bmatrix}$,
	q	0.6	0.55
3	a	$\begin{bmatrix} 1 & 8.2079 & 0.1379 \end{bmatrix}$,	$\begin{bmatrix} 1 & 14.0493 & -1.2076 & 0.0891 \end{bmatrix}$,
	b	$\begin{bmatrix} 0.0015 & 0.0097 & 0.0002 \end{bmatrix}$,	$\begin{bmatrix} 0.0029 & 0.0133 & -0.0012 \end{bmatrix}$,
	q	0.86	0.35
4	a	$\begin{bmatrix} 1 & -4.2455 & 5.1113 \end{bmatrix}$,	$\begin{bmatrix} 1 & 10.8617 & 1.2948 & 0.0028 \end{bmatrix}$,
	b	$\begin{bmatrix} 0.0011 & -0.0050 & 0.0062 \end{bmatrix}$,	$\begin{bmatrix} 0.0013 & 0.0113 & 0.0012 \end{bmatrix}$,
	q	0.22	1
5	a	$\begin{bmatrix} 1 & -0.3138 & 0.0927 \end{bmatrix}$,	$\begin{bmatrix} 1 & 3.0614e7 & -1.6290e7 & 3.1067e6 \end{bmatrix}$,
	b	$\begin{bmatrix} 0.0017 & -0.0012 & 0.0004 \end{bmatrix}$,	$\begin{bmatrix} 1.1135e4 & 1.1758e4 & -4.1266e3 \end{bmatrix}$,
	q	0.21	0.17
Opt	a	$\begin{bmatrix} 1 & 5.6708 & 4.0534 & 0.0001 \end{bmatrix}$,	$\begin{bmatrix} 1 & 1.8585 & 0.9880 & 0.1527 \end{bmatrix}$,
	b	$\begin{bmatrix} 0.0014 & 0.0072 & 0.0045 & 0.0001 \end{bmatrix}$,	$\begin{bmatrix} 0.0022 & -0.0000 & 0.0024 & -0.0002 \end{bmatrix}$,
	q	0.7082	0.2874
Int	a	$\begin{bmatrix} 1 & 11.1164 & 5.3111 & 0.0010 \end{bmatrix}$,	$\begin{bmatrix} 1 & 25.2731 & 18.8599 & 0.0402 \end{bmatrix}$,
	b	$\begin{bmatrix} 0.0014 & 0.0140 & 0.0062 & 0.0001 \end{bmatrix}$	$\begin{bmatrix} 0.0015 & 0.0289 & 0.0184 & -0.0000 \end{bmatrix}$

Table A.10: Validation results orange PP samples: relative error of validation data to fitting data.

Method	G_{Voigt} FC	G_{Voigt} PC	G_{Zener} FC	G_{Zener} PC	G_{max3} FC	G_{max3} PC
1	0.7766	1.7223	0.8962	1.1038	0.8962	0.9707
2	0.8035	1.1742	0.7135	1.3675	1.0731	1.9952
3	0.6269	1.3258		1.2422	0.9274	2.4527
4	0.7005	1.7512	0.8584	1.2133	0.9348	1.4277
5	0.7013	1.7512	0.6530	1.9815	0.9953	1.8359
Opt	0.7743	1.3497	0.8885	1.3317	1.4004	1.5855
Int	0.6612	1.3016	0.8782	1.5337	1.6819	2.0791

A.3 Experiments with Polymer Samples: Figures
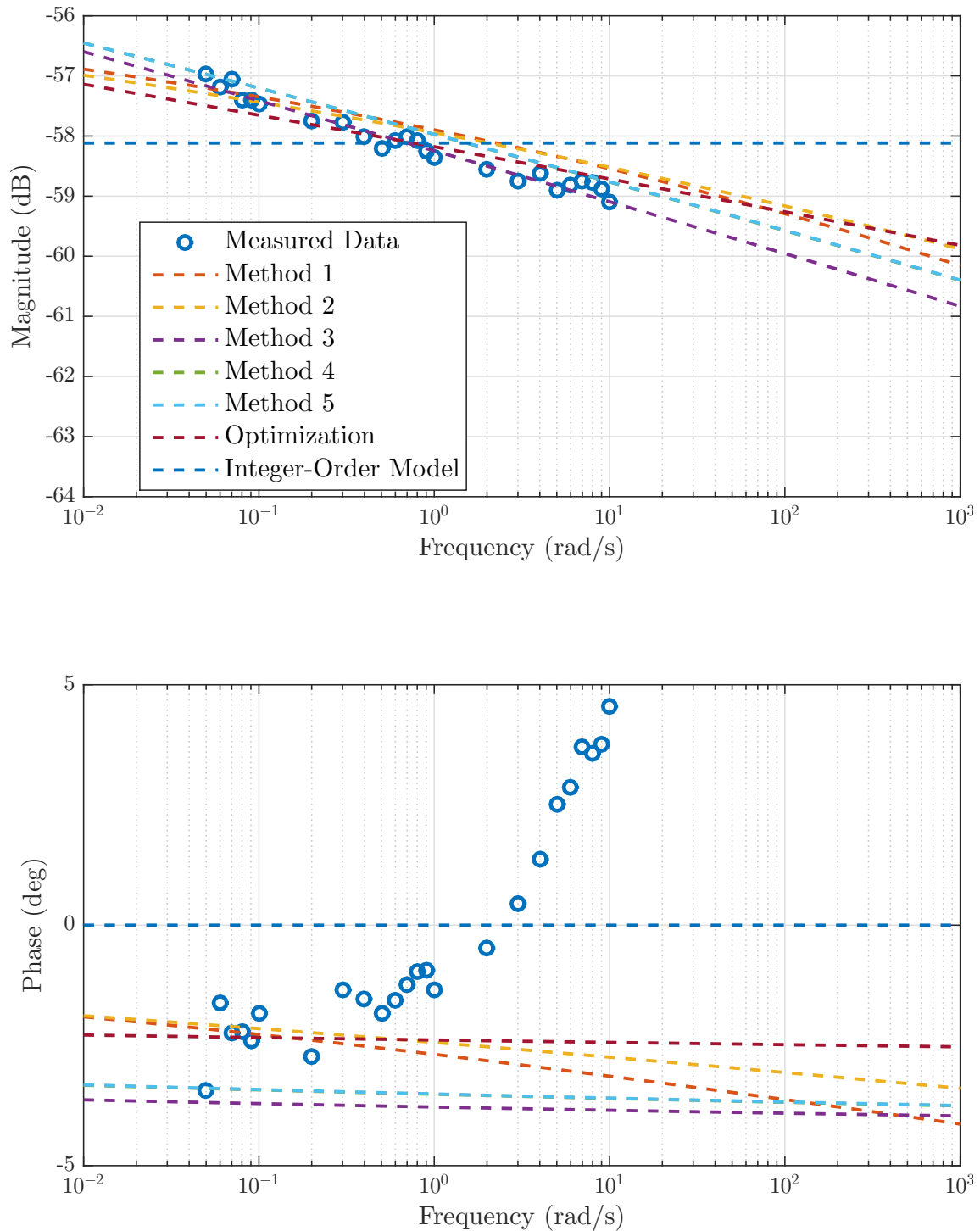
Figure A.1: Best fit of the transfer behavior of PP for G_{Voigt} (orange sample, FC setup).
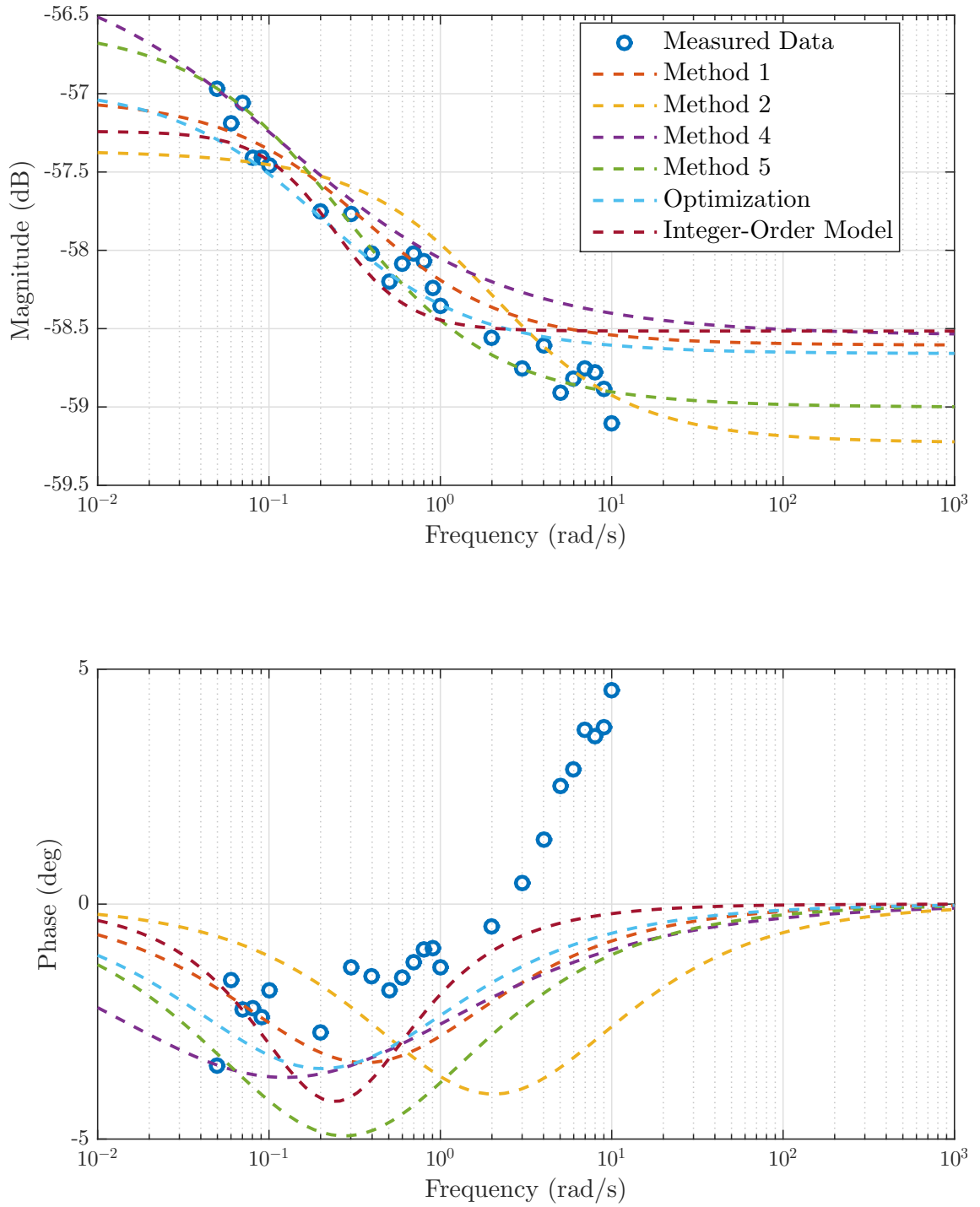
Figure A.2: Best fit of the transfer behavior of PP for G_{Zener} (orange sample, FC setup).
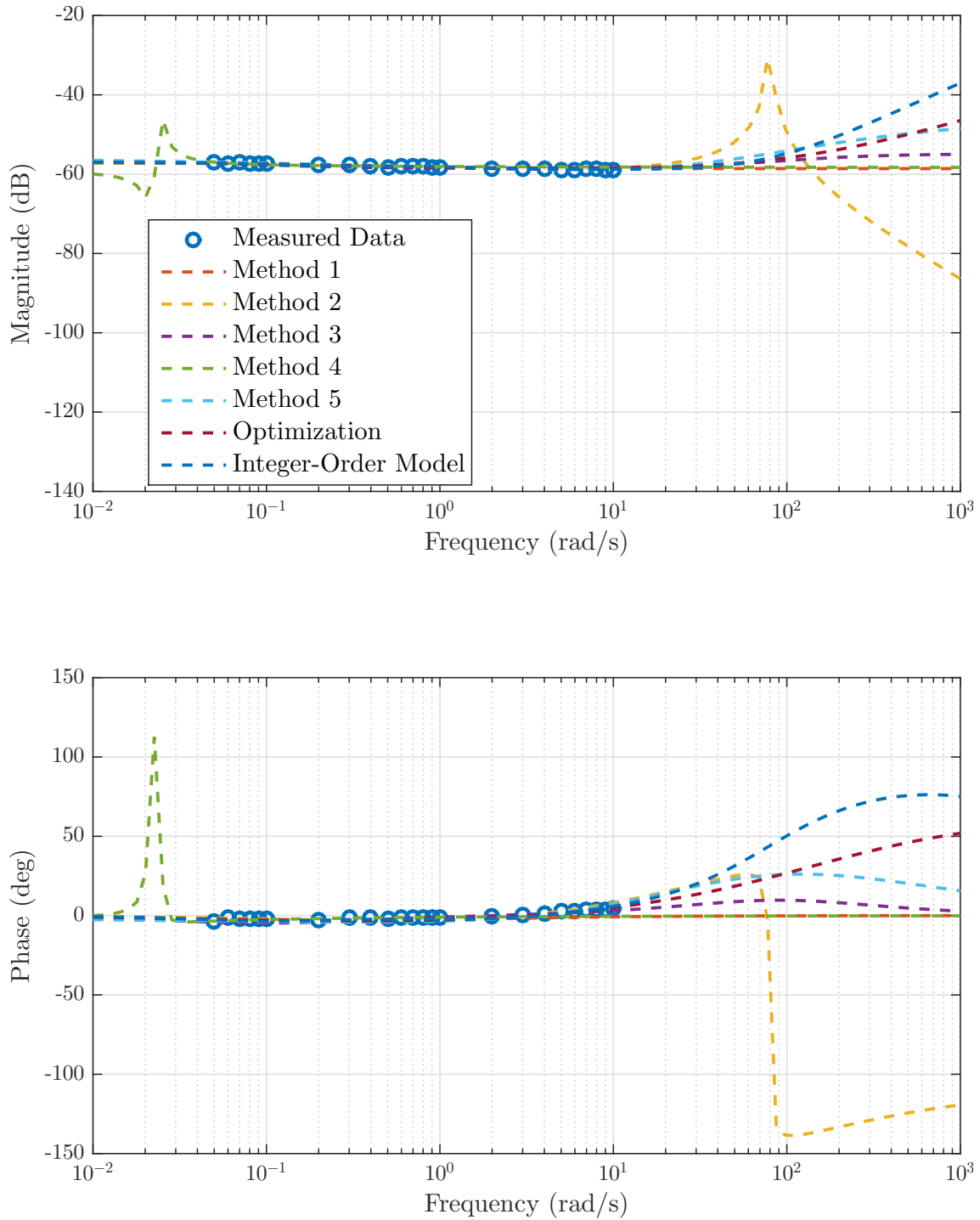
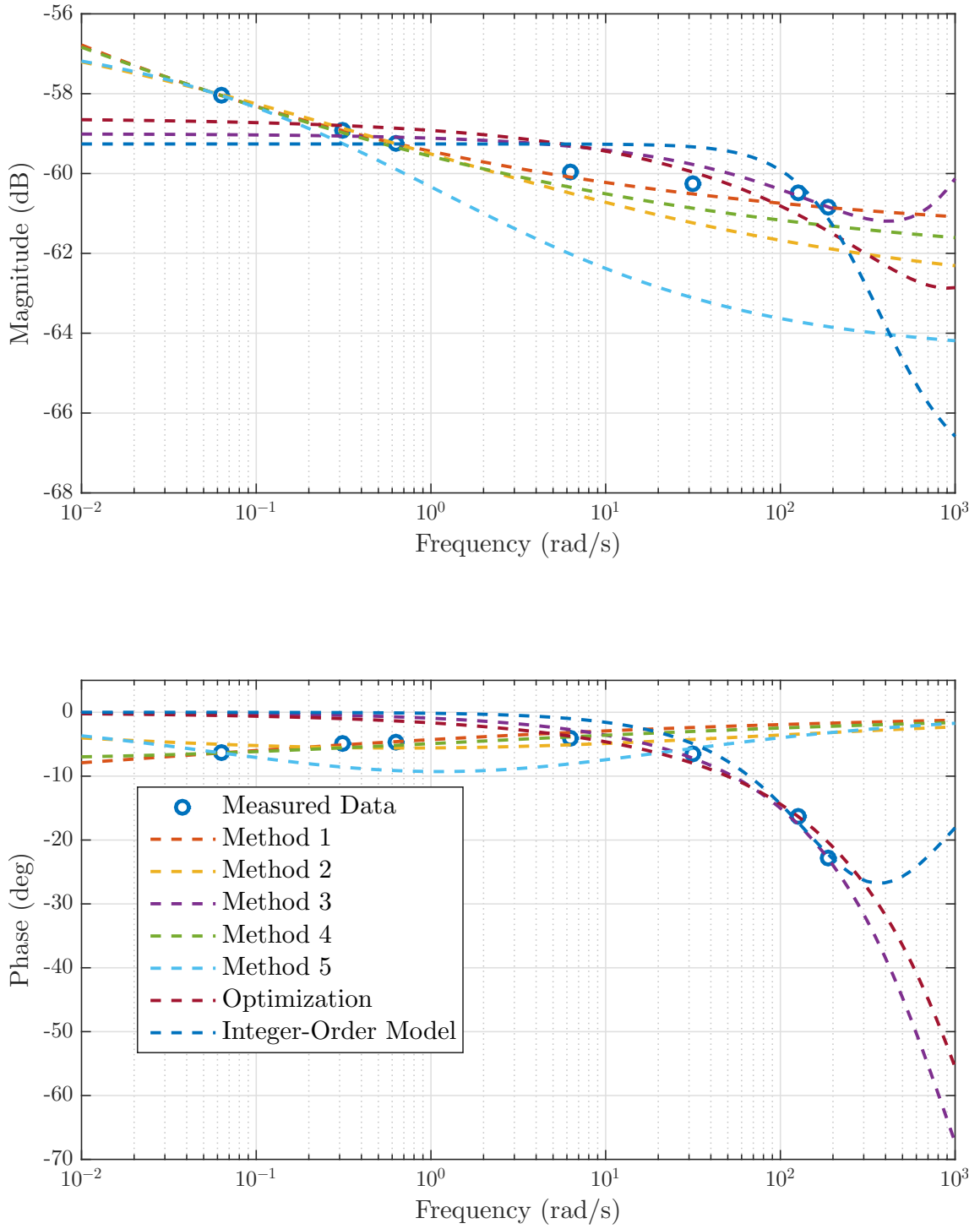Figure A.3: Best fit of the transfer behavior of PP for G_{max3} (orange sample, FC setup).

Figure A.4: Best fit of the transfer behavior of PP for G_{Zener} (orange sample, PC setup).
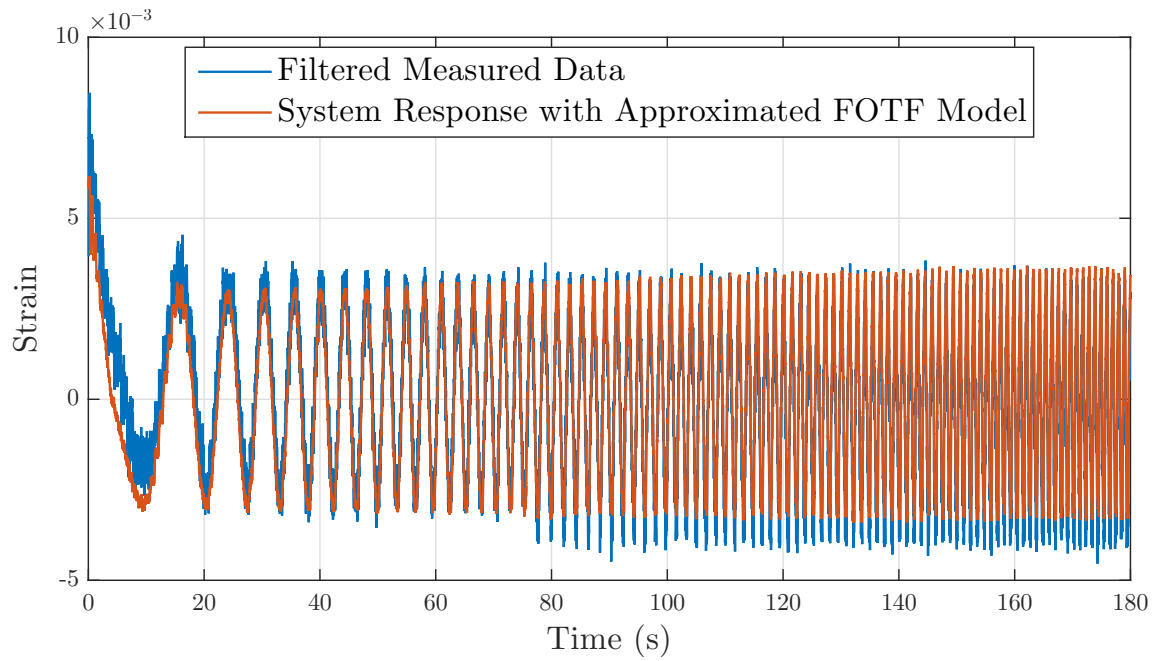
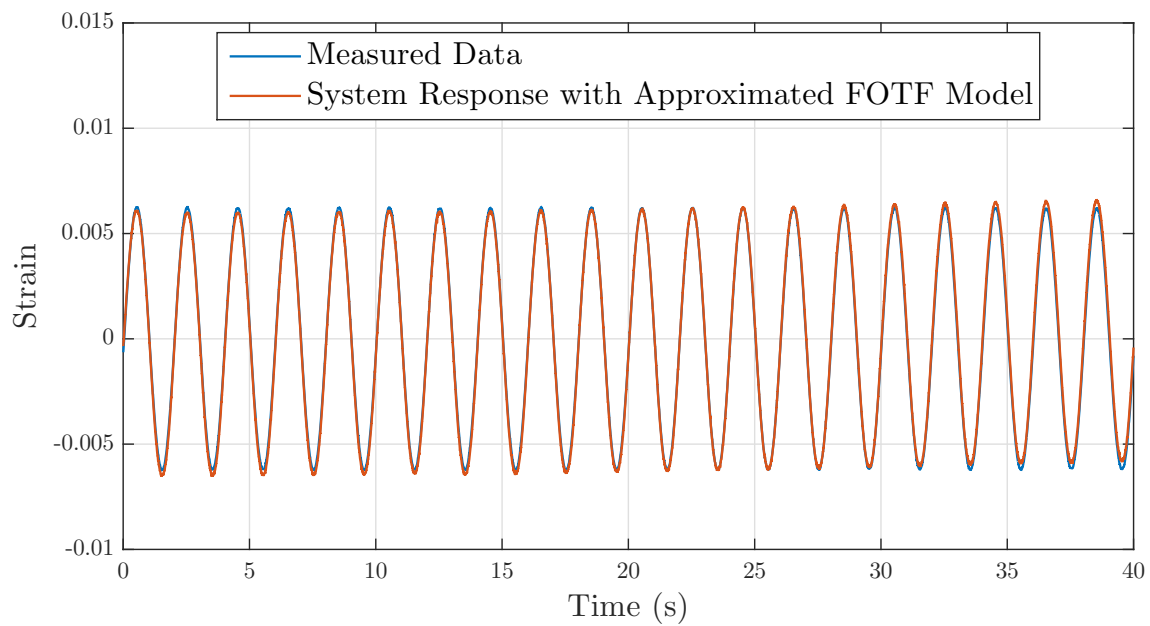Figure A.5: Validation in the time domain: measured and modeled chirp signals (FC setup).

Figure A.6: Validation in the time domain: measured and modeled sine signals with frequency of $0.5\,\text{Hz}$ (PC setup).
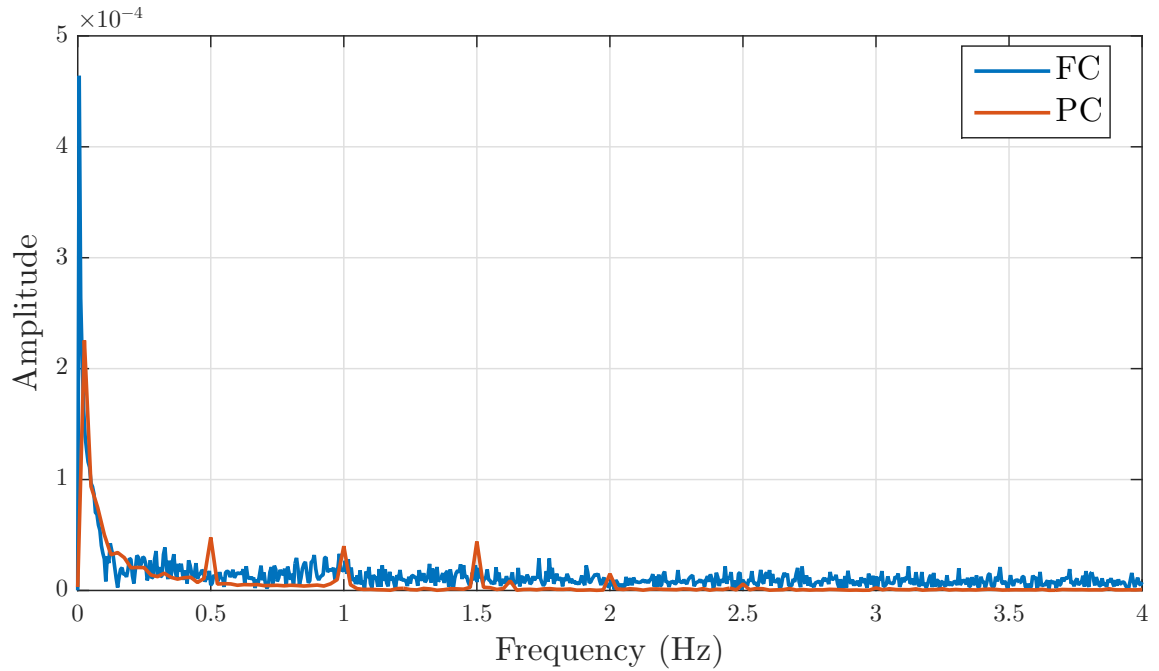
Figure A.7: Validation in the time domain: FFTs of the calculated absolute errors in Figures 4.13 and 4.14.

A.4 Experiments with Dashpot: Tables

Table A.11: Identification results dashpot open-loop measurements for G_{Voigt}: coefficients and commensurate order ($b = 1$).

Method	a		q
1	$\begin{bmatrix} -5.5552e5 & 5.7268e5 \end{bmatrix}$		0.01
4	$\begin{bmatrix} -5.1949e5 & 5.3664e5 \end{bmatrix}$		0.01
Opt	$\begin{bmatrix} -2.2173e5 & 5.6845e4 \end{bmatrix}$		1
Int	$\begin{bmatrix} -2.2173e5 & 5.6845e4 \end{bmatrix}$		1

Table A.12: Identification results dashpot open-loop measurements for G_{Zener} and G_{max3}: coefficients and commensurate order.

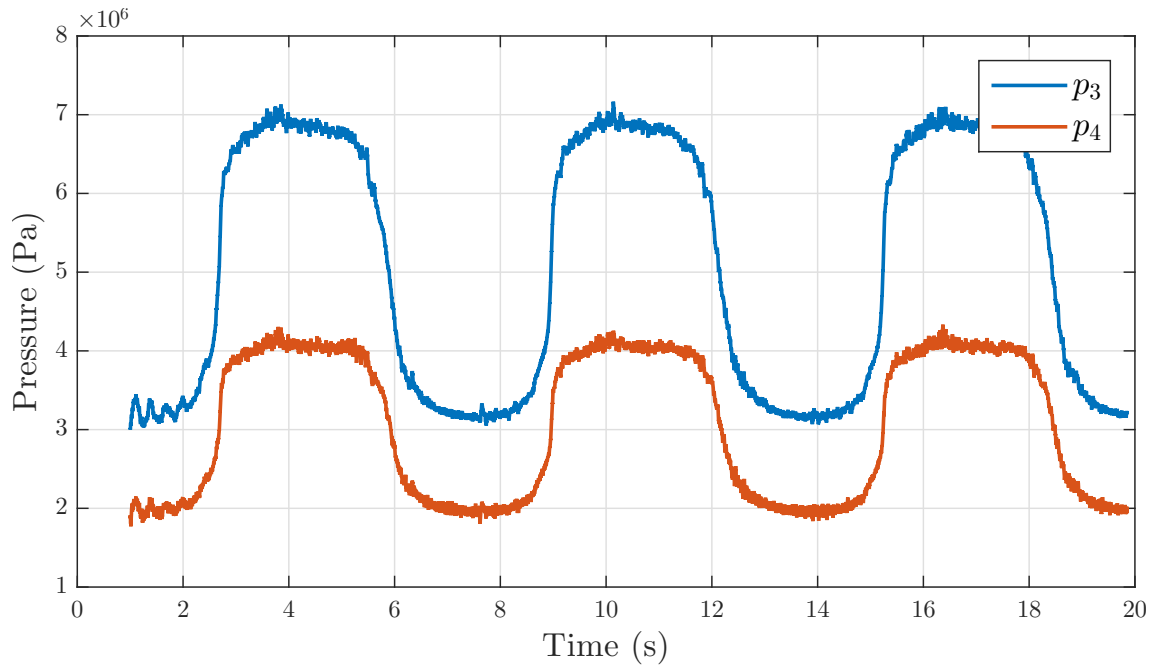| Met.		G_{Zener}	G_{max3}
	a	$\begin{bmatrix} -2.0027e3 & 1.7763e5 \end{bmatrix}$,	$\begin{bmatrix} -812.7716 & 1.5646e5 & -1.1731e6 & -3.9857e5 \end{bmatrix}$,
1	b	$\begin{bmatrix} 1 & -0.1883 \end{bmatrix}$,	$\begin{bmatrix} 1 & -15.1426 & 1.4236 \end{bmatrix}$,
	q	0.95	0.78
	a	$\begin{bmatrix} -1.5992e3 & 1.4449e5 \end{bmatrix}$,	$\begin{bmatrix} -7.6264e3 & 7.0315e4 & 1.2110e4 & -9.9384e3 \end{bmatrix}$,
2	b	$\begin{bmatrix} 1 & -0.1060 \end{bmatrix}$,	$\begin{bmatrix} 1 & -0.4398 & 0.0763 \end{bmatrix}$,
	q	1	0.64
	a	$\begin{bmatrix} 4.7973e4 & 1.9677e5 \end{bmatrix}$,	$\begin{bmatrix} -6.4736e3 & 3.5904e4 & 1.8754e4 & -1.6375e4 \end{bmatrix}$,
3	b	$\begin{bmatrix} 1 & -0.1500 \end{bmatrix}$,	$\begin{bmatrix} 1 & -0.5133 & 0.0975 \end{bmatrix}$,
	q	1	0.62
	a	$\begin{bmatrix} -2.1969e3 & 1.7343e5 \end{bmatrix}$,	$\begin{bmatrix} -2.1034e5 & -8.6551e5 & 2.0077e7 & 5.1246e5 \end{bmatrix}$,
4	b	$\begin{bmatrix} 1 & -0.1541 \end{bmatrix}$,	$\begin{bmatrix} 1 & 159.9927 & -29.2930 & 3.7717 \end{bmatrix}$,
	q	0.92	0.80
	a	$\begin{bmatrix} -1.3577e3 & 1.8174e5 \end{bmatrix}$,	$\begin{bmatrix} -1.1587e4 & 6.5977e4 & 8.0291e3 & -1.1230e4 \end{bmatrix}$,
5	b	$\begin{bmatrix} 1 & -0.1337 \end{bmatrix}$,	$\begin{bmatrix} 1 & -0.5068 & 0.0995 & -0.0023 \end{bmatrix}$,
	q	1	0.62
	a	$\begin{bmatrix} -2.0973e3 & 2.2762e5 \end{bmatrix}$,	$\begin{bmatrix} -1.5540e3 & 8.1747e4 & -6.5837e3 & -3.0135e3 \end{bmatrix}$,
Opt	b	$\begin{bmatrix} 1 & -0.1908 \end{bmatrix}$,	$\begin{bmatrix} 1 & -0.1613 & 0.0193 & 0.0013 \end{bmatrix}$,
	q	1	0.9178
	a	$\begin{bmatrix} -2.0973e3 & 2.2762e5 \end{bmatrix}$,	$\begin{bmatrix} 2.0116e3 & 7.8916e4 & -7.3047e3 & -1.9220e3 \end{bmatrix}$,
Int	b	$\begin{bmatrix} 1 & -0.1908 \end{bmatrix}$	$\begin{bmatrix} 1 & -0.1084 & 0.0136 & 0.0010 \end{bmatrix}$

A.5 Experiments with Dashpot: Figures

Figure A.8: Stationary behavior of the averaged measured pressures in the dashpot in closed-loop design for $\omega = 1\,\frac{\text{rad}}{\text{s}}$.
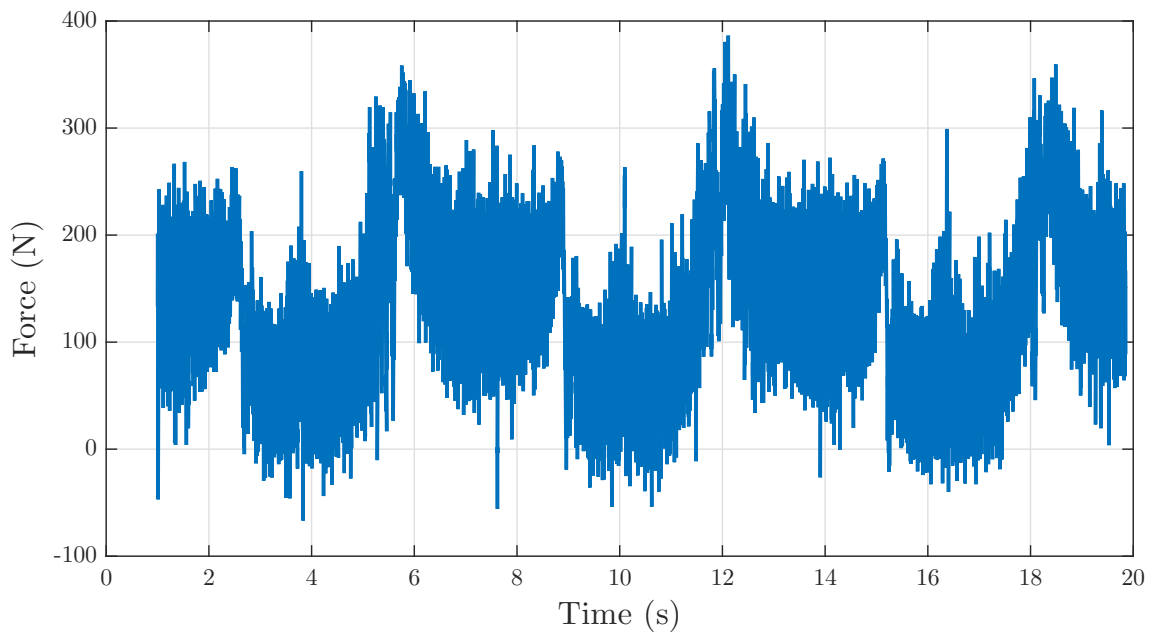

Figure A.9: Stationary behavior of the force calculated with the averaged measured pressures in the dashpot in closed-loop design for $\omega = 1\,\frac{\text{rad}}{\text{s}}$.
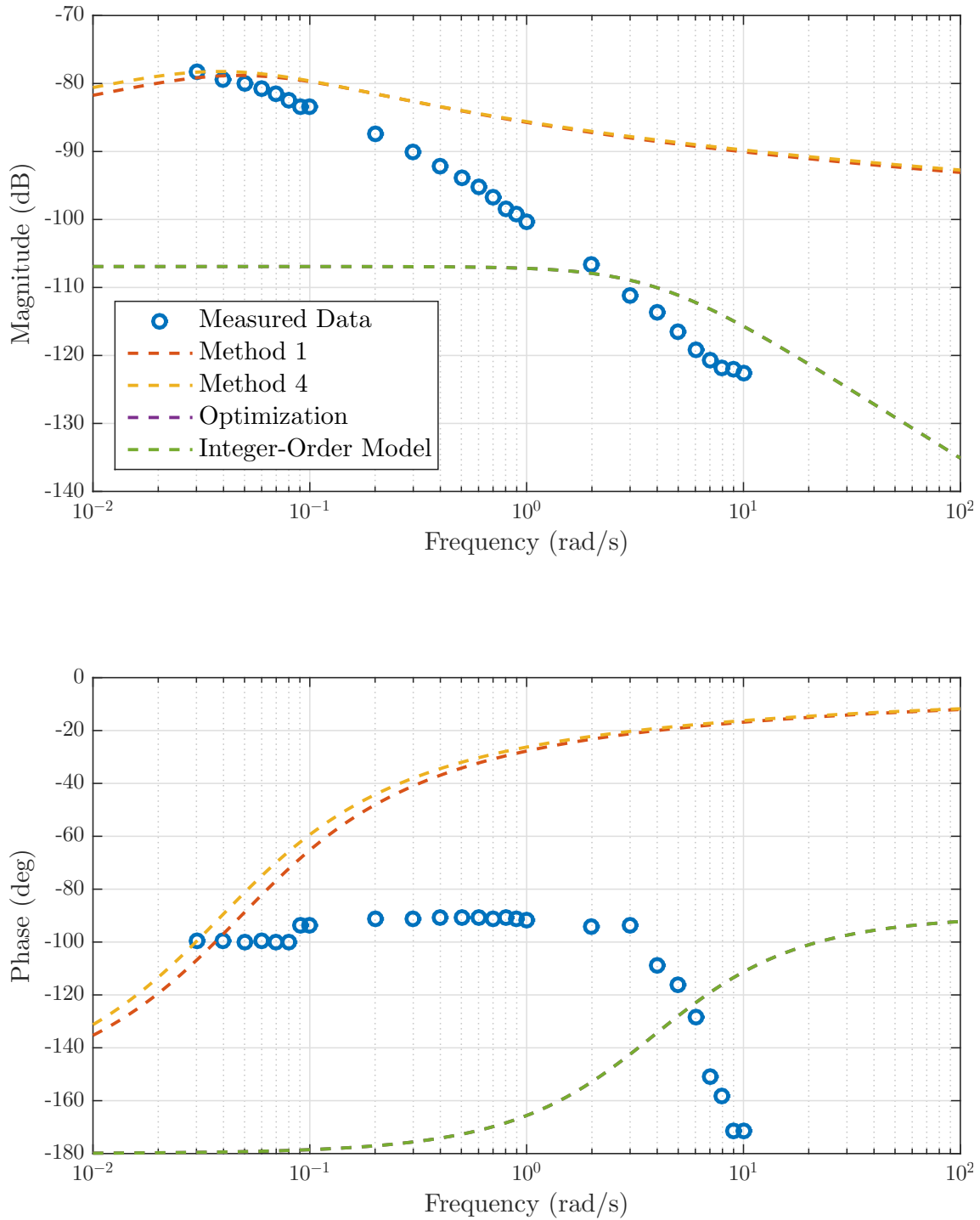
Figure A.10: Best fit of the transfer behavior of the dashpot with open-loop data for G_{Voigt}.

Bibliography

[1] Jay L. Adams, Tom T. Hartley, and Carl F. Lorenzo. "Fractional-order system identification using complex order-distributions". In: *2nd IFAC Workshop on Fractional Differentiation and its Applications, Porto, Portugal.* 2006, pp. 119–124.

[2] Klas Adolfsson, Mikael Enelund, and Peter Olsson. "On the fractional order model of viscoelasticity". In: *Mechanics of Time-Dependent Materials*, 9.1 (2005), pp. 15–34.

[3] Erwin Baur et al. *Saechtling-Kunststoff-Taschenbuch.* 30th edition. Hanser, 2007.

[4] Zehor Belkhatir and Taous Meriem Laleg-Kirati. "Parameters and fractional differentiation orders estimation for linear continuous-time non-commensurate fractional order systems". In: *Systems & Control Letters*, 115 (2018), pp. 26–33.

[5] Milan Cajić, Danilo Karličić, and Mihailo Lazarević. "Nonlocal vibration of a fractional order viscoelastic nanobeam with attached nanoparticle". In: *Theoretical and Applied Mechanics*, 42.3 (2015), pp. 167–190.

[6] Andrzej Dzieliński et al. "Identification of the fractional-order systems: a frequency domain approach". In: *Acta Montanistica Slovaca*, 16.1 (2011), pp. 26–33.

[7] Dietmar Findeisen and Siegfried Helduser. *Ölhydraulik: Handbuch der hydraulischen Antriebe und Steuerungen.* 6th edition. Springer Vieweg, 2015.

[8] Alan Freed, Kai Diethelm, and Yury Luchko. *Fractional-order viscoelasticity (FOV): constitutive development using the fractional calculus: first annual report.* NASA, 2002.

[9] Christian Friedrich. "Relaxation functions of rheological constitutive equations with fractional derivatives: thermodynamical constraints". In: *Rheological modelling: thermodynamical and statistical approaches.* Springer, 1991, pp. 321–330.

[10]   Eric W. Hansen. *Fourier transforms: principles and applications*. Wiley, 2014.

[11]   Per Christian Hansen. *Discrete inverse problems: insight and algorithms*. SIAM, 2010.

[12]   Tom T. Hartley and Carl F. Lorenzo. "Fractional-order system identification based on continuous order-distributions". In: *Signal Processing*, 83.11 (2003), pp. 2287–2300.

[13]   Nicole Heymans and J.-C. Bauwens. "Fractal rheological models and fractional differential equations for viscoelastic behavior". In: *Rheologica Acta*, 33.3 (1994), pp. 210–219.

[14]   Rolf Isermann and Marco Münchhof. *Identification of dynamic systems: an introduction with applications*. Springer, 2011.

[15]   József Karger-Kocsis, ed. *Polypropylene: an A-Z reference*. Kluwer, 1999.

[16]   Roderic S. Lakes. *Viscoelastic solids*. CRC Press, 1999.

[17]   P. J. Lawrence and G. J. Rogers. "Sequential transfer-function synthesis from measured data". In: *Proceedings of the Institution of Electrical Engineers*, 126.1 (1979), pp. 104–106.

[18]   E. C. Levy. "Complex-curve fitting". In: *IRE Transactions on Automatic Control*, AC-4.1 (1959), pp. 37–43.

[19]   Zeng Liao, Cheng Peng, and Yong Wang. "Subspace identification for commensurate fractional order systems using instrumental variables". In: *30th Chinese Control Conference, Yantai, China*. 2011, pp. 1636–1640.

[20]   Da-Yan Liu et al. "Identification of fractional order systems using modulating functions method". In: *American Control Conference, Washington, DC, USA*. 2013, pp. 1679–1684.

[21]   Lennart Ljung. *System identification: theory for the user*. 2nd edition. Prentice Hall, 1999.

[22]   Mohammad Amirian Matlob and Yousef Jamali. "The concepts and applications of fractional order differential calculus in modeling of viscoelastic systems: a primer". In: *Critical Reviews in Biomedical Engineering*, 47.4 (2019), pp. 249–276.

[23]   F. C. Meral, T. J. Royston, and R. Magin. "Fractional calculus in viscoelasticity: an experimental study". In: *Communications in Nonlinear Science and Numerical Simulation*, 15.4 (2010), pp. 939–945.

[24]   Concepción A. Monje et al. *Fractional-order systems and controls: fundamentals and applications.* Springer, 2010.

[25]   Philipp Pasolli and Michael Ruderman. "Hybrid state feedback position-force control of hydraulic cylinder". In: *IEEE International Conference on Mechatronics, Ilmenau, Germany.* 2019, pp. 54–59.

[26]   Philipp Pasolli and Michael Ruderman. "Linearized piecewise affine in control and states hydraulic system: modeling and identification". In: *IECON - 44th Annual Conference of the IEEE Industrial Electronics Society, Washington, DC, USA.* 2018, pp. 4537–4544.

[27]   Igor Podlubny. *Fractional differential equations: an introduction to fractional derivatives, fractional differential equations, to methods of their solution and some of their applications.* Academic Press, 1999.

[28]   Roell-Amsler-Prüfmaschinen GmbH & Co. KG. *Workshop 96 - Basisprogramm für quasistatische und dynamische Prüfungen zur Meß- und Regelelektronik: HydroWin 9600/9610/9640/9690.* 1999.

[29]   C. K. Sanathanan and J. Koerner. "Transfer function synthesis as a ratio of two complex polynomials". In: *IEEE Transactions on Automatic Control*, 8.1 (1963), pp. 56–58.

[30]   Alexandros Syrakos, Yannis Dimakopoulos, and John Tsamopoulos. "Theoretical study of the flow in a fluid damper containing high viscosity silicone oil: effects of shear-thinning and viscoelasticity". In: *Physics of Fluids*, 30.3 (2018). 030708.

[31]   Aleksei Tepljakov, Eduard Petlenkov, and Juri Belikov. "FOMCON: fractional-order modeling and control toolbox for MATLAB". In: *18th International Conference Mixed Design of Integrated Circuits and Systems, Gliwice, Poland.* 2011, pp. 684–689.

[32]   Nhan Phan Thien and Roger I. Tanner. "A new constitutive equation derived from network theory". In: *Journal of Non-Newtonian Fluid Mechanics*, 2.4 (1977), pp. 353–365.

[33]   Magalie Thomassin and Rachid Malti. "Subspace method for continuous-time fractional system identification". In: *IFAC Proceedings Volumes*, 42.10 (2009), pp. 880–885.

[34] Duarte Valério and José Sá da Costa. "Levy's identification method extended to commensurate fractional order transfer functions". In: *5th EUROMECH Nonlinear Dynamics Conference, Eindhoven.* 2005, pp. 1357–1366.

[35] Li Wang, Peng Cheng, and Yong Wang. "Frequency domain subspace identification of commensurate fractional order input time delay systems". In: *International Journal of Control, Automation and Systems*, 9.2 (2011), pp. 310–316.

[36] Wolfgang Weißbach, Michael Dahms, and Christoph Jaroschek. *Werkstoffkunde: Strukturen, Eigenschaften, Prüfung.* 19th edition. Springer Vieweg, 2015.

[37] K. Yasuda, R. C. Armstrong, and R. E. Cohen. "Shear flow properties of concentrated solutions of linear and star branched polystyrenes". In: *Rheologica Acta*, 20.2 (1981), pp. 163–178.

[38] Zwick-Roell GmbH & Co. KG. *Technische Angaben - Material-Prüfmaschine HB100.* 2004.

Declaration of Authorship

I hereby declare that I am the sole author of this thesis and that I have not used any sources other than those listed in the bibliography and identified as references. I further declare that I have not submitted this thesis at any other institution, in order to obtain a degree, and it has not been published yet.

Ilmenau, 20. 02. 2020